2023

ADVANCES AND APPLICATIONS IN ULTRASOUND-SWITCHABLE FLUORESCENCE IMAGING

Liqin Ren

ADVANCES AND APPLICATIONS IN ULTRASOUND-SWITCHABLE FLUORESCENCE IMAGING

by

LIQIN REN

Presented to the Faculty of the Graduate School of

The University of Texas at Arlington in Partial Fulfillment

of the Requirements

for the Degree of

DOCTOR OF PHILOSOPHY

THE UNIVERSITY OF TEXAS AT ARLINGTON

December 2023

Acknowledgments

I am profoundly grateful to all those who have supported me throughout my journey to attain this significant milestone in my academic career. The completion of this PhD thesis would not have been possible without the unwavering guidance, encouragement, and contributions from numerous individuals and institutions.

Foremost, I extend my deepest gratitude to my supervisor, Dr. Baohong Yuan, for his exceptional mentorship, unflagging support, and scholarly insights. Dr. Yuan's commitment to both my professional and personal growth has been a guiding light throughout this journey.

It is my privilege to have Dr. Hanli Liu, Dr. Kytai T. Nguyen, Dr. Yi Hong, and Dr. Juhyun Lee on my dissertation committee. I am sincerely grateful for all the insightful feedback, constructive criticism, and comprehensive evaluation of my research. Their expertise has immensely improved the quality of this thesis.

I am thankful to my colleagues and peers, Dr. Tingfeng Yao. Dr. Yang Liu, and Dr. Ruilin Liu and their camaraderie and intellectual exchange have fostered a stimulating academic environment. The vibrant discussions, collaborative efforts, and shared challenges have been instrumental in shaping my research perspective.

My family's enduring love, patience, and understanding have been my pillars of strength throughout this journey. Their belief in my abilities and unwavering encouragement has been a constant source of motivation.

This work was supported in part by funding from the Funding NIH/NIBIB 1R15EB030809-01, the REP 270089, and the CPRIT RP170564 (PI: Baohong Yuan).

Finally, I express my gratitude to the University of Texas at Arlington for providing me with the resources, facilities, and scholarly community that have been indispensable to my academic pursuits.

To every individual who has played a part, your presence has left an indelible mark, shaping the person I have become. Thank you, from the depths of my heart, for being an integral and cherished part of this remarkable life journey.

Dec 1st, 2023

Abstract

ADVANCES AND APPLICATIONS IN ULTRASOUND-SWITCHABLE FLUORESCENCE IMAGING

Liqin Ren, PhD

The University of Texas at Arlington, 2023

Supervising Professor: Baohong Yuan

Cancer diagnosis is a prerequisite for further medical therapy and treatment. Near-infrared (NIR) fluorescence imaging is a desirable modality without invasiveness and nonionizing radiation. However, fluorescence suffers from a strong light scattering in tissues, leading to a low spatial resolution and low sensitivity in centimeter-deep tissue (limited to several millimeters).

To enhance spatial resolution and avoid the high scattering of conventional fluorescence imaging in deep tissue, ultrasound-switchable fluorescence (USF) imaging has emerged as a highly promising technique for biomedical imaging and research. The principle of improving spatial resolution in USF imaging is to confine the fluorescence emission from thermosensitive fluorophores to a small focal volume via focused ultrasound (FU) stimulations. As a result, the ambient background fluorescent signals can be effectively suppressed.

The study achieved the size control of polymer-based and indocyanine green (ICG) encapsulated USF contrast agents, capable of accumulating in the tumor after intravenous injections. These nanoprobes varied in size from 58 nm to 321 nm. The bioimaging profiles demonstrated that the proposed nanoparticles can efficiently eliminate the background light from normal tissue and show a tumor-specific fluorescence enhancement in the BxPC-3 tumor-bearing mice models possibly via the enhanced permeability and retention effect. *In vivo* tumor USF imaging further demonstrated that these nanoprobes can effectively be switched 'ON' with enhanced fluorescence in response to a FU stimulation in the tumor microenvironment, contributing to the high-resolution USF images. Furthermore, USF technique was utilized to estimate the local background temperature for the first time by

analyzing the temperature dependence of fluorescence emission from USF contrast agents induced by a FU beam. The USF contrast agent suspension was injected into a microtube that was embedded into a phantom and the dynamic USF signal was acquired using a camera-based USF system. The results showed that the difference between the temperatures acquired from the USF thermometry and the infrared thermography was 0.64 ± 0.43 °C when operating at the physiological temperature range from 35.27 to 39.31 °C. Lastly, an experimental investigation into the dynamics of interstitial fluid streaming and tissue recovery in animal tissue induced by the mechanical effects of acoustic waves was performed. Temperature-insensitive sulforhodamine-101 encapsulated poly(lactic-co-glycolic acid) nanoparticles with a size of 175 nm were locally injected into animal tissues. The changes of fluorescence over time caused by the streaming and backflow of interstitial fluid were studied with two *ex vivo* animal tissue models, and a faster recovery was observed in porcine tissue compared with the results in chicken tissue.

In summary, *in vivo* USF imaging in tumor-bearing mouse models via intravenous (i.v.) injections of ICG-encapsulated poly (N-isopropylacrylamide) (PNIPAM) nanoparticles was achieved for the first time. Our findings suggest that ICG-PNIPAM agents are good candidates for USF imaging of tumors in live animals, indicating their great potential in optical tumor imaging in deep tissue. Except for imaging, the potential application of USF techniques in temperature measurements was also explored. The designed USF-based thermometry showed a broad application prospect in high spatial resolution temperature imaging with a tunable measurement range in deep tissue Finally, USF was employed to experimentally investigate the ultrasound-induced transport of nanoparticles in *ex vivo* tissues.

This work has paved the way for the prospective integration of the USF imaging technique into various biomedical applications.

Table of Contents

List of Illustrations

List of Tables

Chapter 1 INTRODUCTION

1.1 Fluorescence imaging

Fluorescence imaging plays a pivotal role in the early diagnosis and evaluation of therapeutic responses to diseases in clinical settings [1]–[3]. It has several advantages including cost-effectiveness, non-invasiveness, high sensitivity, and the absence of ionizing radiation and provides comparative benefits over other diagnostic techniques including computed tomography (CT), positron emission tomography (PET), and magnetic resonance imaging (MRI) [4].

However, the interactions between photons and biological tissues, including reflection, absorption, scattering, and autofluorescence largely determine the acquired fluorescence intensity as illustrated in Fig. 1. In traditional fluorescence imaging within the visible spectrum band from 400 to 700 nm, biological tissues exhibit substantial absorption, scattering, and background autofluorescence from biomolecules, especially as the penetration path increases [5]. Therefore, fluorescence imaging has a main barrier of limited tissue penetration (<3 mm), resulting in a loss of physiological and pathological information of microstructures at the centimeter level [6].

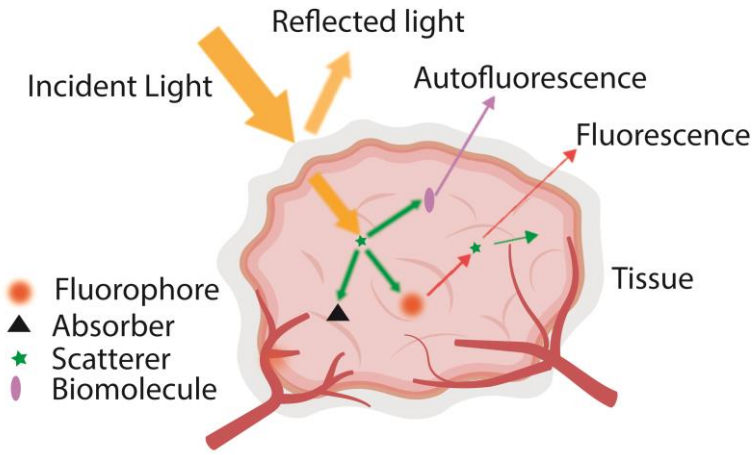

Figure 1 The light and tissue interactions

In order to overcome the main challenges mentioned above, fluorescence imaging in biological transparency near-infrared (NIR) window (700-900 nm) has been explored in the last few decades for the fact the tissue is relatively transparent in this light band due to less scattering in tissue and less absorption by blood [4], [7].

1.2 Principle of ultrasound-switchable fluorescence imaging

Nevertheless, NIR fluorescence imaging has a poor spatial resolution (~5 mm) in tissues at a depth of centimeters, which hinders the clinical applications of ICG-based fluorescence imaging. Ultrasound-switchable fluorescence (USF) imaging, which combines a fluorescence imaging system with a FU system, has overcome this issue. Figure 2 shows a simplified schematic diagram of USF imaging system with electron-multiplying charge-coupled device (EMCCD). During USF imaging, FU locally heats the tissue up in its focal zone, leading to an increased fluorescence intensity from the temperature-sensitive imaging probes in the confined zone. In this way, the background fluorescent signals from the surroundings can be suppressed. The fluorescence increase is referred to as the USF signal, which can be further captured using an EMCCD or Photomultiplier tube [8], [9]. The spatial resolution in USF imaging depends on the thermal focal size induced by ultrasound, given that the enhanced fluorescence is emitted from the fluorescent agents with higher temperatures. To improve this resolution, options include using shorter, more intense FU exposures, higher-frequency FU transducers (with reduced penetration), or dual perpendicular FU transducers for better axial resolution [10]. However, enhanced resolution often comes at the cost of reduced signal-to-noise ratio (SNR) due to fewer fluorophores in the smaller thermal focal zone.

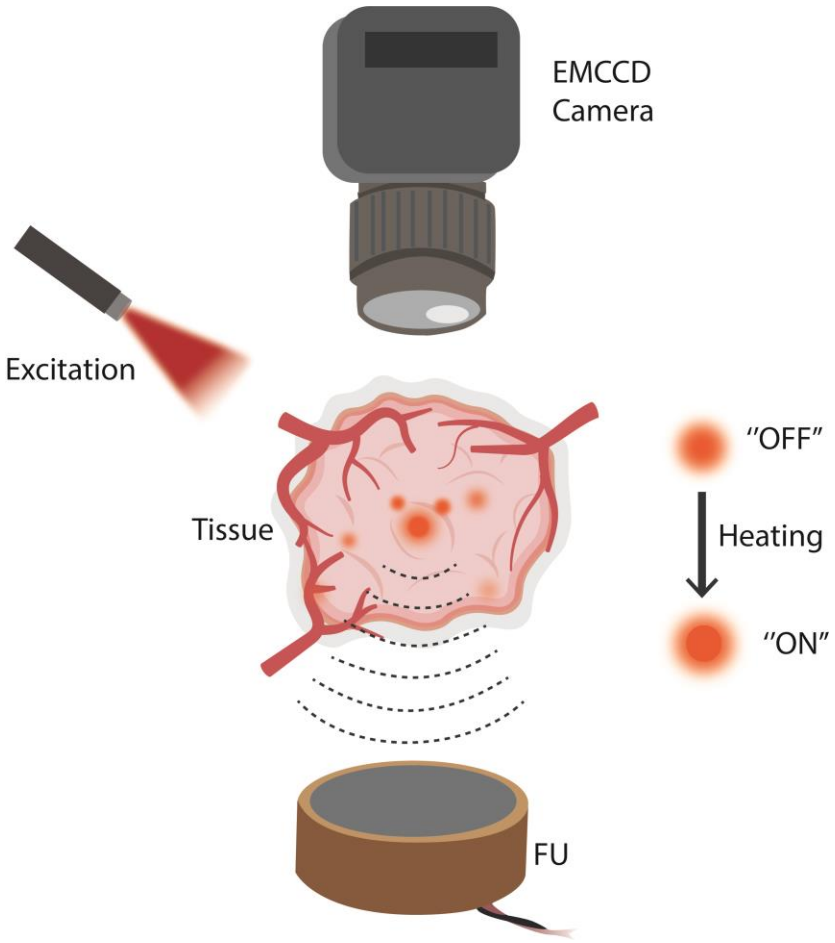

Figure 2 The schematic diagram of USF imaging.

1.3 Thermosensitive USF contrast agents

Indocyanine green (ICG) is a near-infrared fluorescence dye with an emission peak at 830 nm approved for clinical applications in the United States by the Food and Drug Administration [11]. ICG is often used for sentinel lymph node mapping due to the increased quantum yield (>3 folds) and reduced aggregation from the ICG-protein binding [12]. In addition, ICG molecules can be exploited to image cancerous tissue and solid tumors (such as hepatocellular carcinoma, liver metastases, and breast tumors) because these agents can passively accumulate into tumor sites via newly formed, porous, and permeable blood vessels [13].

There are two types of USF contrast agents currently extensively used in *in vivo* USF imaging studies: (1) ICG-encapsulated poly(N-isopropylacrylamide) (PNIPAM) nanoparticle (ICG-PNIPAM NP); and (2) ICG-encapsulated liposome.

PNIPAM is a thermo-sensitive polymer. Below its lower critical solution temperature (LCST), PNIAPM is a swollen hydrogel with a larger volume in aqueous solutions and the hydrogen bonding between the polymer and water molecules is formed. When the temperature rises above the LCST, these hydrogen bonds break, and new bonds will form among the amide groups. This increases the hydrophobicity of PNIPAM and NIPAM chain will collapse into a spherical conformation, leading to the release of trapped water molecules and causing a sol–gel transition [14]. Reduced solvent polarity leads to increased fluorescence intensity in ICG molecules [15]. When the temperature exceeds the LCST, the fluorescence emission of the ICG dyes inside the PNIPAM nanoparticles can increase in a less polarized microenvironment.

Liposomes have been widely used for different biomedical applications, such as drug carriers and imaging agents [16]. They are spherical vesicles consisting of one or more phospholipid bilayers and an aqueous core. When the temperature exceeds the transition temperature, phospholipids are in a liquid crystalline phase with high fluidity and generally low permeability, allowing rapid movement of individual lipid molecules [17]. This temperature-dependent gel-to-liquid crystalline phase transition of the liposomes contrast agents enables an ‘OFF–ON’ switch in fluorescence from the loaded dyes [18], [19].

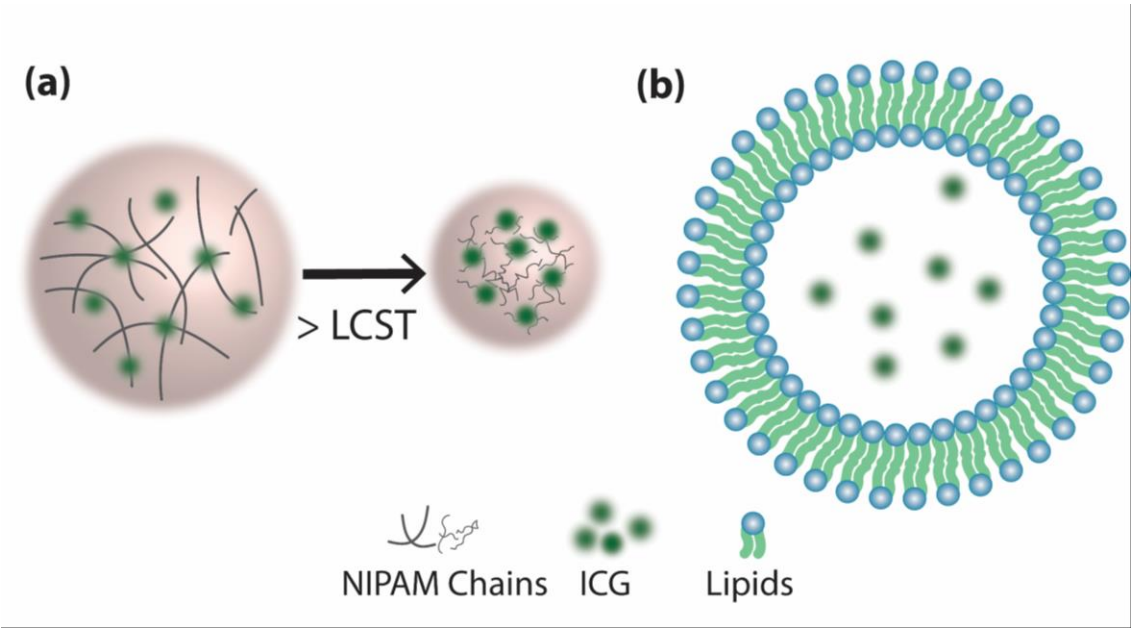

Figure 3 Representation of the general structure of (a) ICG-PNIPAM; (b) ICG-loaded liposomes.

1.4 The application of USF in thermometry

Precise tissue temperature measurement is vital for understanding thermal dynamics in biological systems, facilitating research in thermoregulation, metabolism, neuronal and cancer cell activities [20]–[22]. It can have diverse applications across various fields, including drug development, biotechnology, life sciences, healthcare, and molecular biology [23]–[25]. However, traditional methods face several limitations. They can be invasive to biological systems (e.g., thermocouples or optical fibers) or exhibit inaccuracies, insensitivity, and interferences (e.g. conventional fluorescent thermometry) [26], [27]. Additionally, infrared (IR)-based thermometry can only gauge surface temperature [28], [29]. To overcome these constraints and enable accurate, noninvasive, sensitive, and specific temperature imaging in biological samples, USF thermometry based on fluorescent liposomes was explored in this study. In contrast to micro-sized liposomes, which display two lower critical solution temperatures (LCSTs) at 32 and 42 °C, nano-sized liposomes exhibit a considerably narrower transition bandwidth [30], [31]. This increased sensitivity to elevated temperatures enables the feasible estimation of tissue temperature through the analysis of temperature-dependent fluorescence emissions induced by FU.

1.5 Ultrasound-induced nanoparticles transport

Nanotechnology has been employed for enhanced drug and fluorophore accumulations in the targeted sites (e.g., tumor and inflammable tissues) with less toxicity and side effects to healthy cells over the last decades. However, there are still challenges such as protein-nanoparticle binds in the circulation system, renal clearance, and extraction by the reticuloendothelial systems, which hinder a site-specific drug delivery with a controlled release in the preclinical/ clinical research [32]. Therefore, ultrasound-responsive drug delivery has been recognized for site-selectively enhanced drug release and activation in nanomaterials [33].

The motivation for this study arises from an intriguing observation into USF imaging of tumors via i.v. injection of PNIPAM/β-CD/ICG nanoparticles. Detailed *in vivo* results can be found in Appendix A of this dissertation. Intramuscular USF imaging of a mouse tumor via local injections has previously confirmed the continued thermosensitivity and ultrasound-switchability of PNIPAM/β-CD/ICG in the tumor microenvironment [34]. Although fluorescent agents successfully accumulated in the tumor after i.v. injection via the tail vein, a fluorescence reduction, instead of an enhancement, was found in the ultrasound focal zone during a typical USF imaging experiment. To elucidate this phenomenon, squeezing interstitial fluid via transfer of ultrasound momentum (SIF-TUM) theory was introduced [35]. Briefly, FU exerts pressure on the tissue within a confined ultrasound focal volume from all directions, and interstitial fluid with fluorophores can be squeezed out from the focal zone, leading to a fluorescence reduction. When the ultrasound is deactivated, the elastic properties of the tissue's solid matrix prompt a backflow, leading to a recovery of fluorescence. In this work, comprehensive experimental studies were conducted to offer a practical understanding of SIF-TUM.

1.6 Dissertation outline

The first motivation of the thesis is to demonstrate the feasibility of *in vivo* tumor USF imaging in mice via i.v. injection of polymer-based USF contrast agents. While *in vivo* USF imaging of mouse organs (e.g., spleen and liver) via i.v. injections, as well as tumors via local injections, has been successfully conducted in the past, achieving *in vivo* tumor USF imaging via i.v. injections remains a challenge [36], [37]. By appropriately controlling the size and concentration of ICG-PNIPAM, passive tumor targeting can be observed in BxPC-3 xenograft tumor models with a reasonable tumor/normal tissue ratio. Thus, the feasibility of performing three-dimensional *in vivo* USF imaging in mouse tumors should be studied. In Chapter 2, the USF imaging performances of size-varying ICG-PNIPAM nanoparticles were compared in the blood-vessel mimicking phantom model. Their biodistribution results in BxPC-3

tumor xenograft mice were also investigated. Three-dimensional *in vivo* USF imaging of the BxPC-3 tumor via intravenous injections was also successfully achieved.

In addition to obtaining structural information about tissues, there is a growing demand for USF imaging to provide functional insights into the physiological conditions of tissues. Monitoring the local temperature within deep tissues is crucial, as it is closely linked to cellular activity and can serve as an indicator for diseases such as cancer and inflammation. Unfortunately, only a limited number of technologies are available for this purpose. Thermometry based on the USF technique offers a promising solution, characterized by its high sensitivity, cost-effectiveness, and the potential for two-dimensional temperature mapping in deep tissue through scanning. In Chapter 3, therefore, a pilot study on the silicone tube embed phantom model was tested for USF-based temperature measurements. A USF thermometry was developed, and the results were validated by a commercial IR camera.

The transport of therapeutic or diagnostic agents throughout the tissues to the target cells or diseased areas is a prerequisite for effective drug delivery or target-enhanced imaging contrast [35], [38]. The FU-based modulation of the interstitial fluid is an attractive alternative to accelerate drug and agent transport in deep tissue within a short time frame. However, there is not much work reported on the dynamics of motion of nanoparticles and tissue recovery after ultrasound exposure, and it is therefore important to fill this gap by studying the effects of experimental factors on the movements of nanoparticles induced by FU exposures in *ex vivo* tissues. In Chapter 4, FU-induced displacements of fluorescent nanoparticles in the *ex vivo* tissues were investigated. The tissue property-dependent fluorescence recovery within the focal area was also compared in centimeter-thick porcine muscle and chicken breast tissues.

Chapter 5 provides a summary of all the findings and gives a discussion about limitations and future work.

Chapter 2 IN VIVO TUMOR USF IMAGING VIA INTRAVENOUS INJECTIONS OF ICG-PNIPAM

2.1 Introduction

Cancer is one of the most common causes of premature death worldwide [39]. In the United States, there are roughly 1,958,310 new cancer cases and 609,820 cancer deaths in 2023 [40]. Biomedical imaging plays an essential role in the early detection and characterization of cancers while they are growing.

Previous studies demonstrated successful USF imaging of sub-millimeter silicone tubes in 3.5 cm and 5.5 cm-thick chicken breast tissues. These promising results demonstrated the feasibility of USF imaging in centimeter-deep tissues with a high imaging resolution [34], [41].

ICG-based PNIPAM nanoparticle as one of the USF contrast agents exhibited adjustable LCST, high stability in biological environments, and long shelf-life (>6 months) [42]. *In vivo* USF imaging of mouse organs, such as the spleen and liver, via intravenous (i.v.) injections of PNIPAM nanoparticles was successfully achieved [37]. However, *in vivo* tumor USF imaging via i.v. injections is much more challenging because a sufficient number of nanoparticles must be accumulated in the tumor to achieve an acceptable USF SNR. Therefore, local intratumoral injections were usually adopted in our previous studies to bypass this challenge and allow us to focus on addressing other fundamental and technical challenges [30], [34], [36], [37]. With success in the development of various sensitive USF imaging systems and stable contrast agents, *in vivo* tumor USF imaging via i.v. injections has become increasingly more desirable and achievable. In this study, this goal was achieved by appropriately controlling the size and concentration of ICG-encapsulated PNIPAM (ICG-PNIPAM) nanoparticles. The size effect of ICG-PNIPAM on USF imaging and tumor accumulation was investigated by changing the quantity of surfactants added during the synthesis. Passive tumor targeting of ICG-PNIPAM was demonstrated in BxPC-3 xenograft tumor models with a tumor/normal tissue (T/N) ratio of ~2.3 ± 0.6 at 24 h post-injection. These results indicate that the ICG-PNIPAM nanoparticles are feasible for *in vivo* USF imaging in BxPC-3 tumor, possibly via the enhanced permeability and retention (EPR) effect.

2.2 Materials and methods

2.2.1 Fluorescence intensity study

An in-house built cuvette system was used to examine the fluorescence intensity profile over temperature [41]. A 3 mL sample was loaded into a 3.5 mL quartz cuvette and placed in a temperature-controlled holder (Quantum

Northwest, Inc., USA) with a stir at 1000 rpm. An 808 nm excitation laser (MGL-II-808-2W, Dragon Lasers, China) was used to excite the sample. The emitted light from the sample passed through an 830 long-pass filter (Semrock, USA) before being collected by a modular USB spectrometer (USB2000+, Ocean Inlight, USA). The temperature measurement ranged from 30 ˚C to 55 ˚C with an increment of 0.1 ˚C. A temperature probe was inserted into the cuvette to monitor the sample temperature and the fluorescence intensity was recorded.

2.2.2 USF imaging systems

Phantom experiments and USF imaging via local injections were performed in a previously reported fiber bundle-based USF system [36]. The excitation path consisted of a 785 nm laser (MDL-III-785-2W, Dragon Lasers, China) modulated at 1 kHz by a function generator (FG, 33220A, Agilent, USA) and a bandpass excitation filter (FF01-785/62-25, Semrock Inc., USA). Emitted fluorescence signals were collected by a fiber bundle and transmitted through two 830 nm long-pass filters (BLP01-830R, Semrock Inc., USA), a photomultiplier tube (PMT, H7422-20, Hamamatsu Photonics, Japan) driven by a high-voltage source (C8137-02, Hamamatsu, Japan) and a low-noise current preamplifier (SR570, Stanford Research Systems, USA). Finally, the emission signal was extracted by a lock-in amplifier (SR830, Stanford Research Systems, USA) with a time constant of 300 ms. A FU transducer (2.5 MHz, H-108, Sonic Concepts Inc., USA) raster scanned the sample in the XY plane, and thermally enhanced fluorescence signals were recorded at each location to obtain the two-dimensional USF profile of the tube.

The USF studies via i.v. injections were conducted in a camera-based USF system that offered a high imaging sensitivity, especially in the electron-multiplying gain mode [41]. Briefly, an excitation beam from an 808 nm laser (MGL-II-808-2W, Dragon Lasers, China) passed through a bandpass filter (LL01-808-25, Semrock Inc., USA) and was split by a dual branch light guide (1/4 × 72", Edmund Optics Inc., USA) fiber into two paths to provide uniform illumination on the sample from two opposite directions. The emission light passed through three long-pass filters (BLP01-830R-50/25, Semrock Inc., USA), a camera lens (AF NIKKOR 50 mm f/1.8D Lens, Nikon, Japan), and finally was collected by an EMCCD camera (ProEM®-HS: 1024BX3, Princeton Instruments, USA). A 2.5 MHz FU transducer (H-108, Sonic Concepts Inc., USA) powered by an amplified electrical signal from a 50 dB-gain radio frequency power amplifier (RF-AMP, A075, E&I, USA) was used to create a heated focal volume in the tissue. A three-axis motorized translation stage (XSlide™ and VXM™, Velmex Inc., USA) was used for raster scanning of the subject. During the USF experiments, the exposure time of camera was kept at 1500 ms.

The first fluorescence image was obtained before the FU exposure (exposure time=400 ms); the second was captured immediately after this exposure. The USF image was calculated by subtracting the corresponding pixel values of the first image from the second image, and then further filtered based on the correlation between a normalized averaging filter (typically 15 x 15 pixels) and the image (1024 x 1024 pixels).

2.2.3 USF imaging of a silicone tube embedded in a tissue mimicking phantom

To simulate the blood vessel, a silicone tube (ST 60-011-02, Helix Medical, USA) with an inner diameter of 0.51 mm and an outer diameter of 0.94 mm was embedded in the silicone phantom (along the y-axis) at a depth of ~3 mm. The thickness of the phantom was 7 mm, and the method of fabricating the silicone phantom was based on a published study [42]. The absorption coefficient was estimated at 0.03 cm^{-1}, and the reduced scattering coefficient was 3.5 cm^{-1} [8]. Figure 4(a) illustrates the schematic diagram of imaging a blood vessel-mimicking phantom sample in the fiber bundle-based USF system. The silicone tube was filled with ICG-PNIPAM and illuminated with an excitation laser beam (1.05 mW/cm^2). The mechanical index (MI) of FU was 1.72, and the exposure time was 400 ms.

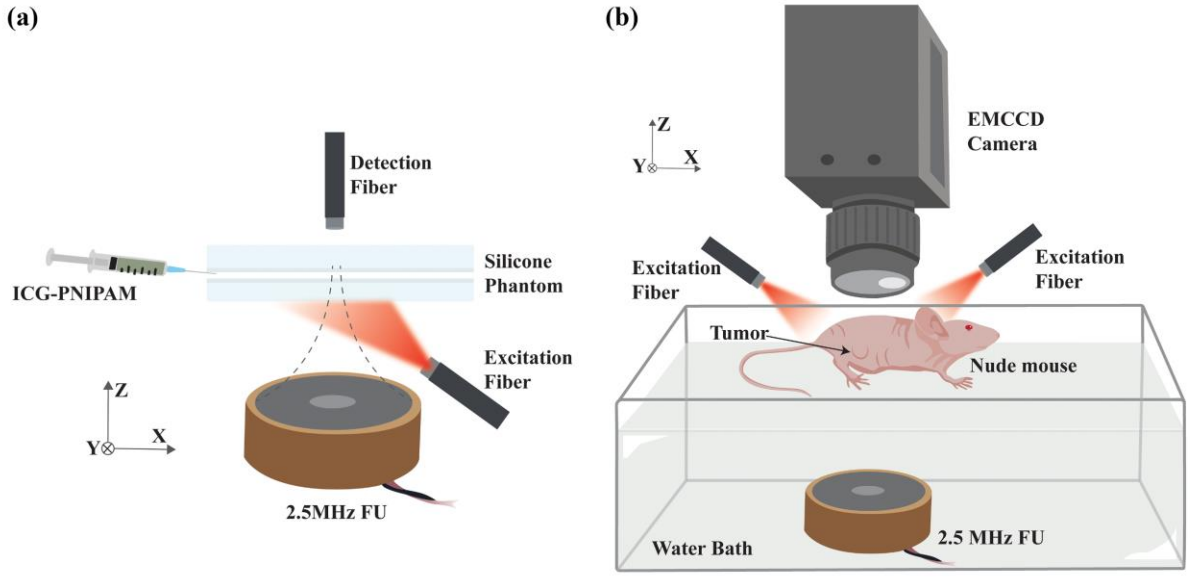

Figure 4 The experimental set-up of USF imaging system. (a) Fiber bundle-based system for tissue-mimicking phantom tests and (b) Camera-based system for *in vivo* USF imaging.

2.2.4 USF imaging at mouse leg after a local injection

This USF study was performed in the fiber bundle-based system. About 10-15 µL contrast agent was locally injected into the hind thigh muscle of BALB/cJ mice (female, Jackson Laboratory, USA) to test the thermal responses of samples. The hair on the mice legs was shaved to avoid light scattering and provide better image contrasts. The temperature of the water bath was maintained at 37.5 °C to keep the mouse body warm. The FU transducer raster scanned a volume of 8.89 (X) * 8.89 (Y) * 3.81 (Z) mm^3 (step size in X&Y direction: 0.889 mm; step size in Z direction: 1.27 mm) with a MI value of 2.81 and exposure time of 400 ms. The excitation laser intensity was adjusted based on the fluorescence strength of each sample and had a range from 0.62 to 0.67 mW/cm^2.

2.2.5 In vivo biodistribution analysis on BxPC-3 tumor-bearing nude mice

NIR fluorescence images (λex = 808 nm, λem = 830 nm) of mice were captured at selected time points before and after an i.v. injection of 200 µL ICG-PNIPAM (n=3 for each group). For each BxPC-3 tumor-bearing mouse, it was observed for the biodistribution study first for about 24 h, and USF imaging was performed afterwards. Finally, mice were euthanized at around 30 h post-administration, and their excised organs/tissues were imaged and semi-quantitatively analyzed by calculating the ratio between the average fluorescence intensity of organ and muscle.

2.2.6 In vivo NIR-USF imaging of BxPC-3 tumor via a tail vein injection

In vivo NIR-USF imaging was conducted in the camera-based USF system. Nude mice bearing BxPC-3 tumors were injected with 200 µL ICG-PNIPAM nanoparticles, and NIR fluorescence images at selected time points were captured. After acquiring the fluorescence images at 24 h post i.v. injection and a high tumor-to-background contrast was observed, the tumor-bearing mice were ready for USF imaging. The water bath temperature was kept at 37.5 °C to avoid massive heat dissipation of the mouse while it was anesthetized with 1.8 % isoflurane with a flow rate at 0.8 L/min. The scan volume was 7.62 (X) * 7.62 (Y) * 5.08 mm^3 (Z) (step size in X&Y direction: 0.762 mm; step size in Z direction: 1.27 mm). The laser intensity (λex = 808 nm) was 7.56 mW/cm^2. The acoustic pressure amplitudes of FU were adjusted based on the size and location of tumors in the mice in each USF experiment. Usually, the acoustic energy was more attenuated in the denser tissue and longer transmission path. For example, when a tumor was directly accessible by the ultrasound beam, the MI value was 3.63. It was adjusted up to 8.19 for one tumor when the ultrasound beam had to pass through the mouse body before reaching the tumor. In addition, these MIs were calculated based on the pressure amplitudes of FU measured via a fiber-optic hydrophone (FOHS, precision acoustic, UK) in the degassed water instead of real tissues or tissue-mimicking materials. The real MI in tumors might be much lower than these numbers because of ultrasound attenuation caused by the reflection from the interface between tissue and water, and the absorption and scattering from the tissue were ignored in the calculation. Figure 4(b) shows the experimental configuration when carrying out the *in vivo* USF imaging of mice tumors.

2.3 Results and discussion

2.3.1 Fluorescence intensity profiles as a function of temperature

The relationship between the fluorescence intensity and temperature, or fluorescence profile, of ICG-PNIPAM nanoparticles in various sizes was studied, and the results are shown in Fig. 5(a). The fluorescence intensities were normalized to the strongest fluorescence emission among 4 curves. Fig. 5(b) lists vital factors, including the LCST, transition bandwidth, and ON/OFF ratio, for USF contrast agents. LCST was defined as the temperature point where the fluorescence intensity was increasing and reached 10 % of the ON/OFF fluorescence difference in the transition band, and the baseline was the average fluorescence intensity in the 'OFF' state. All the curves show significant increase in fluorescence intensity after the temperature is above their thresholds and obvious saturation when temperature is well above the thresholds. The curves shift along both directions, indicating that the size of the ICG-PNIPAM nanoparticles affected the fluorescence profiles. The LCSTs of ICG-PNIPAM rise from 33.8 to 37.8 °C with the increased quantity of SDS, except for PNIPAM-20mgSDS. 20 mg and 100 mg SDS-mediated nanoparticles exhibited a similar background fluorescence level ('OFF' state). The PNIPAM-200mgSDS had the narrowest transition bandwidth of 6.5 °C and the highest fluorescence ON/OFF ratio of 3.38 folds. The PNIPAM-100mgSDS, and PNIPAM-200mgSDS were favored for *in vivo* applications because the switch-ON temperature thresholds were close to or slightly above body temperature. After being introduced into the body, these nanoparticles can be switched 'ON' more efficiently than those with lower temperature thresholds during USF imaging.

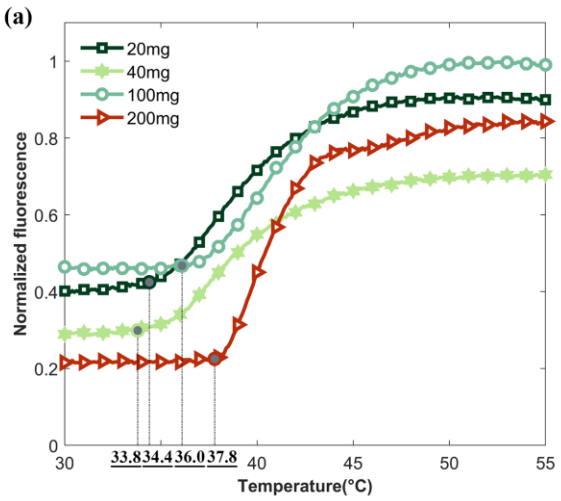

(b)

Sample	LCST (°C)	Transition Bandwidth (°C)	On/off Ratio
PNIPAM-20mgSDS	34.40	11.80	~2.07
PNIPAM-40mgSDS	33.80	12.80	~2.25
PNIPAM-100mgSDS	36.00	12.50	~2.08
PNIPAM-200mgSDS	37.80	6.50	~3.38

Figure 5 LCST determination of PNIPAM nanoparticles. (a) Correlation between fluorescence intensity and temperature for ICG-PNIPAM nanoparticles synthesized with various quantities of SDS. (b) Detailed comparison summarized in the table.

2.3.2 USF imaging in tissue-mimic phantoms

A silicone tube was filled with ICG-PNIPAM nanoparticles of different sizes, and USF imaging was conducted to compare their performance under the same experimental conditions. The water bath temperature was maintained at body temperature using a temperature controller (PTC10, Stanford Research Systems, USA). Figs. 6(a-d) show the distributions of the four types of nanoparticles in the tube with good target-to-background contrasts. The results are similar. Briefly, the SNRs were between 24.36 and 27.16 dB, and full width at half maximum (FWHM) values varied from 1.57 to 2.00 mm as listed in Fig. 4. There were no significant differences in their USF performances when switching ON in the phantom set-up, implying no size-dependent difference in their USF performance. In this experiment, the temperature of the water bath was kept at 37.5 °C so that the USF nanoprobes with the lower LCSTs might be partially switched on already by the water bath before ultrasound exposure. This may help explain why no obvious size-dependent USF differences were observed in the tissue-mimicking phantom experiments.

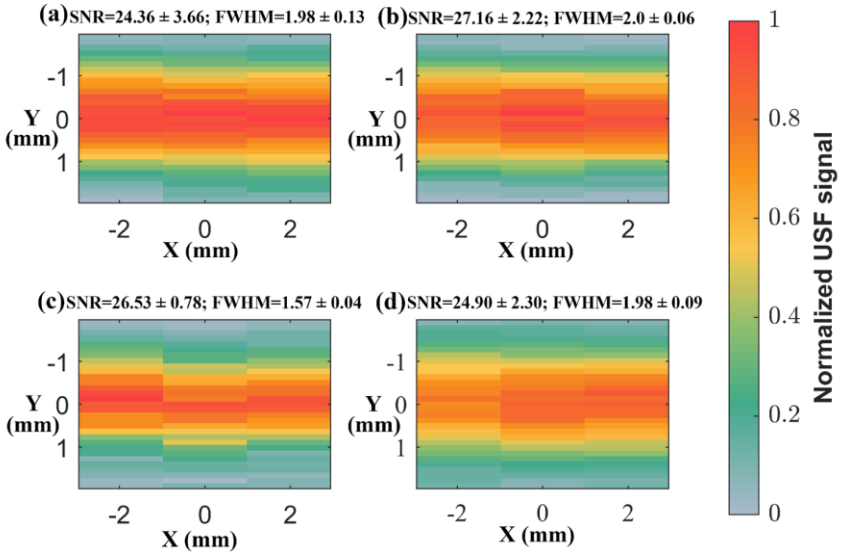

Figure 6 The USF imaging of blood vessel-mimicking silicone phantom. Silicone tube filled with (a) 20, (b) 40, (c) 100, and (d) 200 mg SDS-mediated nanoparticles. The SNR and FWHM of each scanned USF images were also evaluated and highlighted.

2.3.3 USF imaging in mouse muscles via local injections

The solutions of ICG-PNIPAM nanoparticles with different sizes were respectively injected into the muscles of the hind legs of mice to evaluate the USF imaging capability. As shown in Fig. 7, the 3D distribution of the nanoparticles in each case has been successfully imaged.

First, this indicates that the switching 'ON' property of size-varying ICG-PNIPAM probes was retained in real biological environments. Second, the volume of each USF image for PNIPAM-20mgSDS, PNIPAM-40mgSDS, PNIPAM-100mgSDS and PNIPAM-200mgSDS is 46.41, 35.51, 49.17, and 29.05 mm^3, respectively, which is much larger than the volume (~15 mm^3) of the injected nanoparticle solution in each case. This is mainly due to the transport of the nanoparticles via a convection mechanism induced by the syringe pressing. The diffusion of nanoparticles into the surrounding tissue after the injections during USF imaging may be minor due to the large size of the nanoparticles (i.e., tens to hundreds of nanometers). In addition, the transport of nanoparticles depends on the local microenvironments, and therefore the USF images show different distribution profiles in the 4 cases [43].

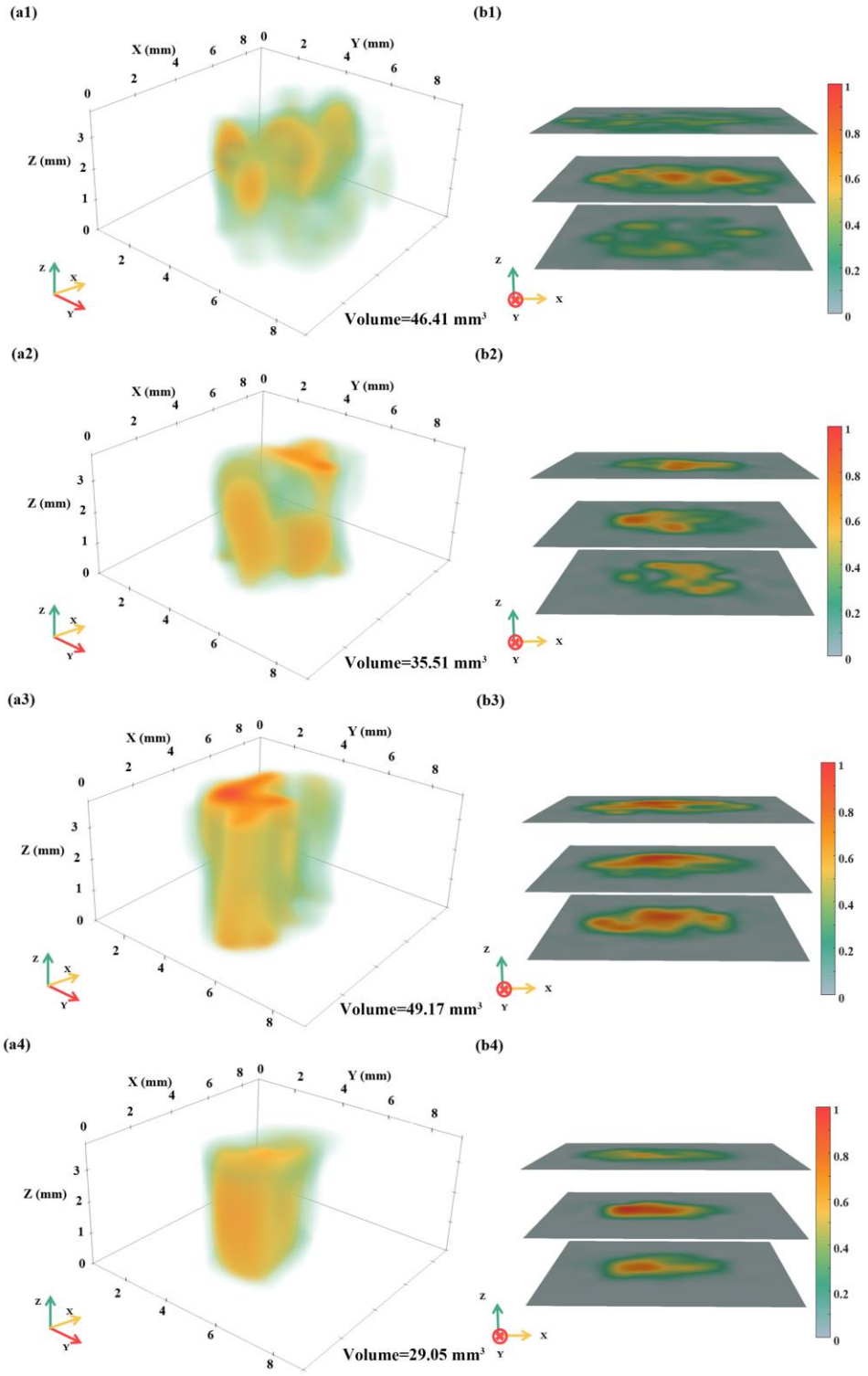

Figure 7 (a1-4) The normalized USF images of ICG-PNIPAM distribution when locally injected into mouse leg muscle. A 30 % threshold was applied when calculating the volume. (b1-4) Three stacks of 2D USF images from

top, middle, and bottom layer along z axis. (a1) (a1) (b1), (a2) (b2), (a3) (b3) and (a4) (b4) are 3D reconstructed USF images for nanoparticles synthesized with 20, 40, 100, and 200 mg SDS.

The USF data in Figs. 7(a1-a4) are further displayed in 2D image slices as shown in Fig. 8. Each slice is a 2D image on the XY plane at a specific depth of Z. When Z increases from zero to a positive number, the ultrasound focus is scanned from a deep layer to a shallow one (i.e., close to the tumor skin). Figure 8 shows the USF results for local injections of 10-15 μL ICG-PNIPAM nanoprobes to the mouse leg muscle. Based on these USF image slices, it is clear that the nanoprobes are relatively concentrated in the scanning areas and mainly centered at the injection locations. This conclusion indicates that the diffusion of these nanoagents in tumors is low.

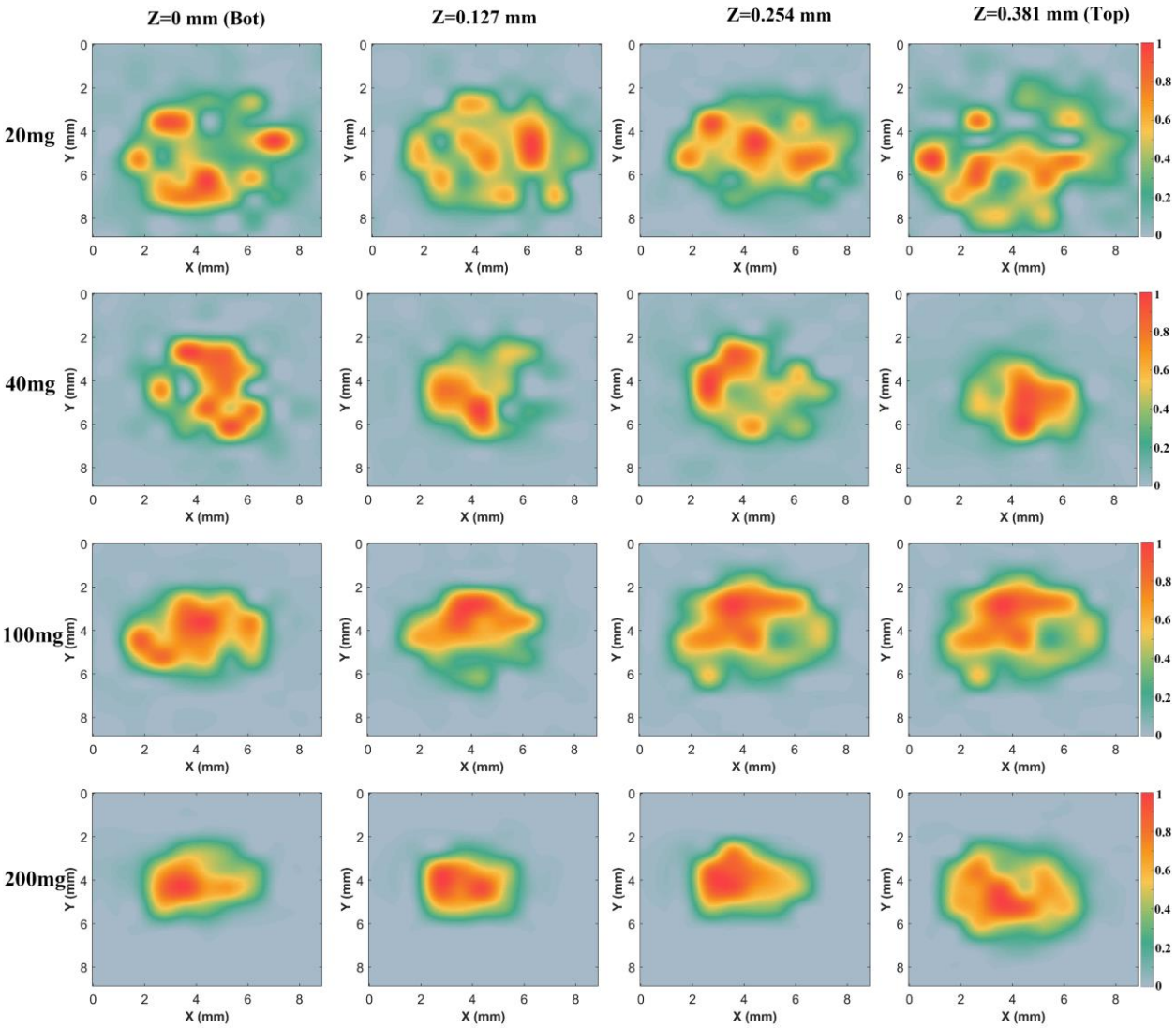

Figure 8 The normalized 2D USF images obtained after local injections of size-varying nanoprobes with 20, 40, 100, and 200 mg SDS. These images were linearly interpolated 15 times in the XY plane.

2.3.4 In vivo biodistribution analyses of the probes in BxPC-3 tumor-bearing nude mice

Biodistribution studies (Fig. 9) show that contrast agents dispersed throughout the mouse body immediately after an injection, and superficial vasculatures were visible. Strong fluorescence emission from the bladder appeared at one h post-injection and decreased significantly when observed at 2 h, suggesting that a portion of the nanoparticles was cleared rapidly by the renal excretion. The kidney is the primary organ responsible for renal

clearance, but the hydrodynamic sizes of all proposed nanoprobes were above 58 nm, much larger than the kidney filtration threshold (6-8 nm) [44]. This is probably because contrast agents were partially dissociated into small fragments by the macrophages in the body and then excreted by the renal routes [45]. This fast renal excretion can be a favorable advantage to reduce systemic toxicity, because a fraction of nanomaterials was cleared quickly and further uptake by the reticuloendothelial system (liver and spleen) can be mitigated. Meanwhile, the fluorescence from the spleen increased gradually with time (left-side view), and this phenomenon was especially obvious with PNIPAM-20mgSDS and PNIPAM-200mgSDS. Further analyses of harvested organs also supported the reticuloendothelial system and lungs being responsible for the uptake of most of the ICG-PNIPAM. For the PNIPAM-40mgSDS and PNIPAM-100mgSDS samples, the accumulations in the lungs were the highest. The lung serving as a biomedical filter receives not fractional, but the total cardiac output. Its pulmonary ultrastructure occupies ~25-30 % of the total endothelial surface area in the body [46], and thus there will be a high chance of nanoparticles-endothelial contacts in the vasculature of the lung. All features mentioned above facilitate the accumulation of nanoparticles in lungs. Also, such a small size of proposed nanoprobes allows for close contact with the endothelium of the mouse lung which has an average diameter of 5 μm, and nanoparticles are likely to be trapped by the ultrastructure afterwards [47]. Overall, as shown in Figs. 9 and 10, the accumulation of both nanoparticles with 20 mg and 200 mg SDS in the liver and spleen were dominant at 24 h post-injection, whereas nanoparticles synthesized with 40 mg and 100 mg SDS accumulated the most in the lungs of mice. However, while imaging organs under the 2D fluorescence camera, their volume effects cannot be neglected. For instance, the volume of the liver was the largest compared with other organs such as the spleen and lung, and the fluorescence signal was possibly biased by the volume effects because it was summed up longitudinally from a thicker volume.

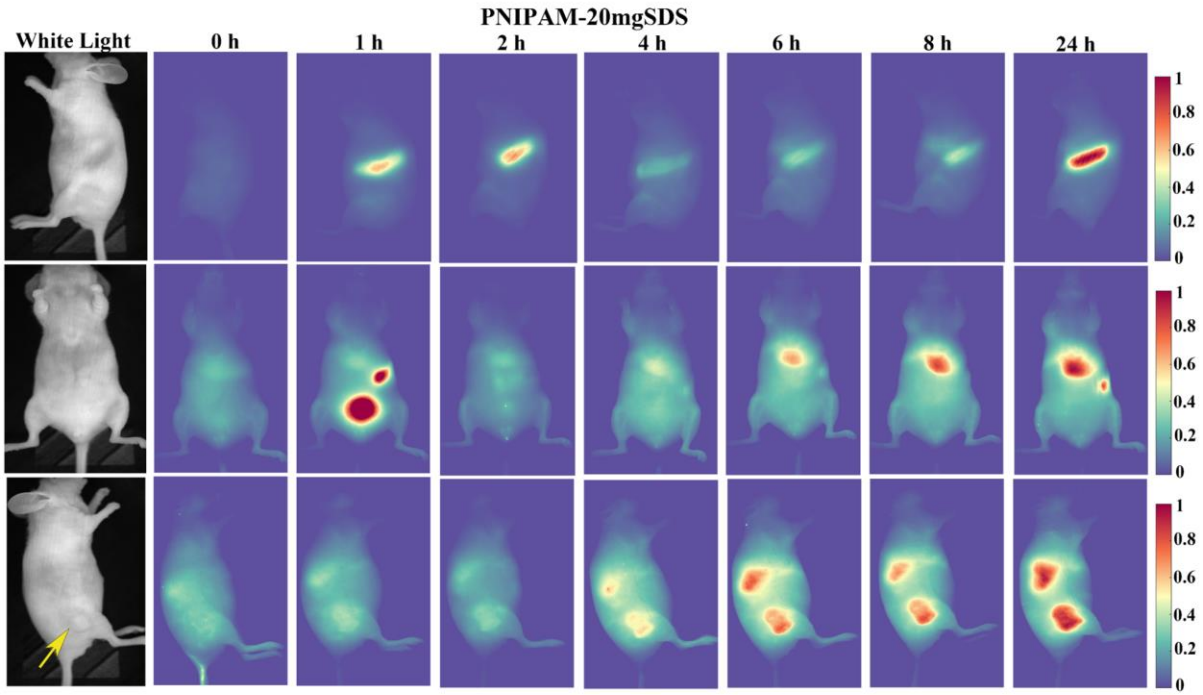
PNIPAM-20mgSDS
White Light
0 h
1 h
2 h
4 h
6 h
8 h
24 h
1
0.8
0.6
0.4
0.2
0

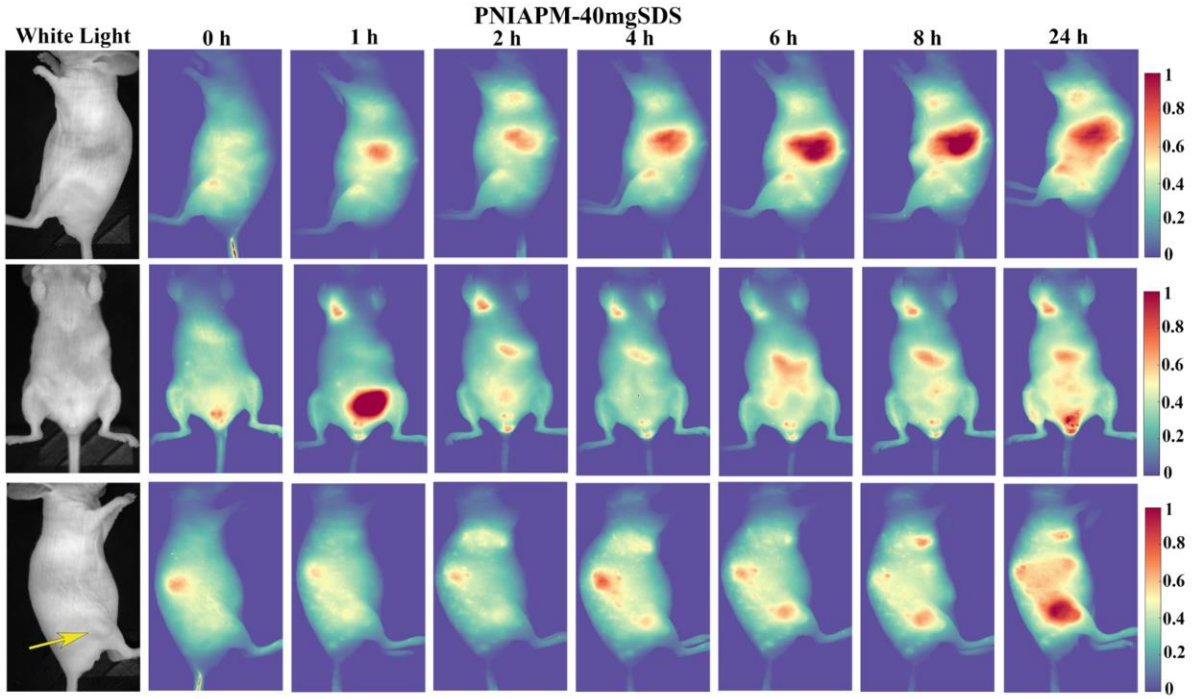
PNIAPM-40mgSDS
White Light
0 h
1 h
2 h
4 h
6 h
8 h
24 h
1
0.8
0.6
0.4
0.2
0

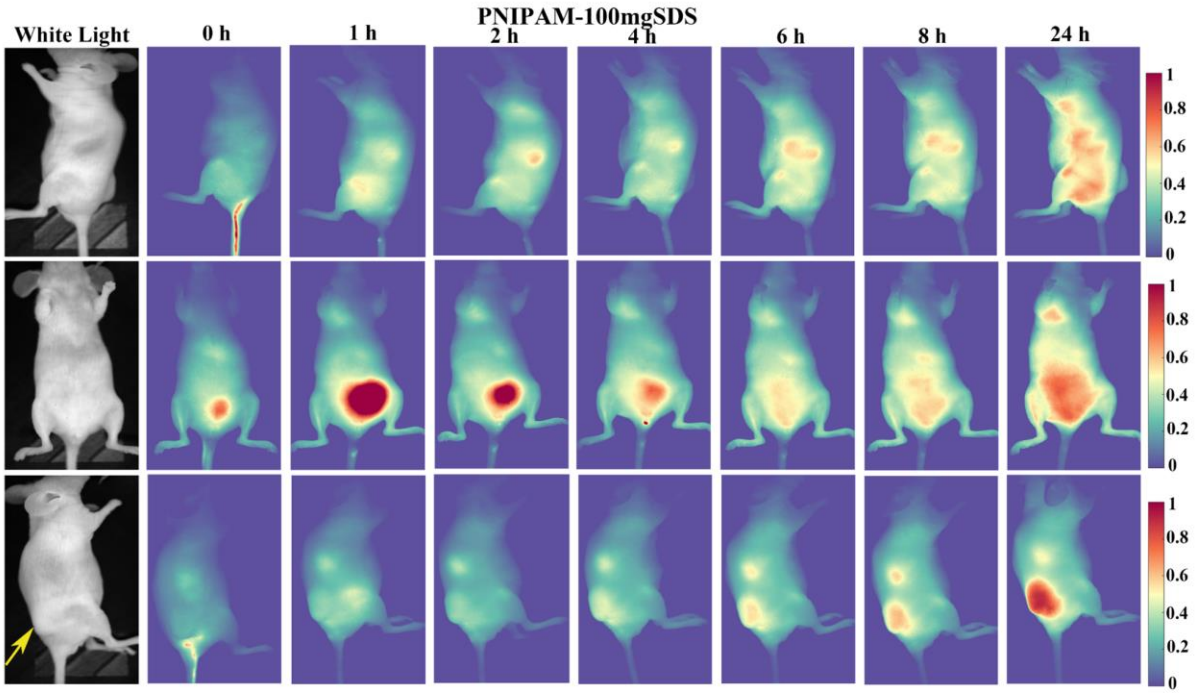
PNIPAM-100mgSDS
White Light
0 h
1 h
2 h
4 h
6 h
8 h
24 h
1
0.8
0.6
0.4
0.2
0

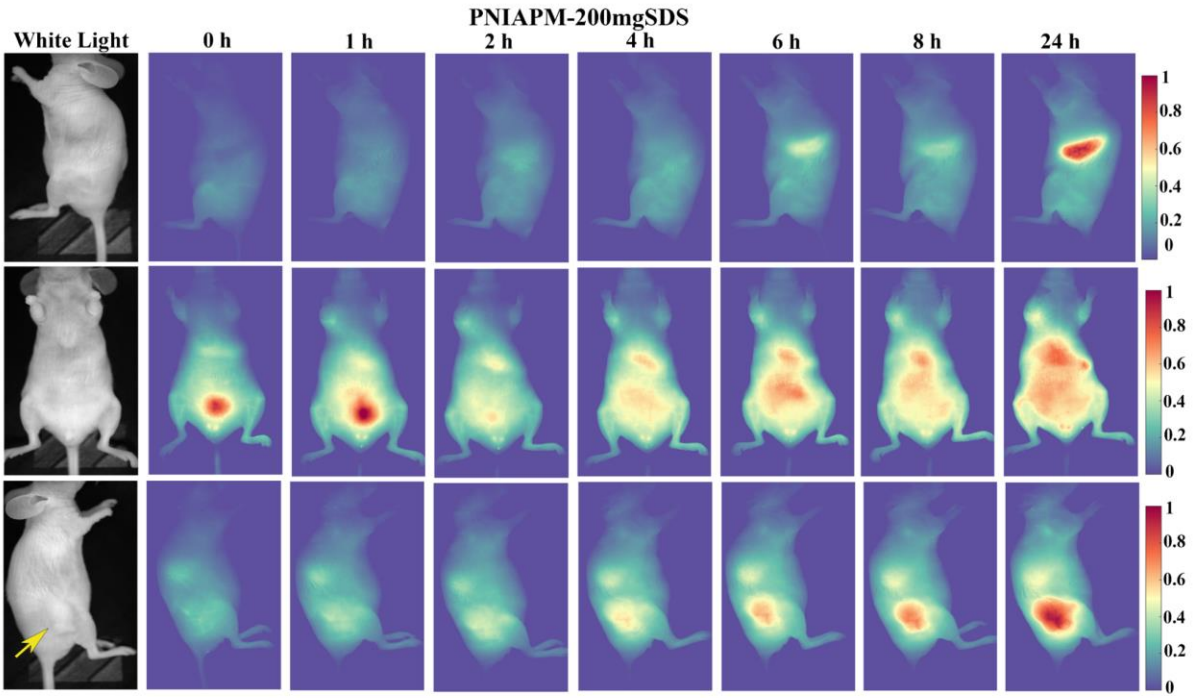

Figure 9 The biodistribution results for ICG-PNIPAM-NPs. 2D fluorescence images captured over 24 h, including left-side view (top), ventral view (middle) and right-side view (bottom). 0 h images were acquired immediately after the i.v. injection. Tumor area is indicated by the yellow arrow.

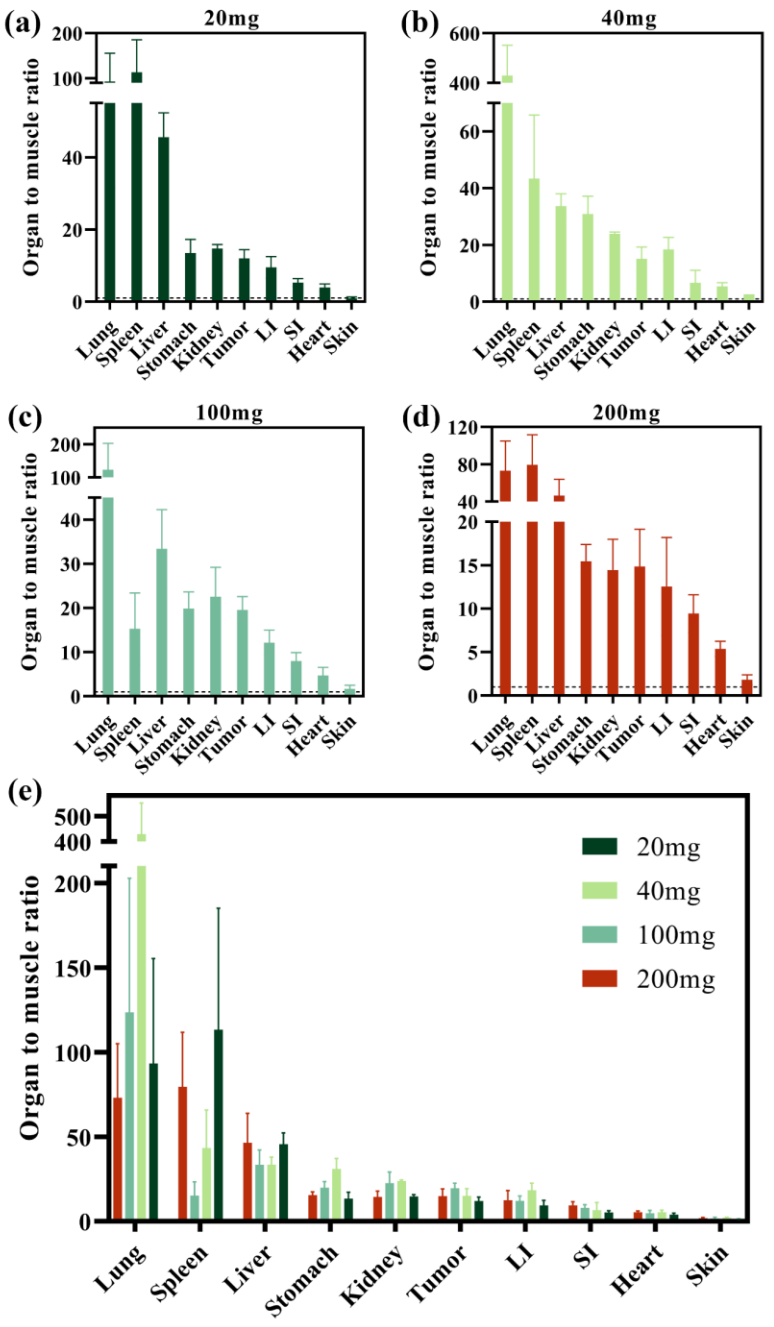

Figure 10 The organ to muscle ratios. (a), (b), (c), and (d) correspond to PNIPAM-20mgSDS, PNIPAM-40mgSDS, PNIPAM-100mgSDS and PNIPAM-200mgSDS respectively (n = 3 for each group). LI=large intestine; SI=small intestine. The horizontal dash line at 1 represents the fluorescence level of mouse muscle. (e) presents the summarized organ to muscle ratios for all groups.

The NIR fluorescence ratio between tumor and normal tissues (T/N ratio) was analyzed over a 24 h period. Figure 11 illustrates that the T/N ratio grows with time from approximately 1.2 to 2.2 folds for all-sized ICG-PNIPAM nanoparticles. The enhanced fluorescence signals in tumors and suppressed background could be attributed to several factors. First, the emission band of ICG-PNIPAM was in the NIR band where the autofluorescence of biological tissue is low, so the background fluorescence is also relatively low. Furthermore, the prolonged circulation time is sufficient for particles to flow through tumor-associated blood vessels and then specifically retain in the tumor area via EPR effects [48]. Also, the nanoparticle concentration gradient between the vascular space and extravascular tissue may remain a high value for a long time period, which is beneficial for nanoparticles to diffuse into extravascular spaces of tumors.

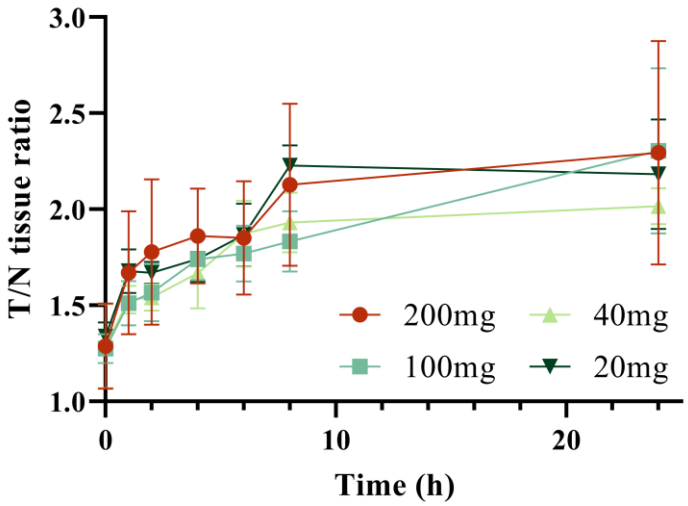

Figure 11 The T/N ratio as a function of time after an i.v. injection of size-varying contrast agents. Data are presented as mean ± s.d. (n = 3).

It is often believed that nanoparticles with a size of 100-200 nm are good candidates for passive tumor site targeting as they are likely to escape from the filtration traps of the liver and spleen. The permeability of tumor blood vessels for large nanoparticles (>200 nm) may be limited, while small nanoprobes (<100 nm) may possibly diffuse back to the blood circulation system and comprise the tumor retention [49], [50]. However, in this study, there is no dramatic variation observed in tumor accumulation for the adopted nanoparticles. Both ICG-PNIPAM

with the smallest size of 58 nm and the largest size of 321 nm demonstrated acceptable tumor-to-background ratios after 24 h as shown in Fig. 9. One possible reason could be the tumor volume differences in each mouse tumor xenograft model. Previous studies demonstrated that tumor volume affects the physiological environment and selectively changes the uptake of differently sized gold nanoparticles [50]. Size is not the only factor determining the EPR effects, and many other critical factors also exist [51]. For example, nanomaterials with a positive surface charge can be bound to the vascular endothelial cells, which leads to a rapid decrease in the concentration of free nanoparticles in the blood circulation and thus a reduction in tumor retention via the EPR mechanisms [52]. Therefore, when comparing the tumor accumulation of nanoparticles of different sizes, it is important to consider the impacts of the physiological environment and nanomaterials' chemical characteristics.

2.3.5 In vivo NIR-USF imaging of BxPC-3 tumor via a tail vein injection

Based on the results of biodistribution tests, a considerable quantity of ICG-PNIPAM could accumulate in the BxPC-3 tumor. The feasibility of conducting USF imaging in the tumor microenvironment using ICG-PNIPAM nanoparticles was examined. Figs. 12(a1-a4) show the 2D planar fluorescence images directly acquired from the camera of four tumors injected with the four different USF nanoparticles (20, 40, 100, and 200 mg SDS). The square on each figure indicates the USF scanning area and the dashed line shows the outline of the tumor. Similarly, Figs. 12(b1-b4) display their 3D USF images, indicating the distribution of USF signals (or contrast agents). Figs. 12(c1-c4) provide three slices of each 3D image in Figs. 12(b1-b4) for the four tumors. Obviously, the 2D images in Fig. 12(a) show a projection of the emission photons along the imaging direction (Z direction). Thus, fluorophores overlap axially (Z direction) and cannot be differentiated. In contrast, USF images in Figs. 12 (b-c) clearly provide depth resolution to allow the differentiation of fluorophores along depth direction (z direction). Figure 12(c) indicates that USF signals and agents are distributed non-uniformly on different slices. Similar results can be found on the lateral (XY) planes. In Fig. 12(a1), some USF scanning areas are not occupied by the tumor. The corresponding 3D USF images validate this result by showing strong USF signals in the tumor areas and either no signal or a weak USF signal in non-tumor areas (Figs. 12(b1) and (c1)). For the other three examples, although the majority of the scanning areas are in the tumors based on Figs. 12(a2-a4), their USF images show the heterogeneous distribution along both lateral (X, Y) and axial (Z) directions, which is quite different from the 2D images in Figs. 12(a2-a4) in which images are much smoother due to the light scattering and fluorescence signal overlapping. These

results further indicate that USF has much higher resolution than the optical method when imaging deep tissues. Thus, the USF distribution profiles can be used to infer more detailed information on the distribution of the contrast agents in the tumor microenvironment.

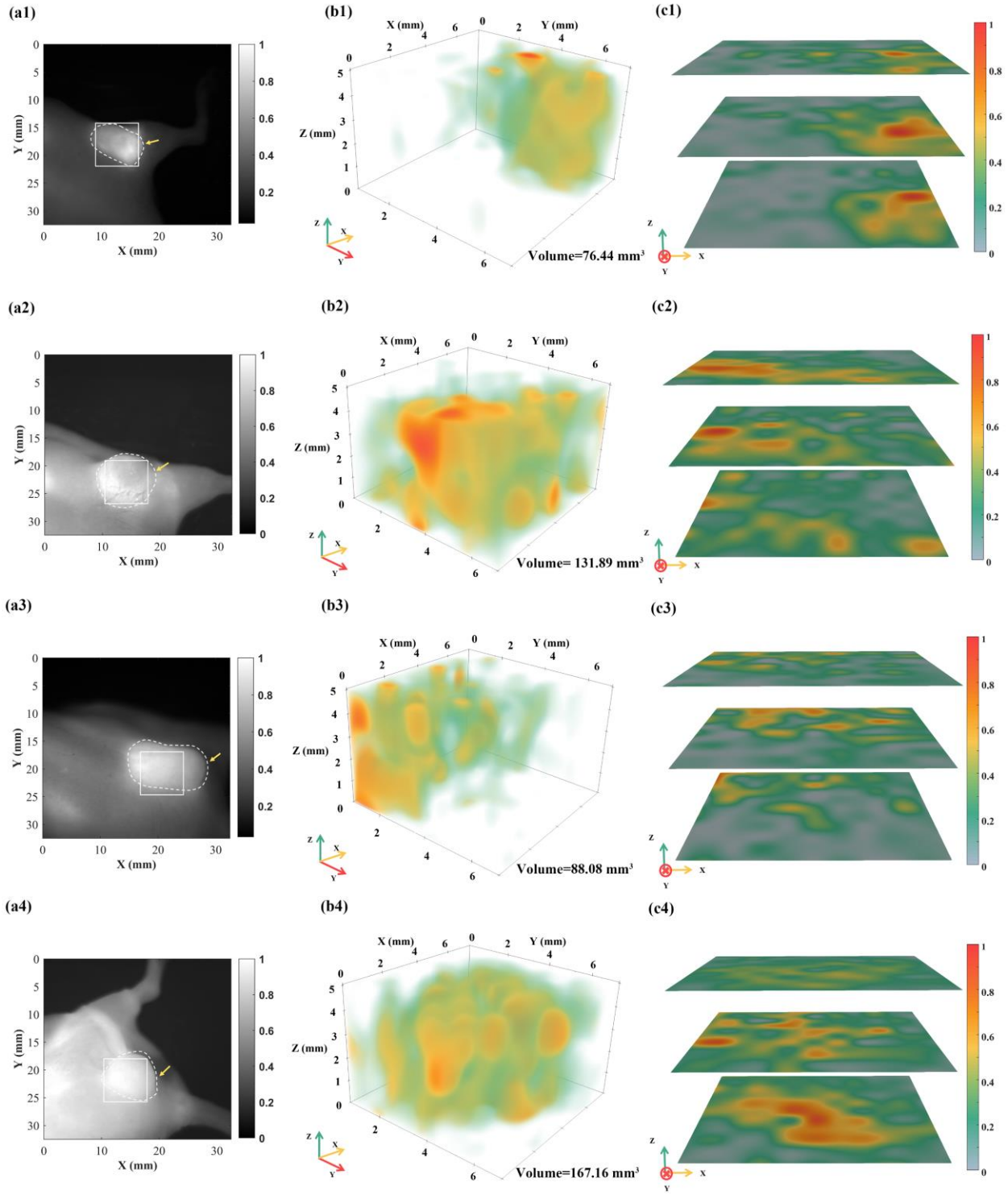

Figure 12 (a1-4) 2D fluorescence images of the BxPC-3 pancreas tumor-bearing mouse, and the tumor area is indicated by the dashed circles and yellow arrow. Scan area is represented by the white box. (b1-4) The reconstructed 3D USF image of the tumor. Volume was calculated with a threshold of 30 %. (c1-4) Three layers of

2D USF images along z axis (top, middle, and bottom). (a1)(b1)(c1), (a2)(b2)(c2), (a3)(b3)(c3), and (a4)(b4)(c4) are for contrast agents synthesized with 20, 40, 100, and 200 mg SDS respectively.

The USF data in Figs. 12(a1-a4) are further displayed in 2D image slices as shown in Fig. 13. Each slice is a 2D image on the XY plane at a specific depth of Z. These images show that the nanoprobes are relatively more dispersed and scattered than those in Fig. 8. This is understandable because the nanoprobes are distributed much more widely in the tumors via i.v. injections than via local injections.

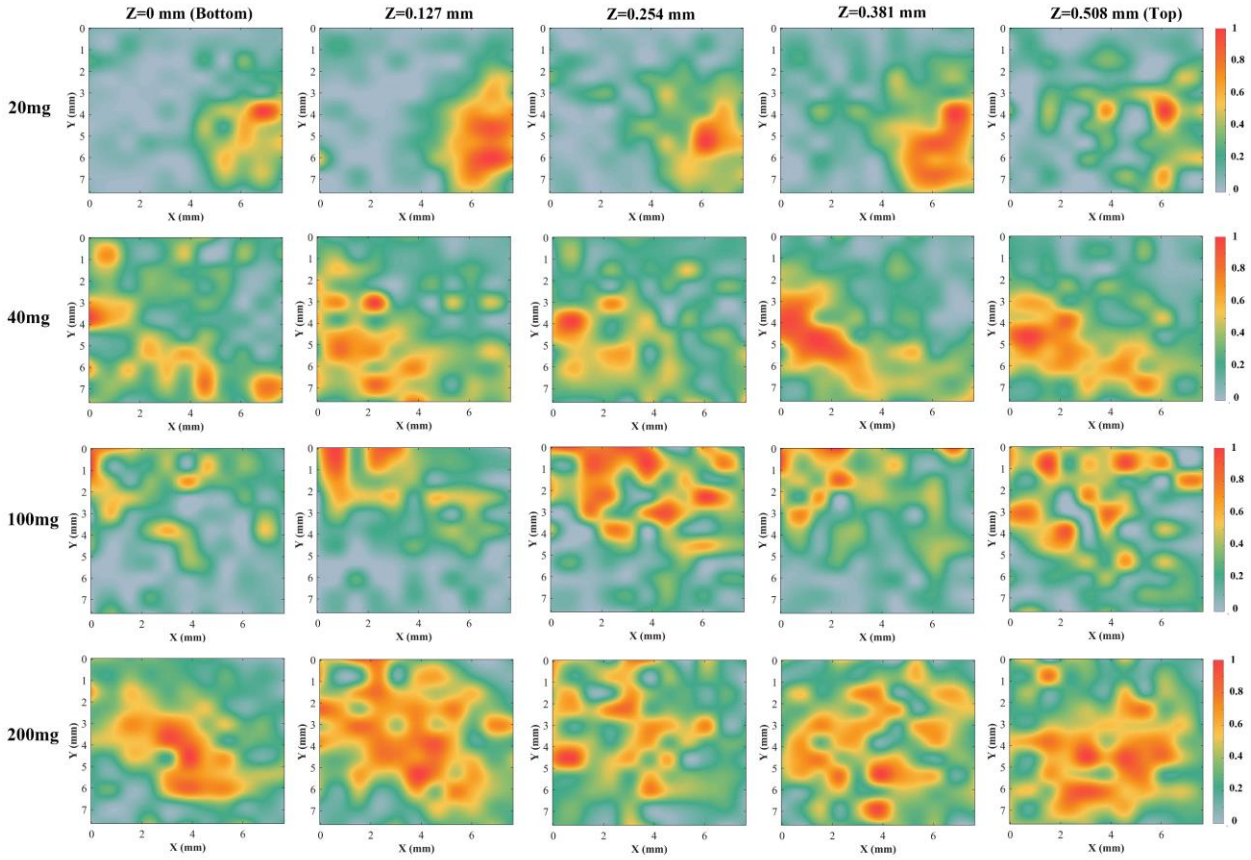

Figure 13 The representative USF images of BxPC-3 tumor area via the i.v. administration of ICG-PNIPAM contrast agents with 20, 40, 100, and 200 mg SDS. Data were linearly interpolated 15 times along both X and Y directions.

All sizes of ICG-PNIPAM nanoparticles exhibited acceptable USF signals, further confirming the preferred passive accumulation of stable nanoprobes rather than free ICG molecules in the tumor sites. The successful *in vivo* USF signals also imply that the tumor microenvironments, such as hypoxia and low PH, did not dramatically affect the thermal-responsive features of proposed ICG-PNIPAM nanoparticles. The LCSTs of different-sized nanoprobes were close to the body temperature, and contrast agents could be easily switched 'ON' by the FU. All the above mechanisms may be present and contribute to the *in vivo* USF imaging in the tumor.

Although all four types of nanoparticles show the successes of *in vivo* USF imaging via i.v. injections, comparisons of the USF images among the four nanoparticles should be made cautiously. Because the location and axial thickness of tumors, and therefore the applied FU power and MI are different. The MI adopted in Figs. 12(b1-b4) were 3.63, 5.57, 8.19, and 5.75, respectively. Usually, for thick tumors or tumors surrounded by thick tissues, high ultrasound power (or MI) is needed to reach good USF SNR. Because ultrasound waves were attenuated by unknown reflection, scattering, and absorption when traveling a long distance before reaching the tumor. In this study, to reduce the imaging time all the ultrasound exposures were limited to as short as 400 ms. This is also one of the reasons that a high ultrasound power and MI were needed. Appropriately increasing the ultrasound exposure time may be an efficient way to reduce ultrasound power and MI. However, this will sacrifice the imaging speed and spatial resolution due to thermal diffusion. An ultrasound array that can simultaneously generate multiple foci combined with a Z-scanning method developed in our previous publication [9] can be an alternative way to improve the temporal resolution. This method is currently being investigated in our laboratory, and preliminary data indicate a success and will be published in future.

2.3.6 Further discussions about USF features and current barriers

USF can be applied to different types of tumors. In this study, pancreatic tumors were selected as an example. Several studies have investigated BxPC-3 human pancreatic carcinoma xenograft-bearing nude mice models via PET [53], [54] and MRI imaging [55]. PET images can investigate tumor activeness, however, the involving of radiotracers in PET poses both health and environmental risks and is highly regulated, while NIR fluorescence and USF imaging do not require any ionizing radiation exposure. MRI provides detailed anatomical information and depicts the morphology of tumors, but its sensitivity to contrast agents is relatively low compared

with optical imaging in the NIR window. More unique features of USF imaging can be found in our previous publications [8], [9], [30], [34], [36], [37], [41], [42] and will be explored and reported in the future.

Increasing the signal strength of USF contrast agents and the sensitivity of the detection system can reduce the required ultrasound strength. The biocompatibility of USF contrast agents is another major barrier to clinical use. A cell study revealed that the PNIPAM nanoparticles are biocompatible when concentrations are at or below 5 mg/mL [56]. In contrast, the NIPAM monomers exhibited a significant cytotoxicity level when compared to their respective polymer forms (PNIPAM) [57]. Therefore, future efforts may focus on reducing the residual monomers within polymers by extending the dialysis duration or exploring alternative in *vivo* USF agents with higher biocompatibility, such as PEG and liposomes [58], [59]. In addition, targeted delivery of nanoparticles to the tumor may be another way to reduce the barrier by limiting the injection dose due to the high attaching efficiency.

2.4 Conclusion

In this paper, for the first time, the goal of *in vivo* 3D tumor USF imaging via i.v. injections was achieved. The size of PNIPAM-based USF contrast agents was controlled by adjusting the quantity of SDS, and the average size ranged from 58 nm to 321 nm. Furthermore, USF imaging in both *ex vivo* blood vessel phantoms and *in vivo* mice models were demonstrated. Our biodistribution results showed the high contrast and passively targeted imaging of tumors possibly via EPR effects. Later, *in vivo* 3D USF imaging in the tumor with a good SNR and a tumor-to-background contrast was achieved, which is beneficial for diagnosis and therapeutic interventions, suggesting a potential high resolution tumor imaging at a depth of centimeters. Further efforts to improve this technology include developing stable and more biocompatible agents, reducing ultrasound power while retaining acceptable USF SNR, and further improving the temporal resolution of the current imaging system. All these efforts will push this technology toward adoption in pre-clinical and clinical applications for high-resolution deep-tissue fluorescence imaging.

Chapter 3 NONINVASIVE MEASUREMENT OF LOCAL TEMPERATURE USING ULTRASOUND-SWITCHABLE FLUORESCENCE

3.1 Introduction

Tissue temperature is largely dependent on cell metabolism and local blood flow. For example, most solid tumors generate more heat than surrounding healthy tissues due to increased vascularization and metabolic activity [60]. It has been examined that the temperature of lung, bladder, and breast tumors often had a 1-2 °C higher temperature than the surrounding healthy tissues [27], [61]–[63]. In cancerous breast tissue, there are two main changes in temperature: (1) an elevated absolute temperature in the tumor area, and (2) a distorted spatial distribution of temperature, with oscillations around the tumor boundary [64].

These results stimulated researchers to consider temperature as an indicator of tumor physiological activeness for screening and/or diagnosis purposes. It directly led to the prevalence of breast thermography for breast cancer screening in the 1960s -1980s [61], [64]–[67]. However, thermography failed in the competition with x-ray-based mammography eventually [68]. The issue with thermography lies in its reliance on infrared photon detection within a wavelength spectrum of approximately 3-10 microns for imaging temperature. In cases where these infrared photons generated from deep breast tissues are completely absorbed by water molecules present in the tissue, leading to a complete loss of information beneath the skin. Unfortunately, the absolute value of the surface temperature is not specific to the tumor's activeness and can be affected by many other factors [69], [70]. Thus, breast thermography diagnosis based on skin surface temperature is neither specific nor sensitive to tumor activeness for diagnosis purposes.

In contrast, x-ray-based mammography can visualize tissue well beyond the skin and provide clear anatomic or structural information of tumors, which were much more specific and sensitive than thermography. However, over the years since the adoption of mammography for breast cancer screening, many shortcomings have been realized, such as possible overdiagnosis, using ionizing radiation, uncomfortable patient experience due to significant compression of patient's breasts, low specificity (especially for small lesions and women with dense breasts), and lack of physiological or functional information [71]–[73].

Based on the discussion above, it is speculated that the measurement of local tumor temperature and its gradient, beneath the surface of the breast, could serve as a valuable tool for assessing tumor activeness and offering risk stratification. This could potentially identify subsets of women, particularly those with small lesions or dense breast tissue, which may reduce the need for biopsy and mitigate overdiagnosis. Unfortunately, even today this indicator still cannot be fully adopted due to several challenges of current technologies: (1) limited temperature sensitivity and (2) difficulty to measure the absolute local tissue temperature. Temperature sensitivity can be quantified by the percent of signal change when temperature increases by one degree (°C). In MRI-based thermometry, temperature sensitivity is < 2% per °C in the spin-lattice relaxation method, which leads to a limited temperature resolution of ~1 °C in a clinical scanner and ~0.3-0.5 °C in a pre-clinical scanner with a strong magnetic field [74]–[76]. Ultrasound-based thermometry has even lower temperature sensitivity (~0.05% per °C) and temperature resolution [77]. Photoacoustic-based thermometry has relatively higher sensitivity (~4-5% per °C), but this sensitivity is still very limited [78]–[83]. In addition, most technologies aim to image the relative change in tissue temperature induced by externally applied energy (such as high intensity FU or other radiation), including MRI-, ultrasound-, and photoacoustic-based thermometry, but imaging local background temperature in tissues is much less investigated [83].

To overcome these limitations in thermography, thermometry, and mammography, a new, sensitive, and robust method based on our USF technology was developed [8], [36], [84]–[86]. ICG, an FDA-approved NIR fluorophore, was encapsulated into nanometer-sized liposomes (ICG-liposomes), which showed excellent temperature sensitivity and has been demonstrated as an excellent USF imaging agent [30], [31]. A unique feature of this type of USF agent is that the fluorescence intensity can increase ~2-3 times when temperature rises ~2-3 °C. Thus, it leads to an 'OFF–ON' switch in fluorescence in a narrow range of the temperature rise, and further provides a significantly high temperature sensitivity, >100% per °C [30], [31]. More importantly, this method enables the direct quantification of tissue's absolute temperature. These features make it an ideal technology to map tumor subtle temperature variations. In this study, a blood vessel-mimic phantom was adopted. The USF-based thermometry shows good agreement with IR thermal imaging and the average difference is 0.64 ± 0.43 °C. The success of this study provides evidence for the feasibility of USF-based thermometry as a potentially viable technique for non-invasive measurement of local tissue temperature.

3.2 Operation principles experimental setup

3.2.1 Principle of background temperature measurement

Liposome-based USF contrast agents typically exhibited a sharp fluorescence transition from an off to an on state when the environmental temperature rises above a threshold, the LCST [20,64]. Thus, their fluorescence-vs-temperature profiles exhibited characteristics similar to sharp step functions. In USF imaging, to avoid liposomes being switched on by surrounding tissue, the LCST was usually controlled slightly above the background tissue temperature. To externally switch on the fluorophores, an ultrasound pulse was usually applied to increase the tissue temperature in its focal volume above the LCST. These ultrasound-induced fluorescence photons were called USF signal. In addition, the threshold (i.e., the LCST) could be easily controlled by adjusting the lipids compositions of the outer liposomal shell. It is speculated, based on these studies, that the ultrasound heating speed might be estimable and the background temperature might further be estimated based on the USF signal, if two liposomes with distinct LCSTs were synthesized and mixed. The second threshold ($LCST_2$) is higher than the first one ($LCST_1$) but both LCSTs are higher than tissue background temperature (T_t). When the ultrasound pulse is applied, the temperature in the focal volume increases from the background temperature, passing the $LCST_1$, and eventually to somewhere above $LCST_2$. When the temperature rises somewhere above $LCST_1$ but below $LCST_2$ (denoted as T_a) at time t_a, it is expected to observe the first quickest increase in the USF signal, which is mainly generated from the first liposome. This indicates that the temperature in the focal volume reaches the value (T_a) that corresponds to the highest slope of the step function of the fluorescence-vs-temperature profile curve of the first liposome.

When the temperature further increases above the $LCST_2$, the second liposomes will be switched on, leading to a further increase in USF signal. Similarly, when the temperature reaches somewhere above the $LCST_2$ (denoted as T_b) at time t_b, it is expected to observe the second quickest increase in the USF signal, which is primarily generated from the second liposome. T_b is the temperature where the highest slope of the fluorescence-vs-temperature profile curve of the second liposome is reached.

By analyzing these speed changes in the USF signal, the specific time points (t_a and t_b) can be identified. Based on the assumption that the tissue temperature in the ultrasound focal volume reaches T_a at t_a and T_b at t_b, a linear heating speed can be calculated as $V_h=(T_b-T_a)/(t_b-t_a)$. If the thermal diffusion can be ignored during the heating due to the short ultrasound exposure, the tissue background temperature (T_t) can be calculated as $T_t=T_a-$

$V_h*(t_a-t_0)=T_b-V_h*(t_b-t_0)$, where t_0 is the time when the ultrasound pulse is initiated and usually can be set as zero if the system is synchronized by the trigger. In practice, T_t can also be equivalently calculated via a linear fitting based on the temperature-vs-time points (i.e., $[T_a, T_b]$ vs $[t_a, t_b]$) by extracting the intercept on the temperature axis, which indicates the background temperature right before the ultrasound exposure (i.e., $[T_t, t_0=0]$). Note that T_a and T_b (and LCSTs) can be independently found by measuring the characteristic curves of the fluorescence-vs-temperature profiles of the two liposomes and their mixture, and the two time points (t_a and t_b) can be found based on the rate of change of the dynamic USF signal.

3.2.2 Materials and liposome preparation

Ethanol and cholesterol were from Fisher Scientific International, Inc., USA. ICG was obtained from Chem-Impex Int'L Inc., USA. 1, 2-dipalmitoyl-sn-glycero-3-phosphocholine (DPPC) and 1,2-distearoyl-sn-glycero-3-phosphocholine (DSPC) were purchased from Avanti Polar Lipids, Inc., USA.

The liposomes were prepared via ethanol injection method [87]. 20 mg phospholipids (DPPC and DSPC) and 1 mg cholesterol were dissolved in 700 µL ethanol. The resultant organic phase was injected into 9 mL of ICG aqueous phase (0.06 mg/mL) under magnetic stirring at 1000 rpm. After stirring for 15 mins, the residual ethanol was removed by rotary evaporation under reduced pressure. The liposome suspension was then purified by ultracentrifugation (Avanti J-E, Beckman Coulter, USA) at 16,500 rpm for 25 min. In this study, the mass ratio of DPPC and DSPC is 1.5 for the first liposome (denoted by L) with a lower threshold $LCST_1$, while the lipids ratio is 0.6 for the second liposome (denoted by H) with a higher threshold $LCST_2$. The liposomal mixture was prepared with a volume ratio of L:H=1:4.

3.2.3 Characterizations methods

The hydrodynamic size and polydispersity index of the liposomal samples were obtained by a dynamic light scattering instrument (NanoBrook 90PlusPALS, Brookhaven Instruments, USA). All measurements were performed in triplicate at room temperature.

An in-house built spectrometer system was used to measure the fluorescence intensity with respect to temperature [41]. The fluorescent sample in a 3 mL quartz cuvette was placed into a temperature-controlled holder (Quantum Northwest, Inc., USA) and excited by an 808 nm laser (MGL-II-808-2W, Dragon Lasers, China). A

modular USB spectrometer (USB2000+, Ocean Inlight, USA) was used to acquire the spectra, and the fluorescence level was a sum of emission spectra beyond 830 nm.

3.2.4 Camera-based USF system

The experiments were carried out in the EMCCD camera-based USF system [9], [34]. Figure 14(a) shows the schematic diagram of the in vitro study of the thermometry system. Briefly, a silicone tube (Inner diameter = 0.30 mm; Outer diameter = 0.64 mm) embedded in the silicone phantom with a thickness of 4 mm was filled with thermosensitive agents and illuminated by the light beam from an 808 nm laser (MGL-II-808-2W, Dragon Lasers, China). The fluorescence passed through three long-pass filters (BLP01-830R-50/25, Semrock Inc., USA), and then was captured by an EMCCD camera (ProEM®-HS: 1024BX3, Princeton Instruments, USA) with a camera lens (AF NIKKOR 50 mm f/1.8D Lens, Nikon, Japan). A function generator (FG, 33500B, Agilent, USA) generated the driven voltage to a 2.5 MHz FU transducer (H-108, Sonic Concepts Inc., USA) after being amplified by a 50 dB-gain radio frequency power amplifier (RF-AMP, A075, E&I, USA) and then passing through the matching network (MNW). To provide independent validation of the temperature values, an IR camera (A300, Teledyne FLIR, USA) was also synchronized by receiving trigger signals from a pulse delay generator (PDG, P40, Highland Technology, USA) connected to the FG. The temperature of the water was controlled by a temperature controller system (PTC10, Stanford Research Systems, USA). The temperature probe submerged in the water was placed near the tube to get a close estimation of the temperature of the USF agents. A magnetic stirrer with a magnetic bar (11-100-16S, Fisher Scientific, USA) was used to ensure a relatively uniform temperature distribution in the water tank.

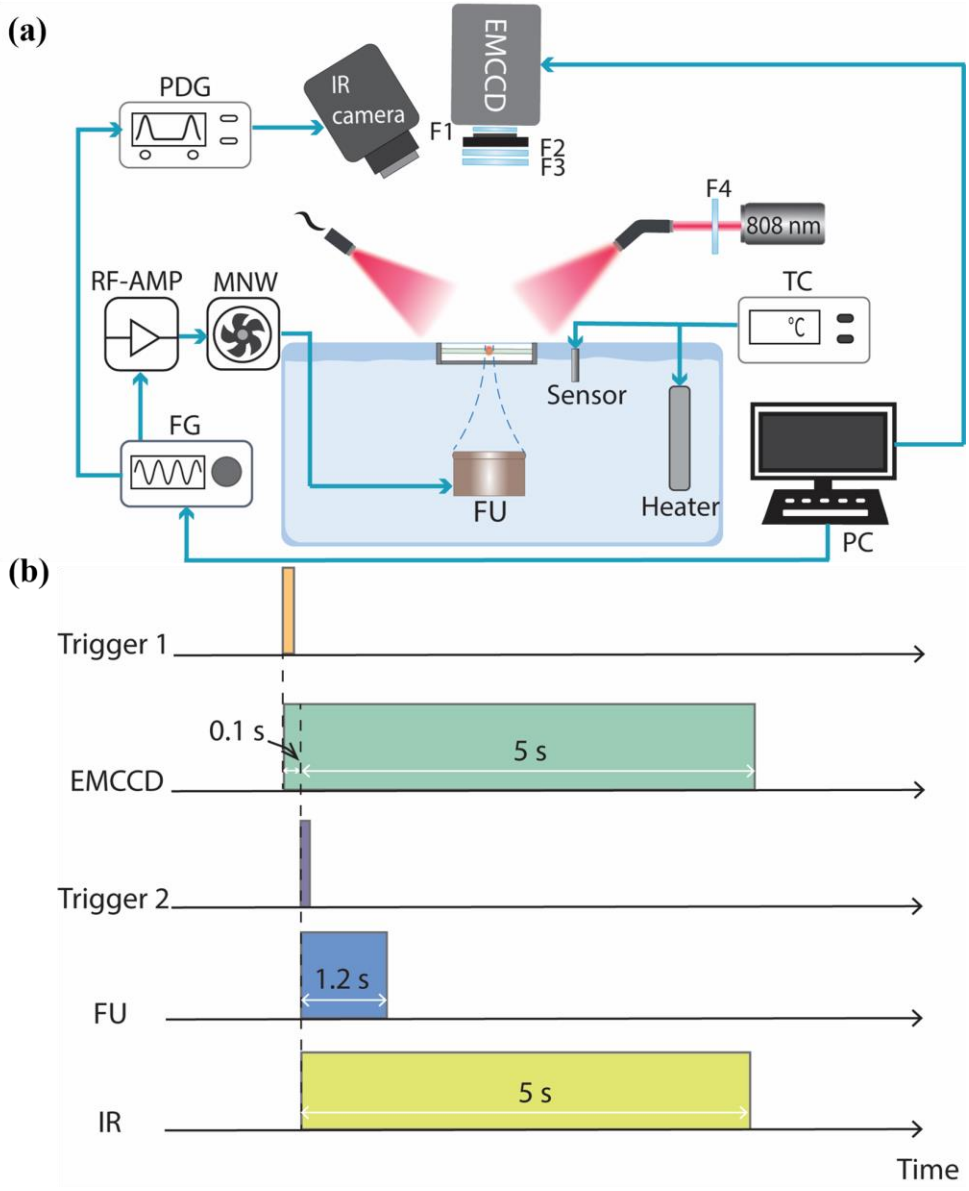

Figure 14 (a) Schematic diagram of the USF thermometry. PDG: pulse delay generator; RF-Amp: radio-frequency power amplifier; MNW: matching network; FU: focused ultrasound; FG: function generator; F1-3: emission filters (830 Long-pass); F4: excitation filter (785/62 Band-pass); TC: temperature controller. (b) Time sequence diagram of each temperature measurement.

The purposes of using a relatively thin silicone sample in this feasibility study are mainly due to two reasons: (1) Combining the small thickness with the transparency of silicone to IR light, the IR-camera-measured

temperature from the sample surface should be approximately equal to the temperature in the sample; (2) To enable the acquisition of dynamic signals at a high frame rate using the EMCCD camera, a strong USF signal without significant attenuation is required.

Figure 14(b) explains the time sequences and synchronization between USF imaging system and IR thermal camera. For all experiments, the heating FU pulse with a duration of 1.2 s was triggered 0.1 s after the EMCCD camera started acquiring. EMCCD camera was initiated by the trigger command sent by the computer (Trigger 1), while the FU transducer was externally triggered by the function generator. Both the function generator and EMCCD were synchronized by executing the customized MATLAB script on the computer. The frame rate of the EMCCD camera was 100 Hz. The IR reading was performed synchronously with the camera acquisition after FU exposure, and a single IR thermograph was obtained right before the FU heating to evaluate the background temperature at the target zone. The 10 frames obtained from the EMCCD camera before the FU exposure were averaged and considered as the background fluorescence image. The time point when the FU initiated and the rising edge of Trigger 2 occurred can be denoted as t_0. A continuous set of 500 fluorescence frames was captured immediately (at t_0) to monitor the real-time change of fluorescence in the focal area.

3.2.5 Fluorescence signal processing

This section explains the procedures for acquiring and processing the signals and further estimating the local temperature based on the acquired dynamic USF signal. The main procedures include measuring the fluorescence-vs-temperature based on two characteristic profiles of the two liposomes and their mixture in cuvettes, and the dynamic USF signals in tissue phantoms from the mixture of the two liposomes. After these profiles are acquired, their differential profiles (i.e., the first-order derivative profiles) are calculated by subtracting any two adjacent data points. The local peaks of these differential profiles are found and used as the characteristic parameters for background temperature estimation via the principle mentioned above (See Section 3.2.1).

First, the fluorescence emission signals from each of the two liposome samples and their mixture were measured as a function of temperature in a range from 34 to 54 °C with a step size of 0.1 °C using the in-house built spectrometer system. Thus, three switching curves were acquired and the first-order derivatives of each curve were calculated. A total of four local peaks were found from the differential profiles (one from each sample and two from the mixed sample). The dynamic USF signal of the mixed contrast agents was acquired from our camera-based USF

system. Briefly, a continuous series of fluorescence images were acquired before, during, and after the FU exposure. The images acquired before the exposure were subtracted from those acquired during and after the exposure. The subtracted images represented the USF signals at different time points. These subtracted images were subsequently and spatially filtered based on the correlation between a normalized averaging filter. Then, the USF intensity values of each USF image were averaged within a 0.33×0.66 mm^2 region of interest from the center of the heating spot, where the temperature distribution was relatively uniform. The computation of the temporal variation of USF intensity can be achieved following the steps mentioned above.

The differential profile of the dynamic USF signal from the mixed liposomes was computed similarly by subtracting any two adjacent data points of the USF signal, and then normalized. Two switching peaks can be found in the time domain, corresponding to two fast-switching temperatures revealed by the characteristic curves of the sample curves measured from the cuvettes. As a result, the information in both time and temperature domains corresponding to each switching peak can be found. As mentioned above, if the thermal diffusion in the focal volume can be ignored within such a short FU exposure, the local background temperature of the sample can be calculated based on the methods discussed previously in Section 3.2.1.

3.3 Results and discussion

3.2.1 Characterizations of fluorescence-vs-temperature profiles of the ICG-Liposomes in cuvettes

Figure 15(a) shows the temperature-dependent fluorescence profiles of the liposomes and their differential profiles. The red dashed line with circles for the liposomes with a high LCST (43.8 °C) and the green dashed line with triangles shows the profiles of the liposomes with a low LCST (38.9 °C). Their differential profiles are represented by the corresponding solid lines, respectively.

(a)

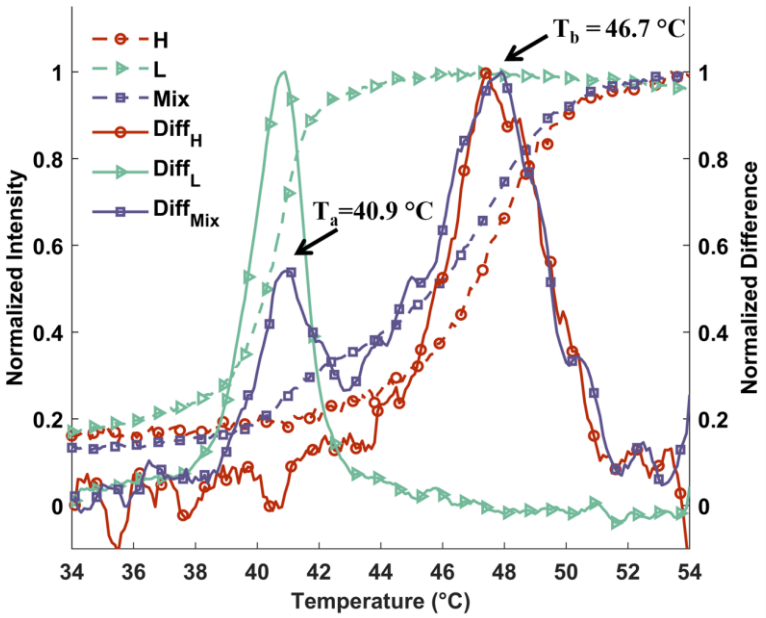

(b)

Sample	DPPC : DSPC	Size (nm)	PDI	Zeta potential	LCST (°C)	Transition band (°C)
H	0.6	368.86 ± 14.37	0.27 ± 0.09	-0.76 ± 0.61	43.8	6.8
L	1.5	414.94 ± 62.85	0.31 ± 0.07	-0.27 ± 0.94	38.9	3.1

Figure 15 (a) The normalized fluorescence intensity (solid lines) and the corresponding differences (dashed lines) as a function of temperature when testing the ICG-liposomes in the cuvette using a spectrometer. H: ICG-liposomes with a higher LCST; L: ICG-liposomes with a lower LCST; Mix: The mixtures of H and L with volume ratio of 4:1. Diff: the differences of fluorescence intensity of two adjacent points calculated from the corresponding solid line. (b) The characteristics of ICG-liposomes (H and L).

Clearly, the fluorescence-vs-temperature profiles exhibit a step function, which is a typical feature required in USF imaging [30], [84]. This fact indicates that the ICG-liposomes can be thermally switched on at different LCSTs over sharp transition bands. In addition, each differential profile shows a peak, representing the highest speed of the fluorescence rising at a specific temperature.

The ICG-liposomes had similar sizes, polydispersity index (PDI), and zeta potential as illustrated in Fig. 15(b). All liposomes had PDI values below 0.31, demonstrating the homogeneity of liposomes. ICG-liposomes with the high LCST (43.8 °C) are labeled with H and have an average size of 368.86 ± 14.37 nm with narrow size distribution (PDI= 0.27 ± 0.09) and neutral zeta potential at -0.76 ± 0.61 mV. The ICG-liposome with the low LCST

(38.9 °C) is denoted as L and has a size of 414.94 ± 62.85 nm with narrow size distribution (PDI= 0.31 ± 0.07) and neutral zeta potential at -0.27 ± 0.94 mV. The low LCST liposome shows a relatively narrower transition band (3.1 °C) relative to the high LCST liposomes (6.8 °C). The LCST shift from high (43.8 °C) to low (38.9 °C) is mainly caused by the increase in the mass ratio between the two main components of DPPC and DSPC from 0.6 to 1.5. The primary components of the liposomal shell are DSPC and DPPC, each possessing a distinct phase transition temperature of 55 °C and 41 °C, respectively [88]. Therefore, LCSTs of liposomal USF agents can be tuned effectively by varying the DPPC: DSPC ratio.

The fluorescence-vs-temperature profile of the mixed liposomes (with a volume ratio of H:L=4:1) and its differential profile are also plotted in Fig. 15(a) as the dashed purple line with squares and the solid purple line with squares, respectively. The switching property is preserved although the shape is changed compared with that of its individual component. Two peaks can be found from the differential profiles (40.9 and 46.7 °C), representing two local maximum speeds of the fluorescence rising and being related to the peaks of the individual components. These two temperature values (40.9 and 46.7 °C) will be used as T_a and T_b, respectively, and will be mapped to the USF dynamical signal for calculating background temperature.

3.2.2 Dynamic USF signal and its derivative of the mixed liposomes in a tissue phantom

As illustrated in Fig. 16(a), the dynamic USF signal and its derivative are displayed by the red dashed line with circles and the solid light green line, respectively. An inset of USF signals over 5 s is also shown in Fig. 16(a), and the USF signal was gradually decreasing after the FU exposure. The background temperature of the USF agents in Fig. 16(a) was 36.85 °C, which was below the first temperature peak (T_a=40.9 °C) as characterized in Fig. 15(a). The voltage from the function generator was 56 mV, which was amplified 50 dB by the power amplifier (RF-AMP) before being applied to the ultrasound transducer. The transmitted electrical power was estimated to be 0.39 W. The lateral and axial sizes of acoustic intensity focus were 0.55 and 2.8 mm, respectively [89].

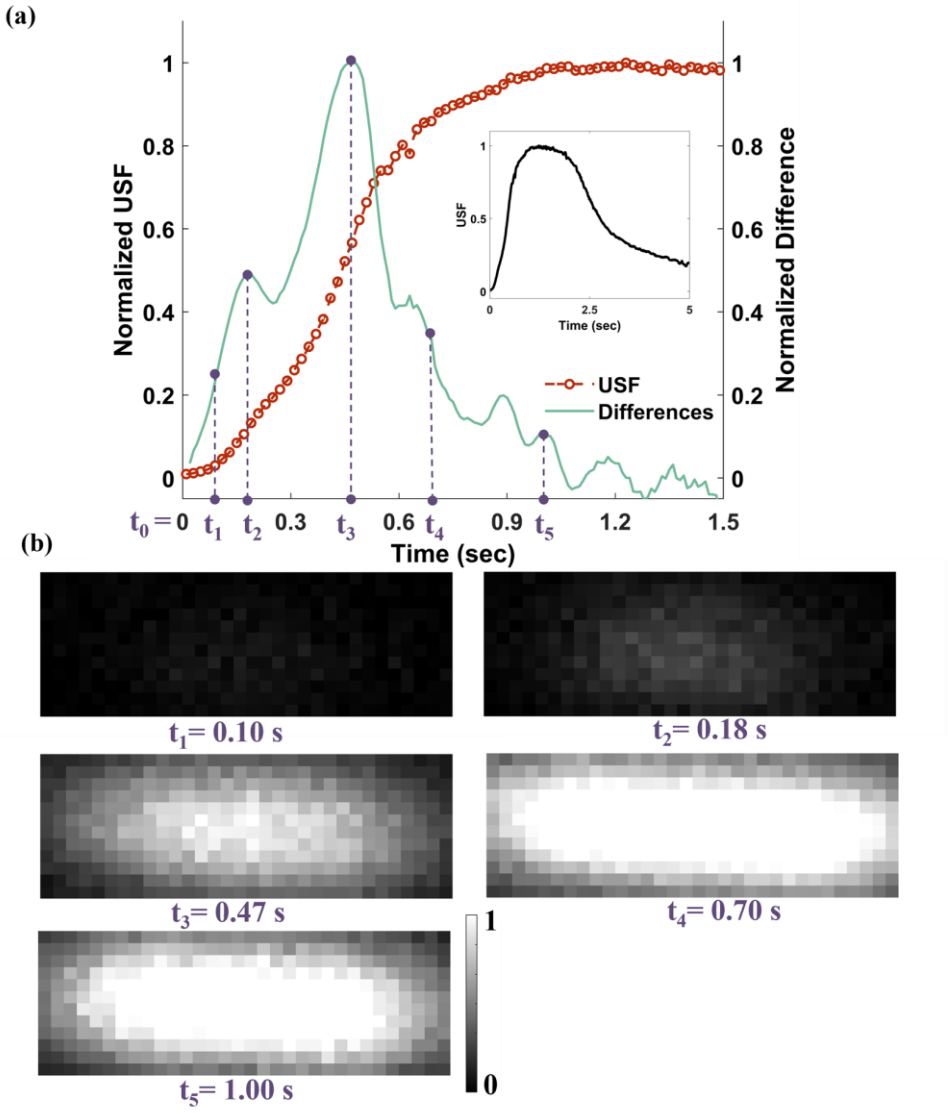

Figure 16 (a) A demonstration of temporal USF curve (red line) and the calculated differential curve (green line) obtained from the camera-based USF system. Inset: USF signals over 5 s. (b) The acquired USF signals with background subtracted (0.33 × 0.99 mm^2 view) at various time points ($t_{1\text{-}5}$).

To demonstrate the USF raw data, five 2D fluorescence images acquired at the time points from t_1=0.10 s to t_5=1.00 s by the EMCCD camera during the procedure are also displayed in Fig. 16(b). The USF signal increases over time immediately after the starting of the FU exposure at t_0=0 s and reaches the maximum when the FU exposure stops at 1.2 s. Similar results can also be seen from the 2D fluorescence images. Also, the first and second

peaks of the differential curve of the USF signal appear at t_2=0.18 s and t_3=0.47 s, which correspond to the ta and tb as discussed before. Obviously, the USF signal does not show a linear relationship with time. This can be seen from its differential curve, which is not a constant. In the early period of the FU exposure (such as $t<t_3$=0.47 s), the speed of USF signal remains in a rising period. After that, the speed falls gradually. This non-linear relationship is caused by two factors. First, in the rising period from 0 to t_3, the thermal energy is usually confined in the focal volume (i.e., so-called thermal confinement) so that thermal diffusion can be ignored, and the temperature grows linearly within the FU exposure time (i.e. the heating speed usually remains a constant in this period). Thus, the non-linearity of the USF signal is mainly caused by the nonlinear features of the step function of the fluorescence-vs-temperature of the two liposomes, rather than the heating. In the late period (such as after t_3), the thermal diffusion may not be ignorable. Thus, the non-linearity of the USF signal is caused by both the nonlinear thermal response of the liposomes and the thermal diffusion. Therefore, restricting ta and tb to the early rising period of USF signal or remaining a short ultrasound exposure is necessary to satisfy the thermal requirement and enable the assumption of a constant ultrasound heating speed in this study. In the situation when thermal confinement is not satisfied, more accurate models should be adopted for the background temperature estimation, which will be studied in the future.

3.2.3 Temperature estimation and precision

Figure 17(a) displays the estimated background temperature (T_t) from our USF method vs. the one measured from the IR camera. The background temperature of the liposome mixture was controlled and varied from 35.27 to 39.31 °C based on the IR camera reading. A solid line is also plotted as a reference to indicate the ideal situation. In general, the USF-estimated background temperature data points should be closely aligned with the reference line, indicating a high degree of correlation between the variables being compared (IR readings in this case). Quantitatively, based on all these data points in Fig. 17(a), the average temperature difference between the two methods was 0.64 ± 0.43 °C. In this study, the measurements were limited to a small range (from 35.27 to 39.31 °C) to match the typical physiological temperature. The measurement range can be modulated by the composition of the lipid shells. For instance, DSPC, DPPC, and dimyristoyl phosphatidylcholine (DMPC) are fully saturated lipids with different lengths of hydrocarbon chains. DMPC exhibits a phase transition temperature that is below body temperature at 24 °C, while the other two phospholipids can transit around and above the physiological temperatures [90].

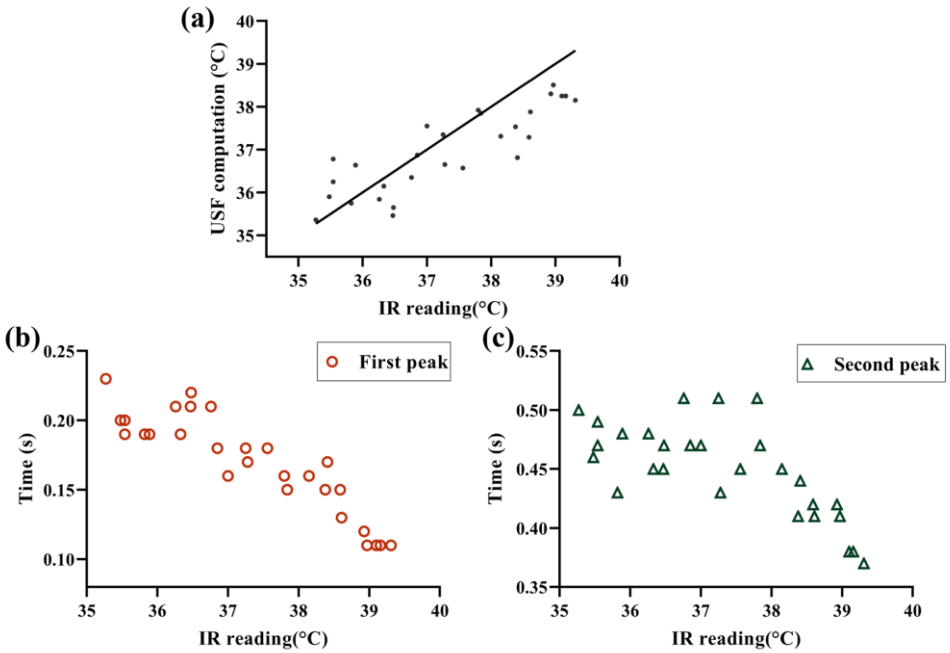

Figure 17 (a) The temperature estimated by USF thermometry versus IR camera. A reference line with a slope of 1 is added to show the agreements between IR reading and the results from USF thermometry. (b) The occurrence time of the first fast-switching peak at various background temperatures. (c) The time at which the second switching peak occurs at different background temperatures.

Figures 17(b)-(c) display how the two peak times (t_a and t_b) shift with the increase of the background temperature. When the background temperature increases, both t_a and t_b decrease, which means the two peaks occur earlier. These results are understandable based on the discussion below. Because T_a and T_b of the liposomes are mainly dependent upon the properties of the material component of the liposomes, it is reasonable to assume they are stable during our experiments. Increasing the background temperature (T_t) will lead to the reduction of the temperature difference between the background temperature and the T_a (and also T_b). In this experiment, the FU heating speed is considered to be fixed. Thus, the required duration for raising the temperature of the sample from T_t to T_a or T_b decreases. On the other hand, if subtracting the data in Fig. 17 (b) from the data in Fig. 17 (c), one can obtain the time difference, t_b-t_a, which represents the time that is needed for heating the sample from T_b to T_a. The results show that this difference remained relatively constant at approximately 0.28 ± 0.03 s. This further indicates

that the FU heating speed roughly remained a constant (i.e., $V_h=(T_b-T_a)/(t_b-t_a)=(46.7-40.9)$ °C/0.28 s=~20.71 °C/s) during this experiment.

3.2.4 Effects of other experimental parameters

Figure 18(a) shows one example of how the ultrasound strength (therefore the heating speed) affects t_a and t_b when the background temperature was kept at 37.00 °C. When the driving voltage from the function generator was increased from 54 to 59 mV, the ultrasound power was raised from 0.36 to 0.43 W. Thus, the heating speed was linearly increased from 14.87 to 17.06 °C/s because it is positively related to the ultrasound intensity. Therefore, both t_a and t_b are expected to be shortened due to the heating speed increase. This is validated by the result in Fig. 18(a) in which t_a is shortened 0.10 s and tb 0.15 s, respectively. A similar experiment was repeated when the background temperature was increased from 37.00 to 38.38 °C, and the results were displayed in Fig. 18(b) where t_a is shortened 0.03 s and t_b 0.02 s, respectively. These results in Fig. 18 indicate that the effect of the heating speed (i.e. ultrasound intensity) on t_a and t_b is more significant at lower background temperatures (relative to the T_a or T_b). This is understandable via one extreme example below. Imagining the background temperature is equal to T_a, ideally one can always have t_a=0 s no matter how fast the heating speed is. Thus, increasing the heating speed will not be able to shorten t_a. However, this assumption does not hold when the background temperature is lower than T_a as seen in Fig. 18(a-b).

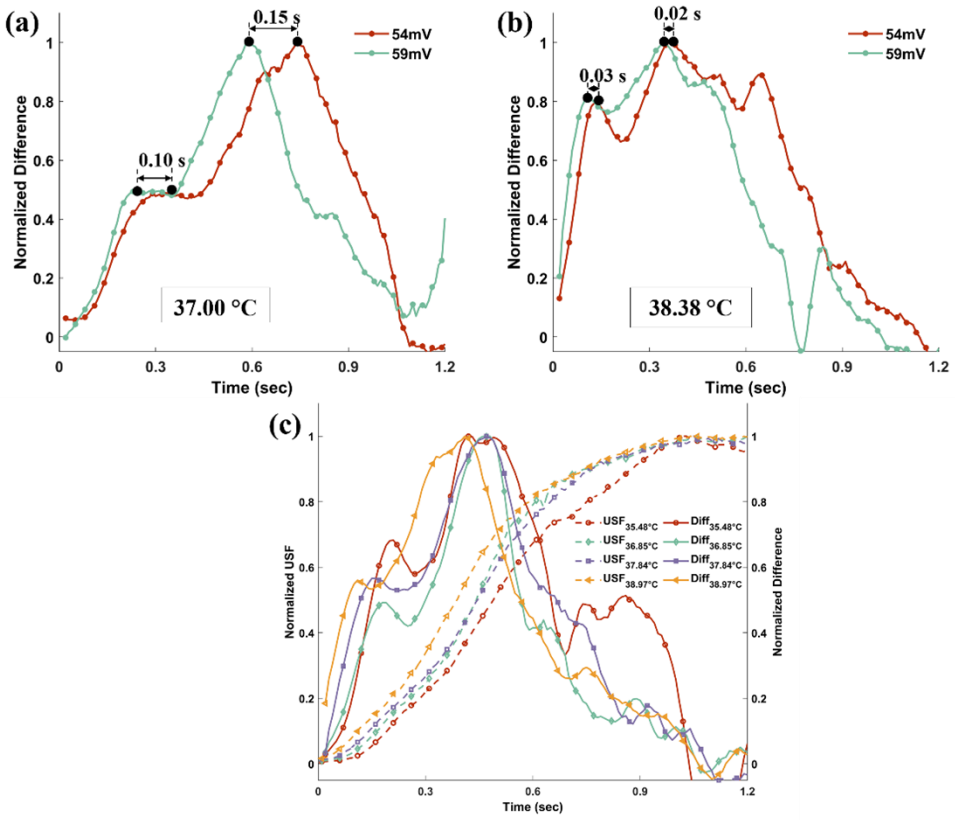

Figure 18 (a) The temporal profiles of normalized differences of USF signal when switching the thermosensitive USF agents by different ultrasound parameters (54 vs. 59 mV). The background temperature is 37.00 °C. (b) Similar results were obtained when the background temperature was 38.38 °C. (c) The normalized USF signals and signal differences with time at selected background temperatures (35.48, 36.85, 37.84, and 38.97 °C). Diff: the differences of two adjacent points in the corresponding dashed line.

The dynamic USF signals and their differential curves acquired at different background temperature values (35.48, 36.85, 37.84, and 38.97 °C) are also plotted in Fig. 18(c). The USF signals are represented using dashed lines, while their differential results are presented using solid lines. When the background temperature is consistent, these signals are depicted using the same color and marker. The differential USF curves indicate that the switching peaks occur earlier as the background temperature increases, owing to the relatively constant heating speed, which leads to faster attainment of T_a and T_b. This is also the reason why the corresponding USF signals display higher slopes, particularly at the start of the FU heating. The FDA guidelines emphasize the importance of well-defined

thermal effects and minimal side effects on surrounding tissues induced by FU. According to the thermal dose formulation, a thermal lesion along with thermal necrosis and the denaturing of tissue protein can form in 10 s at 53 °C [91]. Our experiments demonstrated that exposing tissue to ultrasound for 1.2 seconds raises the temperature from 36.80 to 52.98 °C, indicating a relatively low thermal damage. The mechanical index of FU used for USF thermometry is approximately 1.45, below the FDA limit for diagnostic ultrasound application at 1.9 [92]. Nevertheless, the exposure time can be further reduced to minimize thermal damage and allow for higher ultrasonic power on the condition that the second switching temperature (T_b) can be achieved. Additionally, future *ex*/*in vivo* studies using biological tissue which has a lower absorption coefficient than silicone tube in this feasibility study may allow higher ultrasonic voltage to be applied [36].

3.2.5 Limitations and advantages

The destabilization of the liposome membrane can occur due to hydrolysis and oxidation of lipids, resulting in the formation of soluble derivatives. Physical interactions such as aggregation and coalescence of liposomes can also lead to the loss of encapsulated molecules and changes in size. 30% of cholesterol is considered to be the most stable formulation according to the literature [93], but only approximately 10% molar ratio of cholesterol was added as stabilizer in the current protocol. This is because the transition bands of ICG-liposomes become wider as more cholesterol was added, which can negatively affect the sensitivity of agents at the switching temperature. Therefore, there are still concerns regarding the stability of ICG-liposomes at body temperature, which compromises the effective use of liposomes in the USF-based thermometry. It is also not clear if the instability of USF agents will shift the transition temperature, which may undermine the consistency and repeatability of the experiment data, and lead to fluctuations in temperature measurements.

The temperature estimation is only based on the information collected from two switching peaks, and therefore more switching temperature points possibly allow for higher accuracy and a broader estimation range. However, it will increase the complexity if more switching peaks are incorporated by adding extra varieties of ICG-liposomes with different threshold temperatures.

In addition, the linear heating assumption and the linear equation to calculate the heating speed may be replaced by more sophisticated models, such as thermal diffusion and photon diffusion to improve the accuracy.

While the background temperature estimation has only been demonstrated at a single point, the capability of USF thermometry to map two-dimensional temperature distribution by scanning is a non-negligible advantage. Imaging temperature at depths can be another potential of USF thermometry. A sub-millimeter tube in a 5.5 cm thick chicken breast tissue was successfully imaged using the same USF imaging system and similar ICG-liposomes agents, proving that the spatial imaging resolution remains relatively consistent at varying depths [41]. Therefore, the combination of temperature measurements and USF imaging at deep tissues in the same experiment holds another great potential. However, it is crucial to carefully select the appropriate exposure time and FU intensity for different samples and imaging depths to achieve accurate and reliable results. Further efforts to maintain an acceptable signal-to-noise ratio in the future *ex*/*in vivo* studies of this USF-based thermometry at a deeper level will be investigated.

3.4 Conclusion

This study shows that the local background temperature can be estimated by analyzing the temperature-dependent fluorescence variations from USF contrast agents during ultrasound heating. The ICG-liposome agents provide a tunable measurement range that can be adjusted by modifying the compositions of the outer lipid shells. This USF-thermometry with the mixture of ICG-liposomes with two distinct temperature switching-on thresholds was tested and the dynamic USF signals using a camera-based USF system were also recorded. By fitting the results into our customized algorithm, the local background temperature of the sample can be calculated over a typical physiological range. Our findings indicate that this USF technique-based temperature measurement provides accurate temperature readings, validated by an independent measurement from IR thermography, with a difference of only 0.64 ± 0.43 °C between the two techniques over a range of 35.27 to 39.31 °C.

The significant implications of this research lie in the potential for the USF-based thermometry technique to be applied to deep tissue temperature imaging applications. This approach provides an alternative method to current techniques, which are limited by the low sensitivity and inability to measure temperatures at depth. Further research can optimize USF contrast agents and advance the USF-based thermometry technique to enable its translation into in *vivo* and clinical settings. In summary, our study highlights the potential of USF-based thermometry as a valuable tool for future research and clinical practice, and this new temperature imaging method with a tunable measurement range makes it a great approach for a wide range of applications.

Chapter 4 EXPERIMENTAL STUDIES ON SQUEEZING INTERSTITIAL FLUID VIA TRANSFER OF ULTRASOUND MOMENTUM (SIF-TUM) IN EX VIVO TISSUES

4.1 Introduction

Nanotechnology has been extensively explored for cancer diagnosis and treatments in the past decades [94]. However, the drug delivery efficiency is still not satisfactory, and only 0.7% of administered nanoparticles actually entered solid tumors based on the studies published from 2005 to 2015 [95]. The clearance from the bloodstream by the immune, reticuloendothelial, and renal systems, limited diffusion in dense extracellular matrix, and elevated interstitial pressure gradients pose a significant challenge to effective agent delivery via nanoparticles [48], [96].

Ultrasound-assisted drug delivery has been shown to enhance the mobility of therapeutic or diagnostic agents within diseased tissues and increase permeation across the blood-brain barrier [97], [98]. Several mechanisms of ultrasound-enhanced drug delivery have been proposed, including mechanical effects (such as sonoporation, cavitation, microstreaming, and agent-enhanced effects via microbubbles or pressure-sensitive proteins) and thermal effects (hyperthermia, diffusion, and thermophoresis) [33], [99]–[102]. However, it is still challenging to fully understand the reasons for each specific application, especially in deep tissues. Recently, a new macroscopic streaming mechanism, named squeezing interstitial fluid via transfer of ultrasound momentum (SIF-TUM), was proposed and modeled by our lab to explain possible ultrasound-driven nanoparticle motion enhancement in deep tissues [35]. Briefly, a tissue is considered a two-phase material, including both interstitial fluid (movable) and solid matrix (deformable). When an ultrasound beam is tightly focused into the tissues, it can pass its momentum to tissue interstitial fluid and push the fluid flowing out of the ultrasound focal volume from all directions. This generates a macroscopic streaming of the interstitial fluid (away from the focal volume). At the same time, this results in the inward compression of the solid tissue matrix around the focal volume if no void space can exist in the tissues. After the ultrasound exposure, the solid matrix undergoes recovery (i.e., expanding back to the original position), and therefore the interstitial fluid must flow back into the ultrasound focal volume, which can bring the nanoparticles back too. In addition, the thermal effects, such as thermophoresis via temperature gradient and diffusion via concentration gradient, on the particle motion were found much weaker than the streaming caused by SIF-TUM [35].

To demonstrate the SIF-TUM effect, several experiments were designed in this work to investigate how this macroscopic streaming effect drives nanoparticle motion in tissues and how these nanoparticles recover after ultrasound exposure. As claimed in the previous study [35], streaming occurring at the tissue-and-water-bath boundary (used in the literature) may not fully reflect the dynamics of SIF-TUM and may not simulate real applications in deep tissues. In this study, streaming inside tissues was investigated by focusing an ultrasound beam 2-3 mm away from the top boundary between the tissue and air interface. In addition, to avoid the confounding between mechanical and thermal effects, a temperature-insensitive fluorophore, sulforhodamine 101 (SR101) was encapsulated into a temperature-insensitive nanoparticle, made of poly(lactic-co-glycolic acid) (PLGA). This nanoparticle was denoted as SR101-PLGA. Using the same system as our USF imaging [41], [84], [103], the dynamics of the ultrasound-induced motions of the nanoparticle (SR101-PLGA) in both chicken breast and porcine loin muscle tissues were studied after locally injecting SR101-PLGA in *ex vivo* animal tissues. The ultrasound-caused fluorescence reductions and recoveries were noticed within the ultrasonic focal area in two types of tissues and showed good consistency with our theoretical studies [35]. The dynamic fluorescence changes are tissue-dependent, with a faster recovery in porcine than in chicken tissues. These results not only experimentally demonstrate the SIF-TUM mechanisms but also may benefit the researchers who are looking for an accelerated and controlled distribution of nano agents with the aid of ultrasound.

4.2 Methods

4.2.1 Materials and synthesis of nanoparticles

To select a temperature-insensitive fluorophore, the following four dyes were tested. Fluorescein 548 (FL548; peak excitation: 498 nm; peak emission: 517 nm) was purchased from Exciton, Inc (Lockbourne, OH). SR101 sodium salt (peak excitation: 586 nm; peak emission: 606 nm) was purchased from Assay Biotech (Fremont, CA). Cyanine 5 (CY5 NHS ester; peak excitation: 646 nm; peak emission: 662 nm) was from Broadpharm Inc (San Diego, CA). ICG (peak excitation: 789 nm; peak emission: 814 nm) was purchased from Chem-Impex Int'L Inc., USA. Temperature-insensitive polymer, PLGA, LG (lactic/glycolic=50:50, Mn 15,000-25,000 Da) was purchased from AKina Inc (West Lafayette, IN). Polyvinyl alcohol (PVA, 15,000–25,000) was purchased from Sigma-Aldrich (St. Louis, MS).

Nanoparticles were synthesized using the standard emulsion method as previously described [104]–[106]. Briefly, SR101 was dissolved in 100µL methanol and was added dropwise to 3 mL of organic solution of chloroform containing 100 mg PLGA. The solution was later added dropwise to 20 mL of the aqueous phase of 5% w/v PVA. The emulsion was probe-sonicated at 25 W for 1 minute on ice. The nanoparticle suspension was stirred at 700 rpm and evaporated overnight at room temperature to remove organic solvent. The nanoparticles were collected by ultracentrifugation at 17,000 rpm for 20 minutes at 4 °C. The nanoparticles were then lyophilized and stored at -20 ºC after washed. The freeze-dried sample was resuspended in deionized water followed by shaking and vortexing until there was no solid component in the solution for experimental use.

4.2.2 Characterization of fluorophores

The fluorescence vs. temperature profiles of various dyes and SR101-PLGA were obtained using a temperature-controlled spectrometer-based system [41]. The fluorescence level at each temperature was represented by the sum of fluorescence counts in their corresponding emission spectra.

4.2.3 H&E staining and image acquisition

Porcine and chicken tissues were embedded in optimal cutting temperature (OCT) compound, and flash frozen using liquid nitrogen. Frozen tissues were cross-sectioned at 7 µm thickness using a cryostat (Leica CM1860 UV, (Leica Biosystems, Nussloch, Germany) at -20 °C. The sections were hematoxylin and eosin (H&E)-stained and mounted using permount (SP15-500, Fisher, Fair Lawn, NJ) then imaged under a bright field microscope (RV2-K, Echo, San Diego, CA).

4.2.4 USF imaging system: ex vivo tissues model

The setup of the USF imaging system has been reported previously and the schematic diagram is shown in Fig. 19 [84], [103]. A 2.5 MHz FU transducer (focal length: 50.8 mm; H-108, Sonic Concepts Inc, USA) was used to emit focused ultrasound waves. The sample was placed in a small tank half-submerged in a big water tank. The fluorescence from the sample passed through three emission filters (BLP01-830R50/25, Semrock Inc., USA) and was captured with an electron multiplying charge-coupled device (EMCCD, ProEM®-HS: 1024BX3, Princeton Instruments, USA) equipped with a lens (AF NIKKOR 50 mm f/1.8D Lens, Nikon, Japan). A 473 nm laser (MBL-III-473-20mW, Dragon Lasers, China) with an intensity of 700 μWcm^{-2} was used as an excitation source.

The frame rate of the EMCCD was 25 Hz, and the EM gain was set to 3. Frames were captured continuously to acquire the temporal profile of fluorescence distribution in the focal area. The first 5 frames obtained from the camera before the FU exposure were averaged and used as the background fluorescence image. Each 2D frame obtained after the initiation of FU exposure was processed by subtracting the image from the corresponding pixel values in the background fluorescence image. The fluorescence level of each frame was then represented by the average of pixel values in the target area (0.7 x 1.0 mm^2), which is slightly larger than the focal area of FU because the displacements of agents are considered to be accumulative and becoming larger with time. The experiment was conducted with different ultrasound parameters, and each condition was repeated three times, with the curve plotted as the average at each time point.

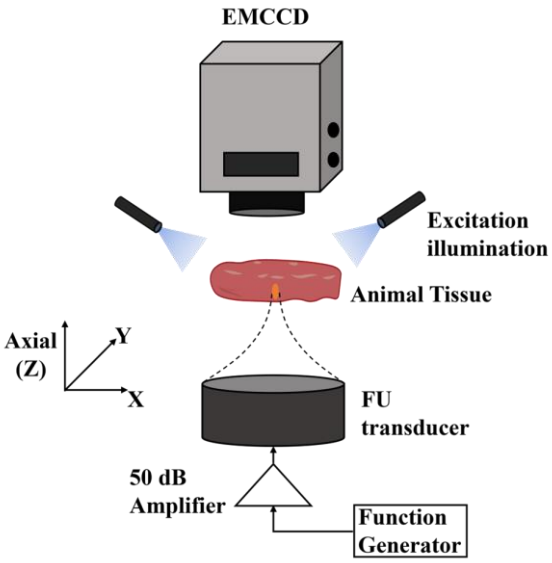

Figure 19 The experimental setup. The sample was exposed to a 2.5 MHz FU transducer, and the fluorescence was acquired by an EMCCD camera.

4.2.5 Samples

150μL PLGA-SR101 suspension (35 mg/mL) was injected into the tissue samples (chicken breast and porcine loin tissues purchased from local grocery stores) with a thickness of 13 mm via a 31-gauge needle. To avoid possible leakage from the hole created by the needle, instead of from the top surface where the camera field view is located, the nanoparticle solution was injected slowly from one side of the sample (i.e., horizontally injecting the

particle solution). The needle tip is ~2-3 mm away from the top surface. On the other hand, to minimize the boundary effect, the ultrasound beam was focused inside the sample 2-3 mm away from the tissue-and-air boundary).

4.2.6 Data fitting models

The results of the fluorescence reductions during ultrasonic exposures were fitted with a linear fitting model. The recovery segments were fitted using three different models including single-phase exponential regression, two-phase exponential regression, and a customized model. Curve fitting was conducted in GraphPad Prism (GraphPad Software Inc., San Diego, CA, USA) or using the curve-fitting toolbox in Matlab (The Mathworks, Natick, Massachusetts, USA). Data was smoothed with a gaussian-weighted moving average filter (sliding window =280 ms) before fitting with the custom *M* model.

In the single-phase exponential model, the fluorescence dynamics (S_t) can be expressed by the following equation:

$$S_t = (S_0 - Plateau)e^{-\frac{t}{\tau_r}} + Plateau$$

The double exponential model can be presented by:

$$S_t = (S_0 - Plateau)(Fast\%)e^{-\frac{t}{\tau_{fast}}} + (S_0 - Plateau)(1 - (Fast\%))e^{-\frac{t}{\tau_{slow}}} + Plateau$$

Where S_0 is the initial fluorescence level when time is zero. $Plateau$ is the fluorescence level at infinite times. Fast% is the fraction of faster exponential component in the equation. τ_r, τ_{fast}, and τ_{slow} are exponential time constants.

The SIF-TUM models provided in the previous publication [35] usually need to be numerically solved by assuming several parameters. To avoid the complexity and the assumption of unknown parameters, in this study, the models are significantly simplified by boldly only considering the central location of the ultrasound focal volume. Thus, a similar analytical solution provided in the literature (usually for calculating ultrasound-induced temperature in tissue) can be adopted to derive an approximate solution for describing the fluorescence reduction [107], [108].

Briefly, the normalized USF signal at the central location of the ultrasound focal volume (i.e, $r = 0$) is approximately expressed as the following analytical solution in the custom M model (derived by Dr. Yuan):

$$\frac{S_{\mathrm{USF}}|_{r=0,t>t_0}}{|S_{\mathrm{USF}}|_{r=0,t=t_0}|} \propto \frac{-{\beta_z}^{1/2}\beta_r}{\left[(4M(t-t_0)+\beta_r)*(4M(t-t_0)+\beta_z)^{\frac{1}{2}}\right]}$$

which can be used as the fitting model to extract M. Here, t_0 is the time when ultrasound exposure ends; M is a "diffusion-like" parameter that has a unit of meter^2/second and represents the transportability of nanoagent in tissues at a macroscopic level [35]; t is time; $\beta_r = 2\sigma_L^2$ and $\beta_z = 2\sigma_A^2$ are related to the square of the lateral and axial focal size of the ultrasound beam, respectively. σ_L can be calculated by dividing the lateral FWHM of the focal zone by a constant of 2.35 and similarly, σ_A can be calculated by dividing the axial FWHM of the focal zone by the same constant (note that the lateral and axial FWHMs of 0.55 and 3.5 mm were used in the fitting). It is important to know that this solution is an approximated analytical solution. The disadvantage is that this model is not an accurate solution to represent the fluorescence recovery dynamics. The advantage is that it is very simple, and the data can be quickly fitted to extract the value of M. More importantly, M is the only unknown parameter. Also, M has a clear physical meaning, representing the nanoparticle transportability [35]. Note that M can be accurately defined and derived from the SIF-TUM models by inserting the equations (1) and (2) into (4) in our previous paper [35], and can be expressed as $M = R_f\,(k/\mu)H$, in which (a) tissue permeability k (related to tissue porosity), (b) tissue fluid viscosity μ, (c) the retardation factor R_f between interstitial fluid and the agent (related to the size difference between tissue pores and nanoagent, and also the surface charge effect between the agent and the adopted tissue), and (d) tissue apparent modulus H (related to tissue elasticity). It is impossible to estimate M based on these unknown and unmeasurable individual factors. Fortunately, M can be experimentally measured via the experimental fitting methods.

4.3 Results and discussion

4.2.1 Comparison of fluorophores

Figure 20 shows that the fluorescence of various dyes and SR101-PLGA changes with respect to temperature. Fluorescein 548 (FL548) exhibits increased fluorescence over a range of 20 °C with a rate of 1.5% per °C. The fluorescence of cyanine 5 (CY5 NHS ester) and ICG decrease significantly with a rate of 0.6% per °C

when the temperature increases from 30 to 50 °C. SR101 grows 0.35% per °C, exhibiting good temperature stability over the temperature range from 30 to 50 °C when dissolved in deionized water. SR101-PLGA remains nearly temperature-insensitive and increases 0.91% per °C. Note that the motion of nanoparticles induced by SIF-TUM, causing them to move out of the ultrasound focal volume, results in a reduction of fluorescence within the ultrasound-illuminated region. At the same time, the temperature in the focal volume may slightly rise. To avoid the confounding associated with the thermal effect, it is better to select a dye that has a positive relationship between fluorescence strength and temperature (such as SR101 or FL548). Thus, the reduction in fluorescence will not be caused by thermal effect, which may not be certain for the dyes that have a negative correlation (such as CY5 or ICG). In this study, SR101 was selected, which not only shows a positive relationship but also is relatively less sensitive to temperature than FL548.

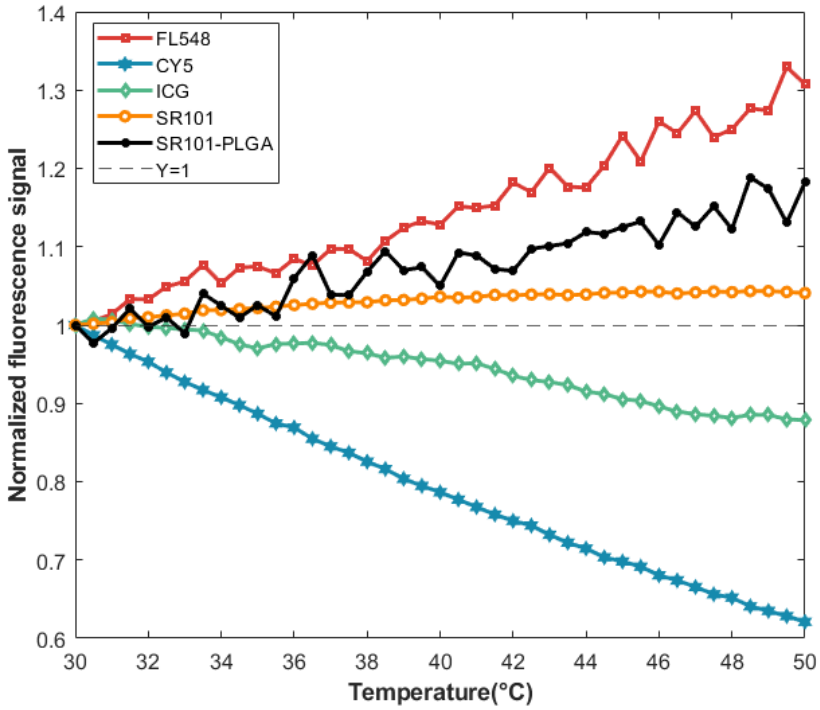

Figure 20 Temperature dependence of the fluorescence emission of FL548 (>561 nm), CY5 NHS ester (>715 nm), ICG (>830 nm), SR101 (>561 nm), and SR101-PLGA (>561 nm) when excited at 473, 640, 808, 473, and 473 nm, respectively.

4.2.2 Porcine versus chicken comparison

Figure 21(a) illustrates the temporal profile of the fluorescence in the ROI as indicated by the black box in Fig. 21(b) and (c). The fluorescence goes down, showing a similar decay trend in both porcine and chicken tissues when FU is on from 0 to 1.6 s (i.e., from t_0 to t_3), while fluorescence within the focal volume recovers due to the backflow of agents upon the deactivation of ultrasound. The backflow rate primarily relies on tissue properties (i.e., the parameter M discussed above, such as tissue permeability k, tissue fluid viscosity μ, the retardation factor R_f, and tissue apparent modulus H) [35]. M represents the capability of agents to flowback into the ultrasound focal volume after ultrasound squeezing via a "diffusion-like" behavior, rather than a concentration gradient. In addition to the parameter M, the recovery speed of the fluorescence signal can also be quantified by recovery time constants by fitting the experimental data to an exponential decay function (either a single or multi-exponential decay model), which will be discussed below.

Based on the data in Fig. 21, the recovery of fluorescence in porcine tissues is much faster than which in chicken breast tissues, and a higher initial backflow speed is observed. This may indicate a higher transportability (M), which may be due to higher tissue apparent modulus, a larger pore size in the porcine tissues and/or lower viscosity of interstitial fluid [35], [109].

Animal tissue is considered to be a biphasic mixture of solid matrix and liquid matrix, and the nanoparticles are believed to most likely exist in the interstitial fluid due to the administration via the local injection. The backflow rate primarily relies on tissue properties and becomes independent of the ultrasound parameters according to SIF-TUM. Remarkably, the initial backflow rate even surpasses the decay flow rate induced by the ultrasound, suggesting that the fluid containing the fluorescent nanoparticles comes backs to the ROI rapidly once the ultrasound illumination stops. However, it quickly diminishes to a small value due to the limited flow velocity of the backflow, which is typically observed in biphasic materials.

A ring-shaped pattern in Fig. 21(b) and (c) indicates the outward movements and accumulation of agents in the surrounding region after ultrasound termination. The agents are continuously displaced from the focal center during the ultrasound activation period and backflow immediately after the termination of ultrasound, leading to a recovery of fluorescence level. As nanoparticles are moving towards the surrounding areas of the ultrasound focus,

the surrounding fluorescence is expected to increase. However, this may not be visibly obvious in Fig. 21(b) and (c) due to the volume effects of surrounding tissues. Fig. 21(d1) and (d2) present the one-dimensional spatial fluorescence profiles along the horizontal and vertical axes at the moment when FU stopped (i.e., $t=t_3$). The vertical spread of the fluorescence patterns in chicken tissues exceeds that observed in pork, while their horizontal dimensions are similar. This discrepancy can likely be attributed to the distinct muscle arrangements in chicken and pork tissues, which, in turn, influence the pathway of ultrasound penetration.

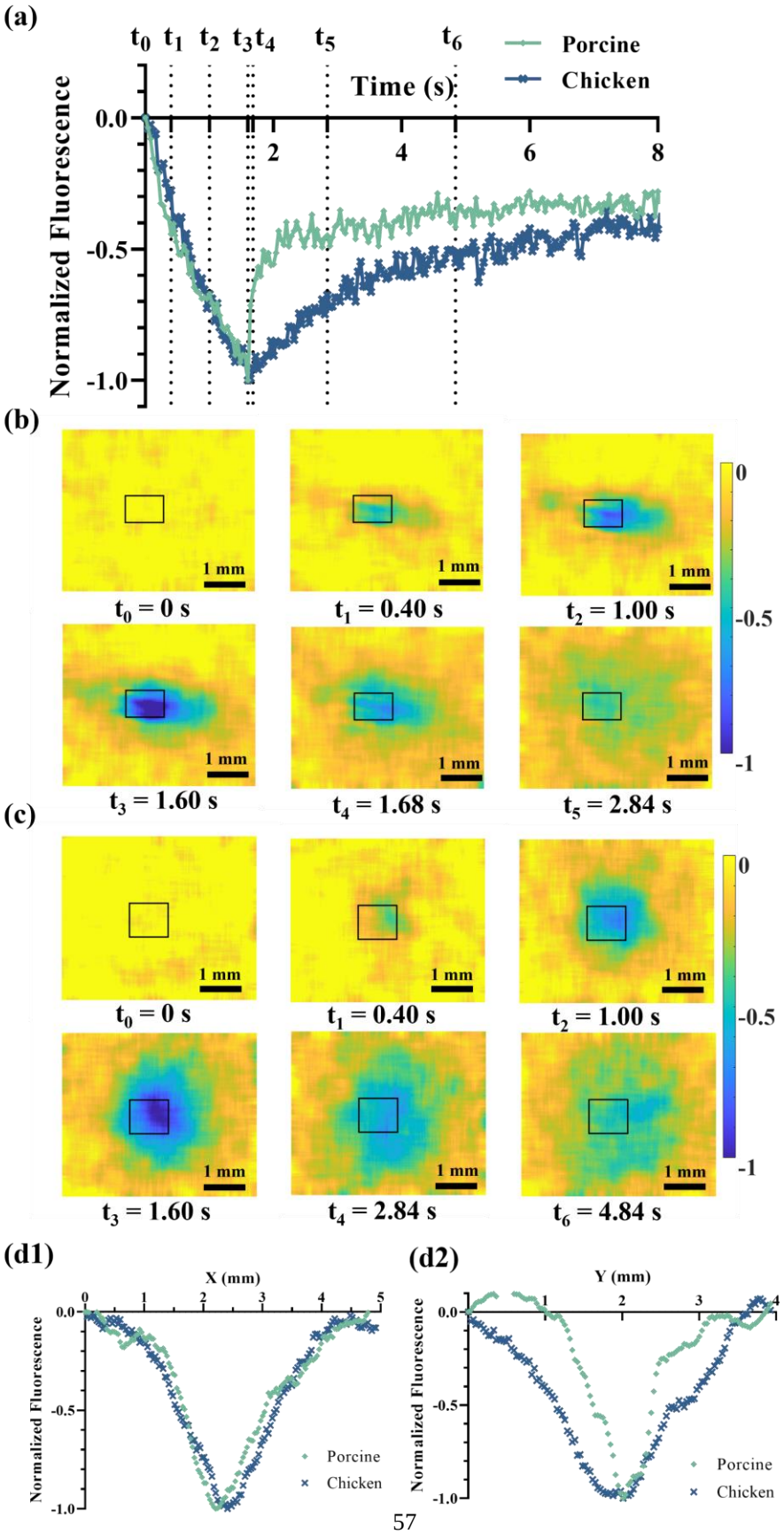
(a)
t0 t1 t2 t3 t4 t5 t6
Porcine
Chicken
Time (s)
Normalized Fluorescence
0.0
-0.5
-1.0
2
4
6
8
(b)
1 mm
t0 = 0 s
t1 = 0.40 s
t2 = 1.00 s
t3 = 1.60 s
t4 = 1.68 s
t5 = 2.84 s
0
-0.5
-1
(c)
1 mm
t0 = 0 s
t1 = 0.40 s
t2 = 1.00 s
t3 = 1.60 s
t4 = 2.84 s
t6 = 4.84 s
0
-0.5
-1
(d1)
X (mm)
Normalized Fluorescence
Porcine
Chicken
(d2)
Y (mm)
Normalized Fluorescence
Porcine
Chicken

Figure 21 (a) The fluorescence variations with time within the focal area in the animal tissues. The subtracted fluorescence images (5 x 4 mm^2 view) of (b) porcine tissues and (c) chicken breast tissues, were obtained during and after HIFU exposures. Images were normalized with a 15 x 15 matrix averaging spatial filter. Black box indicates the ROI for calculating the mean fluorescence. (d1-2) The spatial profiles (X: horizontal; Y: vertical) of fluorescence image at t_3.

The ultrasound-caused fluorescence decay and the subsequent fluorescence recovery due to the backflow processes were also investigated with different ultrasound strengths (controlled by the applied voltage) and exposure time in both pork and chicken breast tissues. Three trials were repeated in each experiment condition, and a curve was plotted as the average of three sets of results.

Fig. 22(a) shows the dynamics of the fluorescence reduction and recovery in the chicken breast tissues, respectively. Two voltages (125 and 145 mV) and three exposure times (0.8, 1.2, and 1.6 s) from the function generator were tested. One can find that the fluorescence reduction time is increased with the exposure time, which is understandable because the SIF-TUM effect is directly related to the exposure time. In addition, the extent of the fluorescence reduction is related to both the exposure strength and time. The longer the exposure time and the higher exposure strength can induce higher fluorescence reduction. Specifically, the fluorescence reductions of six groups were normalized in relation to the maximum reduction observed in the 145mV1600ms group (designated as 100%). The corresponding reductions for the other groups are as follows: 83.6% for the 145mV1200ms, 61.3% for the 125mV1600ms, 58.4% for the 145mV800ms, 51.2% for the 125mV1200ms, and 38.3% for the 125mV800ms. This result indicates that higher voltage (i.e., higher ultrasound strength) induces higher streaming velocity of the intestinal fluid to be “squeezed” out of the focal volume (i.e., more negative slopes in Fig. 22(a) for higher voltage). The results in Fig. 22(a) are consistent with the prediction from the SIF-TUM model [35]. Figs. 23(a1) and (a2) show the results in porcine tissues. Similarly, increasing the exposure time results in a longer fluorescence reduction period, which agrees with the results in Fig. 22(a). However, it does not increase the extent of fluorescence reduction. In addition, increasing the voltage (i.e., increasing the ultrasound strength) does not consistently lead to an increased fluorescence reduction. This phenomenon can be elucidated by considering the possibility of increased tissue fluid loss due to the porosity of the porcine muscle fiber structure, as visually depicted in Fig. 24, especially

when multiple experiments are conducted consecutively at the same location. The microstructure of pork exhibits greater porosity with larger intercellular gaps, whereas Fig. 24(b) reveals denser and tighter interconnections among chicken muscle cells.

Figure 22(b) shows the linear fitting of the fluorescence reduction in chicken breast tissues with a $R^2 \geq 0.95$. However, Fig. 23(b) presents that the performance of the linear model is slightly worse in porcine muscle tissues with the lowest R^2 at 0.91 for two groups (125mV800ms and 125mV1200ms). This decrease in R^2 can be attributed to the faster initial fluorescence reduction during the early stages of ultrasound stimulation. This phenomenon is likely due to the less resistance to the movement of nanoparticles in the more porous tissue structure of porcine samples, resulting in misalignment between the early data points and the linear fitting curves. The fitted time constants for the recovery periods are denoted τ_r, and listed in Table 1. The single-phase exponential model in porcine muscle tissues as illustrated in Fig. 23(c1) exhibits an excellent fitting performance with the coefficient of determination $R^2 \geq 0.95$. However, the R^2 is slightly less than 0.9 in the chicken breast tissues for two sets of data (at 125 mV with an exposure time of 0.8 and 1.2 s) as shown in Fig. 22(c1-1). The fitting performance of single-phase exponential functions with the recovery segments in chicken breast does not exhibit the same level of accuracy as observed in porcine tissues. This disparity in fitting quality can be attributed to the extended fitting time interval used for the chicken model (4 s) in comparison to that of porcine tissues (0.8 s), potentially introducing additional noisy data points from the plateau level. An extended temporal interval of 6 s in Fig. 22(c2-1), 4(c2-2), and 23(c2) was chosen to accommodate a two-phase exponential model. Therefore, two time constants that can be fitted for each recovery period are denoted as τ_{fast} (i.e., the smaller time constant) and τ_{slow} (i.e., the larger time constant), respectively. The results are listed in Table 1. This selection aimed to offer a more comprehensive insight into the slower exponential elements and to prevent data loss. It is worth noting that this approach, while potentially introducing fitting complexity, resulted in a marginal improvement in the R^2 when compared to the one-phase exponential model, even during prolonged fitting durations, for both tissue samples. When the applied voltage is relatively low or the ultrasonic exposure is short (e.g., 125mV or 800 ms), the calculated fluorescence vs. time profile is also nosier. This may explain why smaller R^2 values were noticed in 125mV800ms, 125mV1200ms, and 145mV800ms groups as shown in Fig. 23(c1-2).

Comparing the exponential fitting models, the fitting to the analytical solution for extracting the parameter M shows relatively lower R^2 (several groups provide R^2 between 0.83 and 0.9) as shown in Fig. 22(c3) and 23(c3), despite its inherent simplicity with only one parameter. This is understandable because the solution is an approximation (either a more accurate analytical solution or adopting a numerical solution with known other parameters should be developed in the future). While keeping this disadvantage in mind, M is 0.056 ± 0.011 (mm^2/s) in porcine tissues, significantly higher than M=0.0064 ± 0.0012 (mm^2/s) obtained with chicken breast. The fitted M shows not only a relatively stable value for different experimental conditions (~19%-20% variations, i.e., =0.011/0.056 and 0.0012/0.0064), but also shows significantly different values for the two types of tissues (~8.75 times, i.e., =0.056/0.0064). These results indicate that the nanoparticle has higher transportability in the porcine tissue sample than in the chicken breast tissue samples adopted in this study. Meanwhile, the effect of the experimental conditions on M is much less significant than the tissue types used in this study.

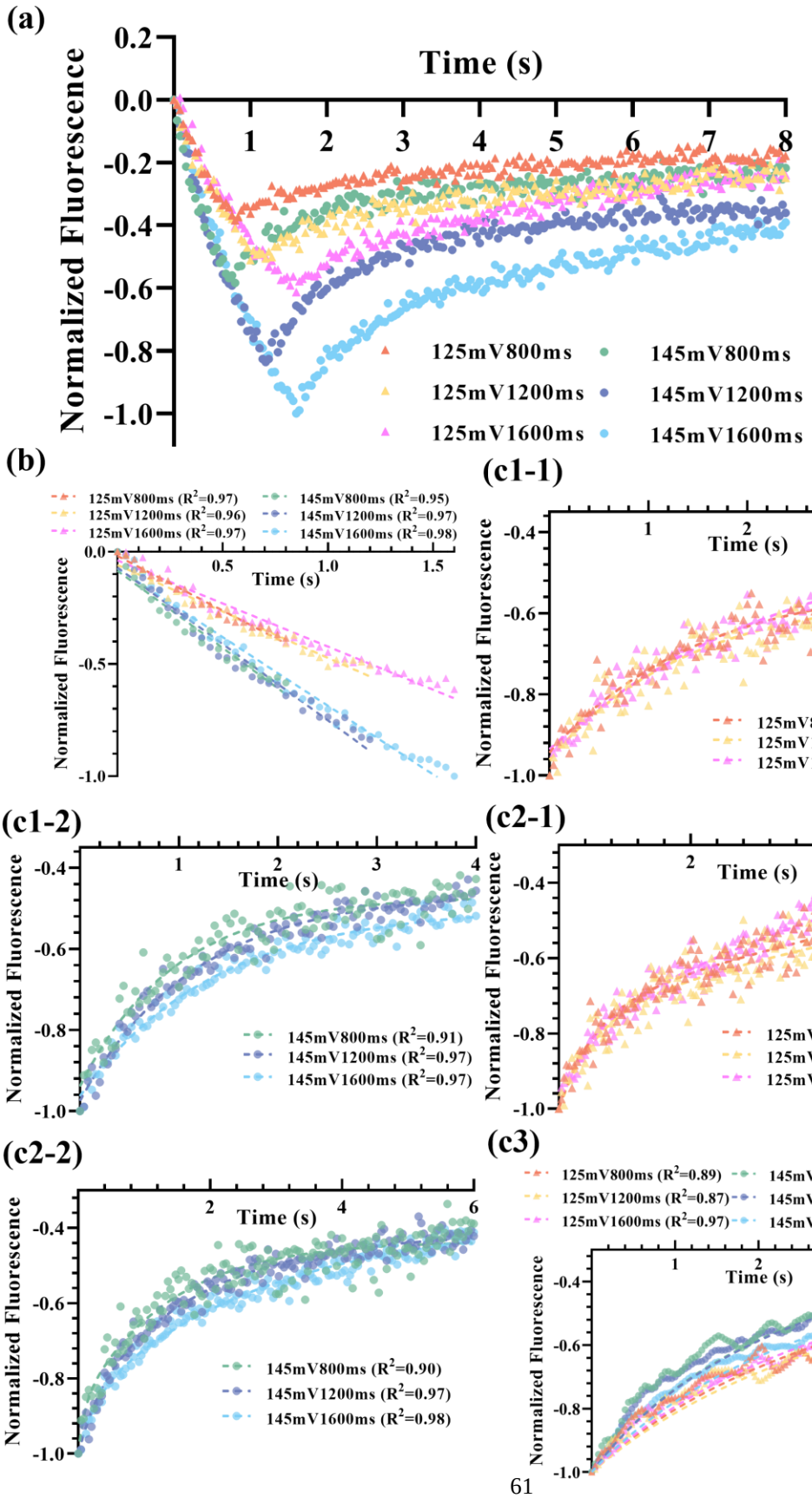
(a)
Normalized Fluorescence
Time (s)
125mV800ms
125mV1200ms
125mV1600ms
145mV800ms
145mV1200ms
145mV1600ms
(b)
125mV800ms (R²=0.97)
125mV1200ms (R²=0.96)
125mV1600ms (R²=0.97)
145mV800ms (R²=0.95)
145mV1200ms (R²=0.97)
145mV1600ms (R²=0.98)
(c1-1)
125mV800ms (R²=0.88)
125mV1200ms (R²=0.85)
125mV1600ms (R²=0.93)
(c1-2)
145mV800ms (R²=0.91)
145mV1200ms (R²=0.97)
145mV1600ms (R²=0.97)
(c2-1)
125mV800ms (R²=0.91)
125mV1200ms (R²=0.87)
125mV1600ms (R²=0.95)
(c2-2)
145mV800ms (R²=0.90)
145mV1200ms (R²=0.97)
145mV1600ms (R²=0.98)
(c3)
125mV800ms (R²=0.89)
125mV1200ms (R²=0.87)
125mV1600ms (R²=0.97)
145mV800ms (R²=0.83)
145mV1200ms (R²=0.92)
145mV1600ms (R²=0.92)

Figure 22 (a)The temporal fluorescence profiles in chicken breast tissues. (b) The fluorescence decreases during ultrasound exposure, and the results were fitted with a linear regression model. (c) The recovery of fluorescence and the results were processed with (c1-1; c1-2) single-phase exponential; (c2-1; c2-2) double exponential; (c3) custom M equations.

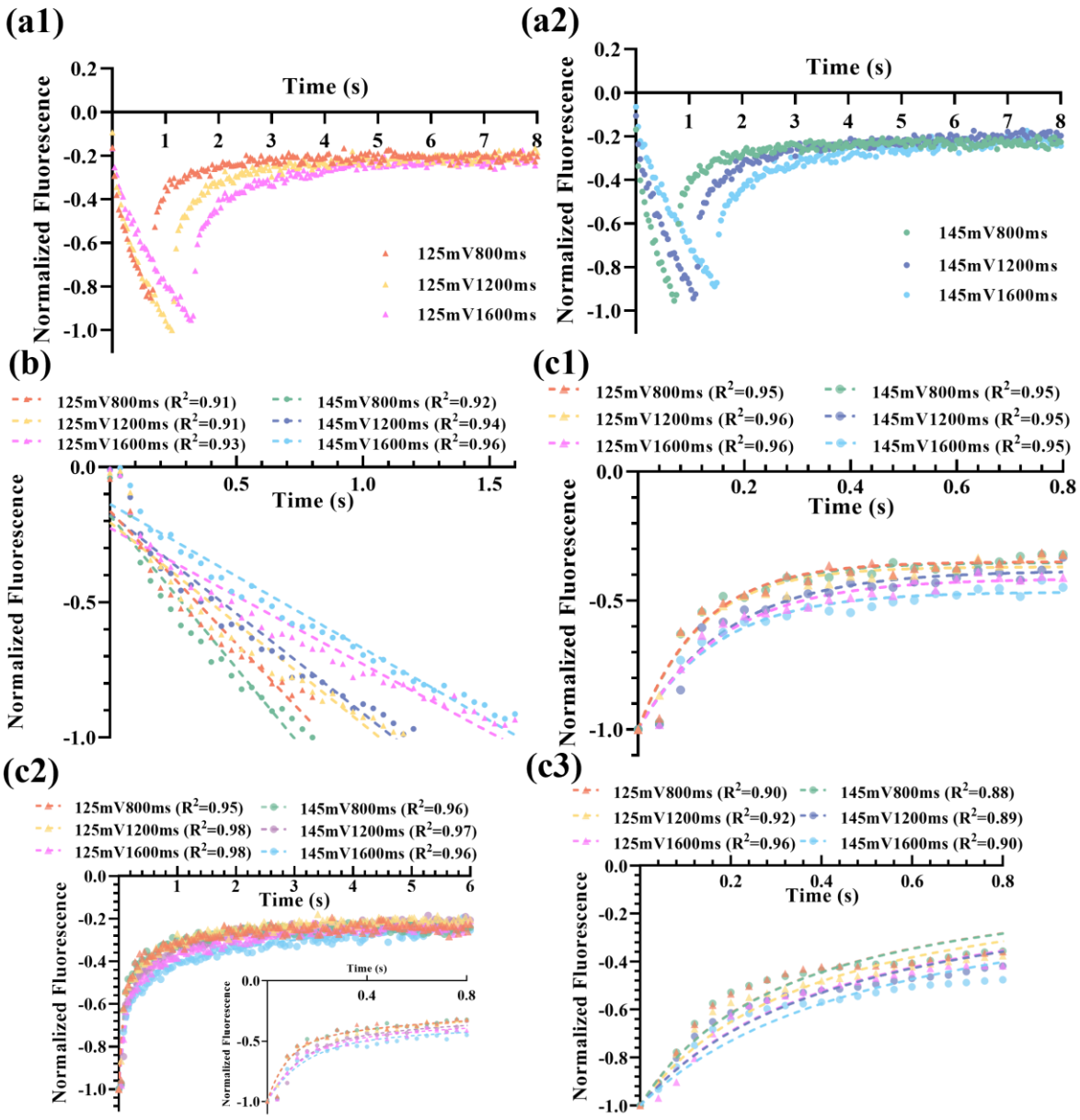

Figure 23 The dynamic fluorescence profiles in porcine tissues for the same voltage at (a1)125mV and (a1)145mV. (b) is the recovery of fluorescence after FU exposure, and the dashed curves represent the fitted linear results. (c) The recovery of fluorescence and their fitting results with (c1) single exponential; (c2) two-phase exponential; Inset: a zoom-in plot within a period from 0 to 0.8 s. (c3) custom *M* models (Dashed curves).

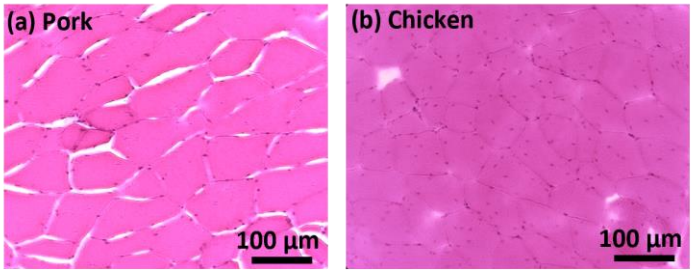

Figure 24 Image of H&E stained microstructure of tissues. (a) porcine loin muscle; (b) chicken breast.

Table 1 summarizes the fitting parameters obtained with different equations. The 125mV group has a lower absolute slope compared to the result for 145mV group (-0.43 ± 0.06 vs. -0.74 ± 0.24). During the ultrasound exposure, the displacements of nanoparticles were mainly dependent on the ultrasound strength. Therefore, a higher applied ultrasonic voltage means a more significant streaming effect in the tissues, leading to a faster fluorescence reduction rate. Fitting recovery data to a single exponential equation yields an average exponential time constant τ_r = 0.14 ± 0.02 in porcine tissues and τ_r =1.48 ± 0.50 in chicken tissues. The bi-exponential regression models give the fast (τ_{fast}) and slow (τ_{slow}) time constants and the relevant percent of fast decay component (Fast%). It is notable that these time constants in the bi-phase exponential fitting exhibit distinct values in both pork and chicken tissues (τ_{slow}=1.19 ± 0.52 vs. 7.94 ± 8.00; τ_{fast}= 0.11 ± 0.03 vs. 0.36 ± 0.18). In summary, the three-time constants (τ_r, τ_{slow}, and τ_{fast}) are tissue-dependent. The porcine muscle tissues showed smaller values than the chicken breast tissues, which indicates that the nanoagents (SR101-PLGA) in porcine tissues sample should be transported relatively easier and quicker. The shared percentage of fast exponential component (Fast%) in porcine is higher than that in chicken (63.26 vs. 21.11). Therefore, the porcine tissues exhibit notably shorter relaxation times, accompanied by a higher proportion of rapid change, which can be attributed to the faster fluid flow through larger pores interspersed among pork muscle fibers (see Fig. 24).

In both tissue samples, the value of τ_r seems to be not correlated with the exposure time. τ_{slow} in porcine tissues increases with the exposure time but it is not in chicken breast tissues (especially when the voltage is 125 mv). Additionally, there is not an obvious relationship between τ_{slow} and the voltage. No obvious relationship can be found between τ_{fast} and the two experimental parameters (i.e., voltage and exposure time). This is also true for the relationship between the parameter M and the two experimental parameters, which may be an indication that the transportability is mainly dependent on particles and tissues, not experimental parameters. Currently, it is unclear

how to understand the relationships between the time constants and the experimental parameters because the physical meanings of these time constants (τ_r, $\tau_{slow,}$ and τ_{fast}) are not as clear as the parameter M, so further studies should be conducted in future.

Tissue	FU Parameters		Reduction		Recovery							
			Linear		Single-phase		Two-phase				M-model	
	Voltage	Time	Slope	R^2	τ_r	R^2	τ_{slow}	τ_{fast}	Fast%	R^2	M	R^2
Chicken	125	800	-0.49	0.97	1.53	0.88	17.89	0.54	21.11	0.91	0.0054	0.89
	125	1200	-0.41	0.96	1.42	0.85	18.28	0.57		0.87	0.0051	0.87
	125	1600	-0.38	0.97	2.41	0.93	5.61	0.41		0.95	0.0058	0.97
	145	800	-0.69	0.95	0.97	0.91	1.34	0.09		0.9	0.0079	0.83
	145	1200	-0.68	0.97	1.17	0.97	1.77	0.29		0.97	0.0078	0.92
	145	1600	-0.61	0.98	1.36	0.97	2.77	0.25		0.98	0.0063	0.92
Porcine	125	800	-0.98	0.91	0.12	0.95	0.71	0.08	63.26	0.95	0.069	0.90
	125	1200	-0.75	0.91	0.12	0.96	0.98	0.08		0.98	0.059	0.92
	125	1600	-0.50	0.93	0.16	0.96	1.47	0.13		0.98	0.050	0.96
	145	800	-1.13	0.92	0.12	0.95	0.70	0.08		0.96	0.041	0.88
	145	1200	-0.77	0.94	0.17	0.95	1.23	0.13		0.97	0.049	0.89
	145	1600	-0.53	0.96	0.15	0.95	2.05	0.15		0.96	0.069	0.90

Table 1 The summary of best-fitting results in porcine and chicken tissues.

4.2.3 Limitations and future work

This study conducted a detailed experimental investigation into the interactions between FU and nanoparticles, elucidating the experimental findings through SIF-TUM. However, the tissue medium was simplistically characterized as a two-phase mixture comprising solid and liquid matrices. In reality, biological tissues possess a far more complex structure, with the presence of a vascular network, osmotic pressures, and various tissue heterogeneities, leading to the non-uniform distribution of nanoparticles [110], [111]. In this analysis, only dominant bioeffects and tissue properties were considered to maintain model simplicity and facilitate comprehension. Nevertheless, it is important to notice that future research endeavors may need to incorporate additional factors to explain the experimental results in a detailed way. Furthermore, the fitting process was restricted to only one or two parameters to facilitate the analysis and visualization of data trends. Extending the current fitting algorithm with multiple parameters may improve the accuracy.

4.4 Conclusion

In conclusion, this study experimentally demonstrated the feasibility of using ultrasound to induce nanoparticle motions via interstitial fluid streaming and tissue recovery within biological tissues. The dynamics of the fluorescence reduction and recovery induced by the SIF-TUM effect during and after ultrasound exposure were monitored and analyzed via three models: single-phase exponential regression, two-phase exponential regression, and an approximated analytical solution of the SIF-TUM model via a parameter of M. To avoid the thermal effect, a temperature-insensitive nanoparticle, SR101-PLGA, was synthesized and adopted in this study. In both chicken breast and porcine muscle tissues, the reduction and recovery of the fluorescence induced by ultrasound were noticed, which agrees with the prediction of the SIF-TUM models. The fluorescence reduction period and extent were significantly influenced by the ultrasound pressure and exposure time in chicken breast tissues, which agree with the results from the SIF-TUM models. In addition, all the time constants (τ_r, $\tau_{slow,}$ and τ_{fast}) depend on tissue type. Compared with chicken breast tissues, porcine muscle tissues seem more favorable for the nanoagents (SR101-PLGA) to transport. The parameter of M, which is defined as the transportability of the nanoagent in tissues via the SIF-TUM models, was found independent of ultrasound experimental parameters but was highly related to tissue types. Porcine muscle tissues adopted in this study showed much higher (~8.75 times) M values than those in chicken breast tissues. Therefore, it indicates that the transportability of the adopted nanoagent (SR101-PLGA) is much higher in porcine muscle tissues than in chicken breast tissues. The study underscores the potential significance of this research in advancing our understanding of ultrasound-involved nanoparticle delivery, which may enhance drug delivery efficiency for both therapeutic and diagnostic applications.

Chapter 5 *CONCLUSIONS AND FUTURE WORK*

5.1 Conclusions

This dissertation demonstrated the feasibility of *in vivo* tumor USF imaging using various NIR polymer-based USF contrast agents s detailed in Chapter 2. Notably, the development of differently sized ICG-PNIPAM USF agents yielded promising results in terms of biodistribution, highlighting their efficacy in passive tumor accumulation through the EPR effect. This breakthrough enabled the successful implementation of *in vivo* 3D tumor USF imaging via i.v. injections. Chapter 3 explored the estimation of local temperature via analyzing temporal profiles of USF signals during ultrasound-induced heating. This novel approach was validated by independent measurements from IR thermography, and its temperature measurement range can be adjusted by controlling the lipid compositions of the USF agents. Lastly, Chapter 4 presented an experimental investigation into the redistribution of nanoparticles in *ex vivo* tissues induced by ultrasound waves. The effects of different ultrasonic conditions in both chicken breast and porcine tissue samples were compared, which may help researchers understand the interactions between ultrasound and nanoparticles and achieve effective ultrasound-assisted drug delivery in tissues.

5.2 Limitations and future work

5.2.1 In vivo USF imaging in tumor

Although PNIPAM-based nanoparticles are very successful for *in vivo* USF imaging, the toxicity of PNIPAM is a concern in biological applications. Most PNIPAM-based nanoparticles are currently still in a developmental stage that is far from clinical application [112]. Thus, it is highly desirable to develop new nano-sized biocompatible USF contrast agents with a high on-to-off ratio, sharp switching performances, and reasonable stability. The liposome-based USF agent developed in our groups is a biocompatible option with a narrow switching band. However, its *in vivo* stability should be improved particularly for nanoscale formulations [31]. Furthermore, exploring nanoparticles with targeting components specific to tumor biomarkers may be another direction for achieving high delivery efficiency and minimal injection dose.

5.2.2 Further improvements in USF thermometry

The work described in this dissertation is only a feasibility study of USF thermometry in a phantom model, so further work will focus on the translations into *ex*/*in vivo* settings. The temperature calculation assumes that the

temperature in the focal volume increases linearly with time when the sample is exposed to FU. However, the HIFU-induced temperature growth can be affected by thermal diffusion, and thus the heating rate decreases with ultrasonic exposure time instead of being stable. Heating prediction models that consider thermal diffusion may be developed in the future to enhance the accuracy of temperature estimation. Furthermore, temperature-sensitive USF agents with high stability in biological environments are preferred, which can improve the repeatability and consistency of the temperature estimations.

5.2.3 Potential improvements on SIF-TUM

This work experimentally studied the interactions between FU and nanoparticles in *ex vivo* tissues based on SIF-TUM. However, the tissue medium usually exhibits heterogeneities that can influence nanoparticle transport. Hence, incorporating factors including vascular networks and muscle fiber orientations, into the model could offer valuable insights into variations in nanoparticle transport, enhancing the overall understanding of the system.

Reference

[1] R. Weissleder and M. Nahrendorf, “Advancing biomedical imaging,” *Proceedings of the National Academy of Sciences*, vol. 112, no. 47, pp. 14424–14428, Nov. 2015, doi: 10.1073/pnas.1508524112.

[2] F. Leblond, S. C. Davis, P. A. Valdés, and B. W. Pogue, “Pre-clinical whole-body fluorescence imaging: Review of instruments, methods and applications,” *Journal of Photochemistry and Photobiology B: Biology*, vol. 98, no. 1, pp. 77–94, Jan. 2010, doi: 10.1016/j.jphotobiol.2009.11.007.

[3] J. T. Alander *et al.*, “A review of indocyanine green fluorescent imaging in surgery,” *Journal of Biomedical Imaging*, vol. 2012, p. 7:7, Jan. 2012, doi: 10.1155/2012/940585.

[4] G. Hong, A. L. Antaris, and H. Dai, “Near-infrared fluorophores for biomedical imaging,” *Nat Biomed Eng*, vol. 1, no. 1, Art. no. 1, Jan. 2017, doi: 10.1038/s41551-016-0010.

[5] J. V. Frangioni, “In vivo near-infrared fluorescence imaging,” *Current Opinion in Chemical Biology*, vol. 7, no. 5, pp. 626–634, Oct. 2003, doi: 10.1016/j.cbpa.2003.08.007.

[6] C. Li, G. Chen, Y. Zhang, F. Wu, and Q. Wang, “Advanced Fluorescence Imaging Technology in the Near-Infrared-II Window for Biomedical Applications,” *J. Am. Chem. Soc.*, vol. 142, no. 35, pp. 14789–14804, Sep. 2020, doi: 10.1021/jacs.0c07022.

[7] J. Huang and K. Pu, “Near-infrared fluorescent molecular probes for imaging and diagnosis of nephro-urological diseases,” *Chemical Science*, vol. 12, no. 10, pp. 3379–3392, 2021, doi: 10.1039/D0SC02925D.

[8] B. Cheng *et al.*, “High-Resolution Ultrasound-Switchable Fluorescence Imaging in Centimeter-Deep Tissue Phantoms with High Signal-To-Noise Ratio and High Sensitivity via Novel Contrast Agents,” *PLoS ONE*, vol. 11, no. 11, p. e0165963, Nov. 2016, doi: 10.1371/journal.pone.0165963.

[9] T. Yao, S. Yu, Y. Liu, and B. Yuan, “Ultrasound-Switchable Fluorescence Imaging via an EMCCD Camera and a Z-Scan Method,” *IEEE J. Select. Topics Quantum Electron.*, vol. 25, no. 2, pp. 1–8, Mar. 2019, doi: 10.1109/JSTQE.2018.2883892.

[10] J. Kandukuri *et al.*, “A Dual-Modality System for Both Multi-Color Ultrasound-Switchable Fluorescence and Ultrasound Imaging,” *International Journal of Molecular Sciences*, vol. 18, no. 2, Art. no. 2, Feb. 2017, doi: 10.3390/ijms18020323.

[11] T. Namikawa, T. Sato, and K. Hanazaki, “Recent advances in near-infrared fluorescence-guided imaging surgery using indocyanine green,” *Surg Today*, vol. 45, no. 12, pp. 1467–1474, Dec. 2015, doi: 10.1007/s00595-015-1158-7.

[12] S. Ohnishi, S. J. Lomnes, R. G. Laurence, A. Gogbashian, G. Mariani, and J. V. Frangioni, “Organic Alternatives to Quantum Dots for Intraoperative Near-Infrared Fluorescent Sentinel Lymph Node Mapping,” *Mol Imaging*, vol. 4, no. 3, p. 15353500200505127, Jul. 2005, doi: 10.1162/15353500200505127.

[13] B. E. Schaafsma *et al.*, “The clinical use of indocyanine green as a near-infrared fluorescent contrast agent for image-guided oncologic surgery,” *Journal of Surgical Oncology*, vol. 104, no. 3, pp. 323–332, 2011, doi: 10.1002/jso.21943.

[14] Y. Yu, Y. Cheng, J. Tong, L. Zhang, Y. Wei, and M. Tian, “Recent advances in thermo-sensitive hydrogels for drug delivery,” *J. Mater. Chem. B*, vol. 9, no. 13, pp. 2979–2992, 2021, doi: 10.1039/D0TB02877K.

[15] “Near-Infrared Fluorescent Nanocapsules with Reversible Response to Thermal/pH Modulation for Optical Imaging.” Accessed: Oct. 06, 2023. [Online]. Available: https://pubs.acs.org/doi/epdf/10.1021/bm201350d

[16] H. Nsairat, D. Khater, U. Sayed, F. Odeh, A. Al Bawab, and W. Alshaer, “Liposomes: structure, composition, types, and clinical applications,” *Heliyon*, vol. 8, no. 5, p. e09394, May 2022, doi: 10.1016/j.heliyon.2022.e09394.

[17] D. Guimarães, A. Cavaco-Paulo, and E. Nogueira, “Design of liposomes as drug delivery system for therapeutic applications,” *International Journal of Pharmaceutics*, vol. 601, p. 120571, May 2021, doi: 10.1016/j.ijpharm.2021.120571.

[18] R.-L. Liu and R.-Q. Cai, “Recent advances in ultrasound-controlled fluorescence technology for deep tissue optical imaging,” *Journal of Pharmaceutical Analysis*, Oct. 2021, doi: 10.1016/j.jpha.2021.10.002.

[19] W. H. Abuwatfa, N. S. Awad, W. G. Pitt, and G. A. Husseini, “Thermosensitive Polymers and Thermo-Responsive Liposomal Drug Delivery Systems,” *Polymers*, vol. 14, no. 5, Art. no. 5, Jan. 2022, doi: 10.3390/polym14050925.

[20] T. Qin *et al.*, “Organic fluorescent thermometers: Highlights from 2013 to 2017,” *TrAC Trends in Analytical Chemistry*, vol. 102, pp. 259–271, May 2018, doi: 10.1016/j.trac.2018.03.003.

[21] G. Kucsko *et al.*, “Nanometre-scale thermometry in a living cell,” *Nature*, vol. 500, no. 7460, Art. no. 7460, Aug. 2013, doi: 10.1038/nature12373.

[22] F. Menges, P. Mensch, H. Schmid, H. Riel, A. Stemmer, and B. Gotsmann, “Temperature mapping of operating nanoscale devices by scanning probe thermometry,” *Nat Commun*, vol. 7, no. 1, Art. no. 1, Mar. 2016, doi: 10.1038/ncomms10874.

[23] M. Mecklenburg *et al.*, “Nanoscale temperature mapping in operating microelectronic devices,” *Science*, vol. 347, no. 6222, pp. 629–632, Feb. 2015, doi: 10.1126/science.aaa2433.

[24] K. Okabe, N. Inada, C. Gota, Y. Harada, T. Funatsu, and S. Uchiyama, “Intracellular temperature mapping with a fluorescent polymeric thermometer and fluorescence lifetime imaging microscopy,” *Nat Commun*, vol. 3, no. 1, p. 705, Jan. 2012, doi: 10.1038/ncomms1714.

[25] P. Löw, B. Kim, N. Takama, and C. Bergaud, “High-Spatial-Resolution Surface-Temperature Mapping Using Fluorescent Thermometry,” *Small*, vol. 4, no. 7, pp. 908–914, 2008, doi: 10.1002/smll.200700581.

[26] M. Mikolajek *et al.*, “Temperature Measurement Using Optical Fiber Methods: Overview and Evaluation,” *Journal of Sensors*, vol. 2020, p. e8831332, Oct. 2020, doi: 10.1155/2020/8831332.

[27] Q. Zhao, J. Zhang, R. Wang, and W. Cong, “Use of a Thermocouple for Malignant Tumor Detection,” *IEEE Eng. Med. Biol. Mag.*, vol. 27, no. 1, pp. 64–66, 2008, doi: 10.1109/MEMB.2007.913292.

[28] R. Usamentiaga, P. Venegas, J. Guerediaga, L. Vega, J. Molleda, and F. G. Bulnes, “Infrared Thermography for Temperature Measurement and Non-Destructive Testing,” *Sensors*, vol. 14, no. 7, Art. no. 7, Jul. 2014, doi: 10.3390/s140712305.

[29] D. D. Soerensen and L. J. Pedersen, “Infrared skin temperature measurements for monitoring health in pigs: a review,” *Acta Vet Scand*, vol. 57, no. 1, p. 5, Feb. 2015, doi: 10.1186/s13028-015-0094-2.

[30] Y. Liu *et al.*, “A Biocompatible and Near-Infrared Liposome for In Vivo Ultrasound-Switchable Fluorescence Imaging,” *Advanced Healthcare Materials*, vol. 9, no. 4, p. 1901457, 2020, doi: 10.1002/adhm.201901457.

[31] Y. Liu, T. Yao, L. Ren, and B. Yuan, “Size effect of liposomes on centimeter-deep ultrasound-switchable fluorescence imaging and ultrasound-controlled release,” *J. Mater. Chem. B*, vol. 10, no. 43, pp. 8970–8980, 2022, doi: 10.1039/D2TB01343F.

[32] D. G. Fisher and R. J. Price, “Recent Advances in the Use of Focused Ultrasound for Magnetic Resonance Image-Guided Therapeutic Nanoparticle Delivery to the Central Nervous System,” *Frontiers in*

Pharmacology, vol. 10, 2019, Accessed: Oct. 07, 2023. [Online]. Available: https://www.frontiersin.org/articles/10.3389/fphar.2019.01348

[33] L. Tu, Z. Liao, Z. Luo, Y.-L. Wu, A. Herrmann, and S. Huo, "Ultrasound-controlled drug release and drug activation for cancer therapy," *Exploration*, vol. 1, no. 3, p. 20210023, 2021, doi: 10.1002/EXP.20210023.

[34] R. Liu *et al.*, "Temperature-sensitive polymeric nanogels encapsulating with β-cyclodextrin and ICG complex for high-resolution deep-tissue ultrasound-switchable fluorescence imaging," *Nano Res.*, vol. 13, no. 4, pp. 1100–1110, Apr. 2020, doi: 10.1007/s12274-020-2752-6.

[35] B. Yuan, "Interstitial fluid streaming in deep tissue induced by ultrasound momentum transfer for accelerating nanoagent transport and controlling its distribution," *Phys. Med. Biol.*, vol. 67, no. 17, p. 175011, Sep. 2022, doi: 10.1088/1361-6560/ac88b5.

[36] T. Yao, S. Yu, Y. Liu, and B. Yuan, "In vivo ultrasound-switchable fluorescence imaging," *Sci Rep*, vol. 9, no. 1, Art. no. 1, Jul. 2019, doi: 10.1038/s41598-019-46298-2.

[37] S. Yu, T. Yao, Y. Liu, and B. Yuan, "In vivo ultrasound-switchable fluorescence imaging using a camera-based system," *Biomed. Opt. Express*, vol. 11, no. 3, p. 1517, Mar. 2020, doi: 10.1364/BOE.385996.

[38] C. A. Stine and J. M. Munson, "Convection-Enhanced Delivery: Connection to and Impact of Interstitial Fluid Flow," *Front. Oncol.*, vol. 9, p. 966, Oct. 2019, doi: 10.3389/fonc.2019.00966.

[39] F. Bray, M. Laversanne, E. Weiderpass, and I. Soerjomataram, "The ever-increasing importance of cancer as a leading cause of premature death worldwide," *Cancer*, vol. 127, no. 16, pp. 3029–3030, 2021, doi: 10.1002/cncr.33587.

[40] R. L. Siegel, K. D. Miller, N. S. Wagle, and A. Jemal, "Cancer statistics, 2023," *CA A Cancer J Clinicians*, vol. 73, no. 1, pp. 17–48, Jan. 2023, doi: 10.3322/caac.21763.

[41] T. Yao, Y. Liu, L. Ren, and B. Yuan, "Improving sensitivity and imaging depth of ultrasound-switchable fluorescence via an EMCCD-gain-controlled system and a liposome-based contrast agent," *Quant Imaging Med Surg*, vol. 11, no. 3, pp. 957–968, Mar. 2021, doi: 10.21037/qims-20-796.

[42] S. Yu *et al.*, "New generation ICG-based contrast agents for ultrasound-switchable fluorescence imaging," *Sci Rep*, vol. 6, no. 1, Art. no. 1, Oct. 2016, doi: 10.1038/srep35942.

[43] A. M. Gehling *et al.*, "Evaluation of Volume of Intramuscular Injection into the Caudal Thigh Muscles of Female and Male BALB/c Mice (Mus musculus)," *J Am Assoc Lab Anim Sci*, vol. 57, no. 1, pp. 35–43, Jan. 2018.

[44] M. Yu and J. Zheng, "Clearance Pathways and Tumor Targeting of Imaging Nanoparticles," *ACS Nano*, vol. 9, no. 7, pp. 6655–6674, Jul. 2015, doi: 10.1021/acsnano.5b01320.

[45] H. H. Gustafson, D. Holt-Casper, D. W. Grainger, and H. Ghandehari, "Nanoparticle uptake: The phagocyte problem," *Nano Today*, vol. 10, no. 4, pp. 487–510, Aug. 2015, doi: 10.1016/j.nantod.2015.06.006.

[46] C. de Wet and J. Moss, "METABOLIC FUNCTIONS OF THE LUNG," *Anesthesiology Clinics of North America*, vol. 16, no. 1, pp. 181–199, Mar. 1998, doi: 10.1016/S0889-8537(05)70013-4.

[47] A. C. Anselmo *et al.*, "Delivering Nanoparticles to Lungs while Avoiding Liver and Spleen through Adsorption on Red Blood Cells," *ACS Nano*, vol. 7, no. 12, pp. 11129–11137, Dec. 2013, doi: 10.1021/nn404853z.

[48] M. Izci, C. Maksoudian, B. B. Manshian, and S. J. Soenen, "The Use of Alternative Strategies for Enhanced Nanoparticle Delivery to Solid Tumors," *Chem. Rev.*, vol. 121, no. 3, pp. 1746–1803, Feb. 2021, doi: 10.1021/acs.chemrev.0c00779.

[49] M. Longmire, P. L. Choyke, and H. Kobayashi, “Clearance Properties of Nano-sized Particles and Molecules as Imaging Agents: Considerations and Caveats,” *Nanomedicine (Lond)*, vol. 3, no. 5, pp. 703–717, Oct. 2008, doi: 10.2217/17435889.3.5.703.

[50] E. A. Sykes *et al.*, “Tailoring nanoparticle designs to target cancer based on tumor pathophysiology,” *Proc. Natl. Acad. Sci. U.S.A.*, vol. 113, no. 9, Mar. 2016, doi: 10.1073/pnas.1521265113.

[51] J. Fang, W. Islam, and H. Maeda, “Exploiting the dynamics of the EPR effect and strategies to improve the therapeutic effects of nanomedicines by using EPR effect enhancers,” *Advanced Drug Delivery Reviews*, vol. 157, pp. 142–160, Jan. 2020, doi: 10.1016/j.addr.2020.06.005.

[52] R. B. Campbell *et al.*, “Cationic Charge Determines the Distribution of Liposomes between the Vascular and Extravascular Compartments of Tumors,” p. 7.

[53] H. Luo *et al.*, “ImmunoPET and Near-Infrared Fluorescence Imaging of Pancreatic Cancer with a Dual-Labeled Bispecific Antibody Fragment,” *Mol. Pharmaceutics*, vol. 14, no. 5, pp. 1646–1655, May 2017, doi: 10.1021/acs.molpharmaceut.6b01123.

[54] S. H. Hausner *et al.*, “Targeted *In vivo* Imaging of Integrin αvβ6 with an Improved Radiotracer and Its Relevance in a Pancreatic Tumor Model,” *Cancer Research*, vol. 69, no. 14, pp. 5843–5850, Jul. 2009, doi: 10.1158/0008-5472.CAN-08-4410.

[55] S. Ren *et al.*, “Emodin-Conjugated PEGylation of Fe3O4 Nanoparticles for FI/MRI Dual-Modal Imaging and Therapy in Pancreatic Cancer,” *Int J Nanomedicine*, vol. 16, pp. 7463–7478, Nov. 2021, doi: 10.2147/IJN.S335588.

[56] A. S. Wadajkar, B. Koppolu, M. Rahimi, and K. T. Nguyen, “Cytotoxic evaluation of N-isopropylacrylamide monomers and temperature-sensitive poly(N-isopropylacrylamide) nanoparticles,” *J Nanopart Res*, vol. 11, no. 6, pp. 1375–1382, Aug. 2009, doi: 10.1007/s11051-008-9526-5.

[57] H. Vihola, A. Laukkanen, L. Valtola, H. Tenhu, and J. Hirvonen, “Cytotoxicity of thermosensitive polymers poly(N-isopropylacrylamide), poly(N-vinylcaprolactam) and amphiphilically modified poly(N-vinylcaprolactam),” *Biomaterials*, vol. 26, no. 16, pp. 3055–3064, Jun. 2005, doi: 10.1016/j.biomaterials.2004.09.008.

[58] J. Shi, L. Yu, and J. Ding, “PEG-based thermosensitive and biodegradable hydrogels,” *Acta Biomaterialia*, vol. 128, pp. 42–59, Jul. 2021, doi: 10.1016/j.actbio.2021.04.009.

[59] M. Alawak *et al.*, “Magnetic resonance activatable thermosensitive liposomes for controlled doxorubicin delivery,” *Materials Science and Engineering: C*, vol. 115, p. 111116, Oct. 2020, doi: 10.1016/j.msec.2020.111116.

[60] J. P. Knapp, J. E. Kakish, B. W. Bridle, and D. J. Speicher, “Tumor Temperature: Friend or Foe of Virus-Based Cancer Immunotherapy,” *Biomedicines*, vol. 10, no. 8, p. 2024, Aug. 2022, doi: 10.3390/biomedicines10082024.

[61] J. D. Wallace and G. D. Dodd, “Thermography in the Diagnosis of Breast Cancer,” *Radiology*, vol. 91, no. 4, pp. 679–685, Oct. 1968, doi: 10.1148/91.4.679.

[62] C. Stefanadis *et al.*, “Increased Temperature of Malignant Urinary Bladder Tumors In Vivo: The Application of a New Method Based on a Catheter Technique,” *JCO*, vol. 19, no. 3, pp. 676–681, Feb. 2001, doi: 10.1200/JCO.2001.19.3.676.

[63] C. Stefanadis *et al.*, “Temperature differences are associated with malignancy on lung lesions: a clinical study,” *BMC Cancer*, vol. 3, no. 1, p. 1, Jan. 2003, doi: 10.1186/1471-2407-3-1.

[64] M. Gautherie, “Thermopathology of breast cancer: measurement and analysis of in vivo temperature and blood flow,” *Ann NY Acad Sci*, vol. 335, no. 1 Thermal Chara, pp. 383–415, Mar. 1980, doi: 10.1111/j.1749-6632.1980.tb50764.x.

[65] M. Gautherie, “Thermobiological assessment of benign and malignant breast diseases,” *American Journal of Obstetrics and Gynecology*, vol. 147, no. 8, pp. 861–869, Dec. 1983, doi: 10.1016/0002-9378(83)90236-3.

[66] S. A. Feig *et al.*, “Thermography, Mammography, and Clinical Examination in Breast Cancer Screening: Review of 16,000 Studies,” *Radiology*, vol. 122, no. 1, pp. 123–127, Jan. 1977, doi: 10.1148/122.1.123.

[67] R. N. Lawson and M. S. Chughtai, “Breast Cancer and Body Temperature,” *Can Med Assoc J*, vol. 88, no. 2, pp. 68–70, Jan. 1963.

[68] M. Moskowitz, J. Milbrath, P. Gartside, A. Zermeno, and D. Mandel, “Lack of Efficacy of Thermography as a Screening Tool for Minimal and Stage I Breast Cancer,” *N Engl J Med*, vol. 295, no. 5, pp. 249–252, Jul. 1976, doi: 10.1056/NEJM197607292950504.

[69] G. C. Wishart *et al.*, “The accuracy of digital infrared imaging for breast cancer detection in women undergoing breast biopsy,” *European Journal of Surgical Oncology (EJSO)*, vol. 36, no. 6, pp. 535–540, Jun. 2010, doi: 10.1016/j.ejso.2010.04.003.

[70] N. Arora *et al.*, “Effectiveness of a noninvasive digital infrared thermal imaging system in the detection of breast cancer,” *The American Journal of Surgery*, vol. 196, no. 4, pp. 523–526, Oct. 2008, doi: 10.1016/j.amjsurg.2008.06.015.

[71] N. F. Boyd, L. J. Martin, M. Bronskill, M. J. Yaffe, N. Duric, and S. Minkin, “Breast Tissue Composition and Susceptibility to Breast Cancer,” *JNCI: Journal of the National Cancer Institute*, vol. 102, no. 16, pp. 1224–1237, Aug. 2010, doi: 10.1093/jnci/djq239.

[72] P. C. Gøtzsche and K. J. Jørgensen, “Screening for breast cancer with mammography,” *Cochrane Database Syst Rev*, vol. 2013, no. 6, p. CD001877, Jun. 2013, doi: 10.1002/14651858.CD001877.pub5.

[73] S. H. Heywang-Köbrunner, A. Hacker, and S. Sedlacek, “Advantages and Disadvantages of Mammography Screening,” *Breast Care*, vol. 6, no. 3, pp. 2–2, 2011, doi: 10.1159/000329005.

[74] V. Rieke and K. Butts Pauly, “MR thermometry,” *Journal of Magnetic Resonance Imaging*, vol. 27, no. 2, pp. 376–390, 2008, doi: 10.1002/jmri.21265.

[75] J. Yuan, C.-S. Mei, L. P. Panych, N. J. McDannold, and B. Madore, “Towards fast and accurate temperature mapping with proton resonance frequency-based MR thermometry,” *Quantitative imaging in medicine and surgery*, vol. 2, no. 1, p. 21, 2012, doi: 10.3978/j.issn.2223-4292.2012.01.06.

[76] L. H. Lindner, H. M. Reinl, M. Schlemmer, R. Stahl, and M. Peller, “Paramagnetic thermosensitive liposomes for MR-thermometry,” *International Journal of Hyperthermia*, vol. 21, no. 6, pp. 575–588, Sep. 2005, doi: 10.1080/02656730500158410.

[77] M. A. Lewis, R. M. Staruch, and R. Chopra, “Thermometry and ablation monitoring with ultrasound,” *International Journal of Hyperthermia*, vol. 31, no. 2, pp. 163–181, Feb. 2015, doi: 10.3109/02656736.2015.1009180.

[78] J. Yao, H. Ke, S. Tai, Y. Zhou, and L. V. Wang, “Absolute photoacoustic thermometry in deep tissue,” *Opt. Lett., OL*, vol. 38, no. 24, pp. 5228–5231, Dec. 2013, doi: 10.1364/OL.38.005228.

[79] I. V. Larina, K. V. Larin, and R. O. Esenaliev, “Real-time optoacoustic monitoring of temperature in tissues,” *J. Phys. D: Appl. Phys.*, vol. 38, no. 15, pp. 2633–2639, Aug. 2005, doi: 10.1088/0022-3727/38/15/015.

[80] A. Hariri, J. Lemaster, J. Wang, A. S. Jeevarathinam, D. L. Chao, and J. V. Jokerst, "The characterization of an economic and portable LED-based photoacoustic imaging system to facilitate molecular imaging," *Photoacoustics*, vol. 9, pp. 10–20, Mar. 2018, doi: 10.1016/j.pacs.2017.11.001.

[81] M. W. Schellenberg and H. K. Hunt, "Hand-held optoacoustic imaging: A review," *Photoacoustics*, vol. 11, pp. 14–27, Sep. 2018, doi: 10.1016/j.pacs.2018.07.001.

[82] Y. Zhou, E. Tang, J. Luo, and J. Yao, "Deep-tissue temperature mapping by multi-illumination photoacoustic tomography aided by a diffusion optical model: a numerical study," *J. Biomed. Opt.*, vol. 23, no. 01, p. 1, Jan. 2018, doi: 10.1117/1.JBO.23.1.016014.

[83] Y. Zhou *et al.*, "Thermal memory based photoacoustic imaging of temperature," *Optica*, vol. 6, no. 2, p. 198, Feb. 2019, doi: 10.1364/OPTICA.6.000198.

[84] L. Ren, Y. Liu, T. Yao, K. T. Nguyen, and B. Yuan, "In vivo tumor ultrasound-switchable fluorescence imaging via intravenous injections of size-controlled thermosensitive nanoparticles," *Nano Res.*, Sep. 2022, doi: 10.1007/s12274-022-4846-9.

[85] Y. Pei *et al.*, "High resolution imaging beyond the acoustic diffraction limit in deep tissue via ultrasound-switchable NIR fluorescence," *Sci Rep*, vol. 4, no. 1, p. 4690, Apr. 2014, doi: 10.1038/srep04690.

[86] B. Yuan, S. Uchiyama, Y. Liu, K. T. Nguyen, and G. Alexandrakis, "High-resolution imaging in a deep turbid medium based on an ultrasound-switchable fluorescence technique," *Appl. Phys. Lett.*, vol. 101, no. 3, p. 033703, Jul. 2012, doi: 10.1063/1.4737211.

[87] M. Pons, M. Foradada, and J. Estelrich, "Liposomes obtained by the ethanol injection method," *International Journal of Pharmaceutics*, vol. 95, no. 1–3, pp. 51–56, Jun. 1993, doi: 10.1016/0378-5173(93)90389-W.

[88] T. Lu and T. L. M. ten Hagen, "Inhomogeneous crystal grain formation in DPPC-DSPC based thermosensitive liposomes determines content release kinetics," *Journal of Controlled Release*, vol. 247, pp. 64–72, Feb. 2017, doi: 10.1016/j.jconrel.2016.12.030.

[89] B. Yuan, Y. Pei, and J. Kandukuri, "Breaking the acoustic diffraction limit via nonlinear effect and thermal confinement for potential deep-tissue high-resolution imaging," *Appl. Phys. Lett.*, vol. 102, no. 6, p. 063703, Feb. 2013, doi: 10.1063/1.4792736.

[90] M. Anderson and A. Omri, "The Effect of Different Lipid Components on the In Vitro Stability and Release Kinetics of Liposome Formulations," *Drug Delivery*, vol. 11, no. 1, pp. 33–39, Jan. 2004, doi: 10.1080/10717540490265243.

[91] T. D. Khokhlova and J. H. Hwang, "HIFU for palliative treatment of pancreatic cancer," *J Gastrointest Oncol*, vol. 2, no. 3, pp. 175–184, Sep. 2011, doi: 10.3978/j.issn.2078-6891.2011.033.

[92] S. B. Barnett, G. R. Ter Haar, M. C. Ziskin, H.-D. Rott, F. A. Duck, and K. Maeda, "International recommendations and guidelines for the safe use of diagnostic ultrasound in medicine," *Ultrasound in Medicine & Biology*, vol. 26, no. 3, pp. 355–366, Mar. 2000, doi: 10.1016/S0301-5629(00)00204-0.

[93] M.-L. Briuglia, C. Rotella, A. McFarlane, and D. A. Lamprou, "Influence of cholesterol on liposome stability and on in vitro drug release," *Drug Deliv. and Transl. Res.*, vol. 5, no. 3, pp. 231–242, Jun. 2015, doi: 10.1007/s13346-015-0220-8.

[94] Y. Yao *et al.*, "Nanoparticle-Based Drug Delivery in Cancer Therapy and Its Role in Overcoming Drug Resistance," *Frontiers in Molecular Biosciences*, vol. 7, 2020, Accessed: Sep. 24, 2023. [Online]. Available: https://www.frontiersin.org/articles/10.3389/fmolb.2020.00193

[95] S. Wilhelm *et al.*, "Analysis of nanoparticle delivery to tumours," *Nat Rev Mater*, vol. 1, no. 5, Art. no. 5, Apr. 2016, doi: 10.1038/natrevmats.2016.14.

[96] P. Tharkar, R. Varanasi, W. S. F. Wong, C. T. Jin, and W. Chrzanowski, “Nano-Enhanced Drug Delivery and Therapeutic Ultrasound for Cancer Treatment and Beyond,” *Frontiers in Bioengineering and Biotechnology*, vol. 7, 2019, Accessed: Sep. 22, 2023. [Online]. Available: https://www.frontiersin.org/articles/10.3389/fbioe.2019.00324

[97] S. Ohta, E. Kikuchi, A. Ishijima, T. Azuma, I. Sakuma, and T. Ito, “Investigating the optimum size of nanoparticles for their delivery into the brain assisted by focused ultrasound-induced blood–brain barrier opening,” *Sci Rep*, vol. 10, no. 1, Art. no. 1, Oct. 2020, doi: 10.1038/s41598-020-75253-9.

[98] V. Sheth, L. Wang, R. Bhattacharya, P. Mukherjee, and S. Wilhelm, “Strategies for Delivering Nanoparticles across Tumor Blood Vessels,” *Advanced Functional Materials*, vol. 31, no. 8, p. 2007363, 2021, doi: 10.1002/adfm.202007363.

[99] A. Jain, A. Tiwari, A. Verma, and S. K. Jain, “Ultrasound-based triggered drug delivery to tumors,” *Drug Deliv. and Transl. Res.*, vol. 8, no. 1, pp. 150–164, Feb. 2018, doi: 10.1007/s13346-017-0448-6.

[100] S. Mullick Chowdhury, T. Lee, and J. K. Willmann, “Ultrasound-guided drug delivery in cancer,” *Ultrasonography*, vol. 36, no. 3, pp. 171–184, Jul. 2017, doi: 10.14366/usg.17021.

[101] K. Entzian and A. Aigner, “Drug Delivery by Ultrasound-Responsive Nanocarriers for Cancer Treatment,” *Pharmaceutics*, vol. 13, no. 8, p. 1135, Jul. 2021, doi: 10.3390/pharmaceutics13081135.

[102] S. M. Chowdhury, L. Abou-Elkacem, T. Lee, J. Dahl, and A. M. Lutz, “Ultrasound and microbubble mediated therapeutic delivery: Underlying mechanisms and future outlook,” *Journal of Controlled Release*, vol. 326, pp. 75–90, Oct. 2020, doi: 10.1016/j.jconrel.2020.06.008.

[103] L. Ren, T. Yao, K. T. Nguyen, and B. Yuan, “Noninvasive measurement of local temperature using ultrasound-switchable fluorescence,” *Biomed. Opt. Express*, vol. 14, no. 9, p. 4406, Sep. 2023, doi: 10.1364/BOE.497815.

[104] J. U. Menon, P. Ravikumar, A. Pise, D. Gyawali, C. C. W. Hsia, and K. T. Nguyen, “Polymeric nanoparticles for pulmonary protein and DNA delivery,” *Acta Biomaterialia*, vol. 10, no. 6, pp. 2643–2652, Jun. 2014, doi: 10.1016/j.actbio.2014.01.033.

[105] S. Rezvantalab *et al.*, “PLGA-Based Nanoparticles in Cancer Treatment,” *Frontiers in Pharmacology*, vol. 9, 2018, Accessed: Sep. 18, 2023. [Online]. Available: https://www.frontiersin.org/articles/10.3389/fphar.2018.01260

[106] S. Kona, J.-F. Dong, Y. Liu, J. Tan, and K. T. Nguyen, “Biodegradable nanoparticles mimicking platelet binding as a targeted and controlled drug delivery system,” *International Journal of Pharmaceutics*, vol. 423, no. 2, pp. 516–524, Feb. 2012, doi: 10.1016/j.ijpharm.2011.11.043.

[107] A. Anand and P. J. Kaczkowski, “Noninvasive measurement of local thermal diffusivity using backscattered ultrasound and focused ultrasound heating,” *Ultrasound Med Biol*, vol. 34, no. 9, pp. 1449–1464, Sep. 2008, doi: 10.1016/j.ultrasmedbio.2008.02.004.

[108] R. Vyas and M. L. Rustgi, “Green’s function solution to the tissue bioheat equation,” *Medical Physics*, vol. 19, no. 5, pp. 1319–1324, 1992, doi: 10.1118/1.596767.

[109] M. Mohammadkhah, P. Murphy, and C. K. Simms, “The in vitro passive elastic response of chicken pectoralis muscle to applied tensile and compressive deformation,” *Journal of the Mechanical Behavior of Biomedical Materials*, vol. 62, pp. 468–480, Sep. 2016, doi: 10.1016/j.jmbbm.2016.05.021.

[110] M. Sefidgar *et al.*, “Numerical modeling of drug delivery in a dynamic solid tumor microvasculature,” *Microvascular Research*, vol. 99, pp. 43–56, May 2015, doi: 10.1016/j.mvr.2015.02.007.

[111] C. O'Connor, E. Brady, Y. Zheng, E. Moore, and K. R. Stevens, "Engineering the multiscale complexity of vascular networks," *Nat Rev Mater*, vol. 7, no. 9, pp. 702–716, May 2022, doi: 10.1038/s41578-022-00447-8.

[112] X. Xu *et al.*, "Poly(N-isopropylacrylamide)-Based Thermoresponsive Composite Hydrogels for Biomedical Applications," *Polymers*, vol. 12, no. 3, Art. no. 3, Mar. 2020, doi: 10.3390/polym12030580.

APPENDIX A – COMPARISON BETWEEN NEGATIVE AND POSITIVE USF IN TUMOR

Negative USF in BxPC-3 tumor

200 µL PNIPAM/β-CD/ICG nanogels were delivered intravenously (i.v.) to the BxPC-3 tumor-bearing nude mouse via tail vein injection. The synthesis method was described in the published work [34]. The concentration of nanogels was 90 mg/mL. USF imaging was carried out at 10 h post-administration in a camera-based USF system reported in this study [41].

Figure 25 shows the PNIPAM/β-CD/ICG nanogels accumulated in the tumor area with a high tumor-to-background contrast. The fluorescence of tumor increased with time and reached the strongest intensity at 8 h postinjection. As shown in Fig. 26, the USF images were captured at various locations within the tumor area. The electric peak-peak voltage and exposure time of HIFU pulses set in the function generator were 70 mV and 1200 ms respectively in the locations labeled as (i), (ii), (iii), and (iv), while the voltage was increased to 140 mV and the exposure time was reduced to 400 ms in the location (v). The fluorescence signals were reduced 0.92 %, 1.18 %, 0.46 %, 0.48 %, and 1.26 % at the locations from (i) to (v), compared with the average fluorescence intensity in the zoom-in images (5 x 5 mm^2) before the HIFU exposure.

Positive USF in BxPC-3 tumor

Positive USF signals were acquired in the same USF system following a similar protocol. However, PNIPAM-ICG nanogels were administrated i.v. instead of PNIPAM/β-CD/ICG nanogels, and the preparation method was based on a previous study [84]. The PNIPAM-ICG nanogels were concentrated at 79 mg/mL. At approximately 30 h postinjection, the BxPC-3 tumor-bearing mouse was ready for the USF imaging.

The biodistibution results of PNIPAM-ICG nanogels are shown in Fig. 27. At 24 h post-adminstration, the tumor site showed an increased fluorescence intensity as more nanogels were retained during the circulation. Figure 28 demonstrates the positive USF profiles in the BxPC-3 tumor. The electric peak-peak voltage applied to the HIFU transducer was kept at 125 mV, and the exposure time was 400 ms. The fluorescence signals increased 27.13 %, 71.07 %, 63.04 %, and 14.22 % at the locations from (i) to (iv), compared with the average fluorescence signal in the zoom-in areas before the HIFU pulses were applied.

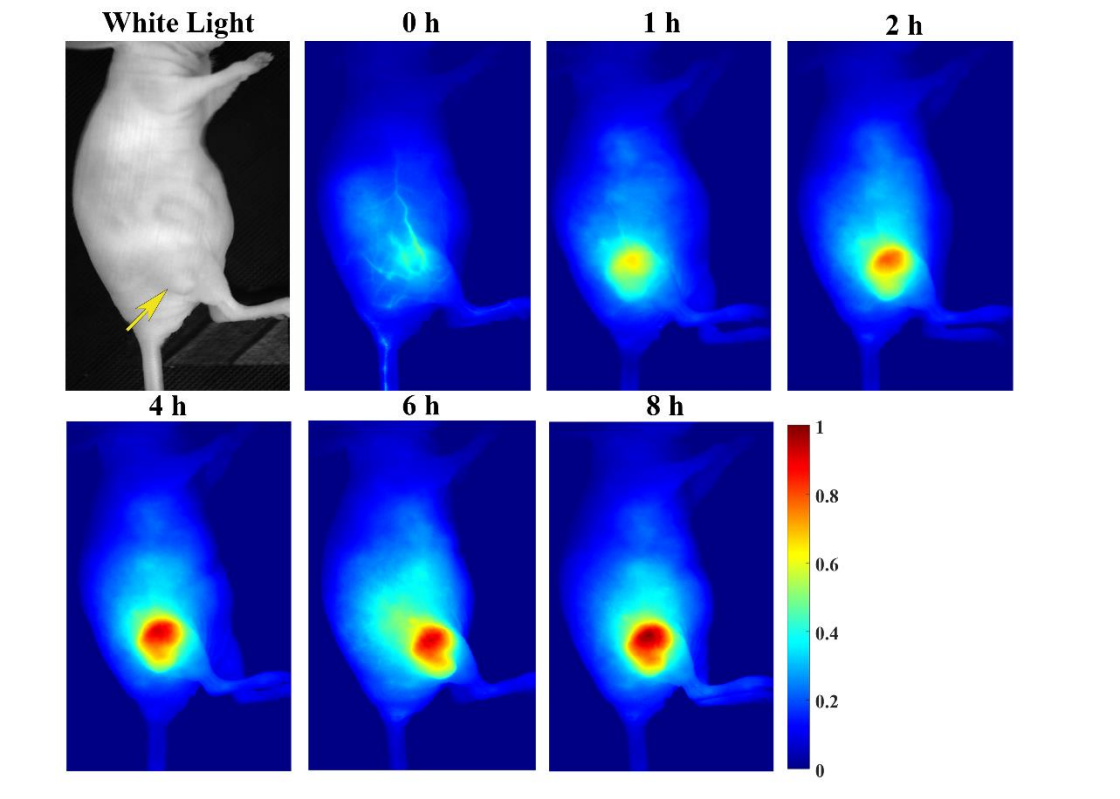

Figure 25 The accumulation of nanogels at selected time points after i.v. injection of PNIPAM/β-CD/ICG. The image captured immediately after i.v. injection was labeled as 0 h.

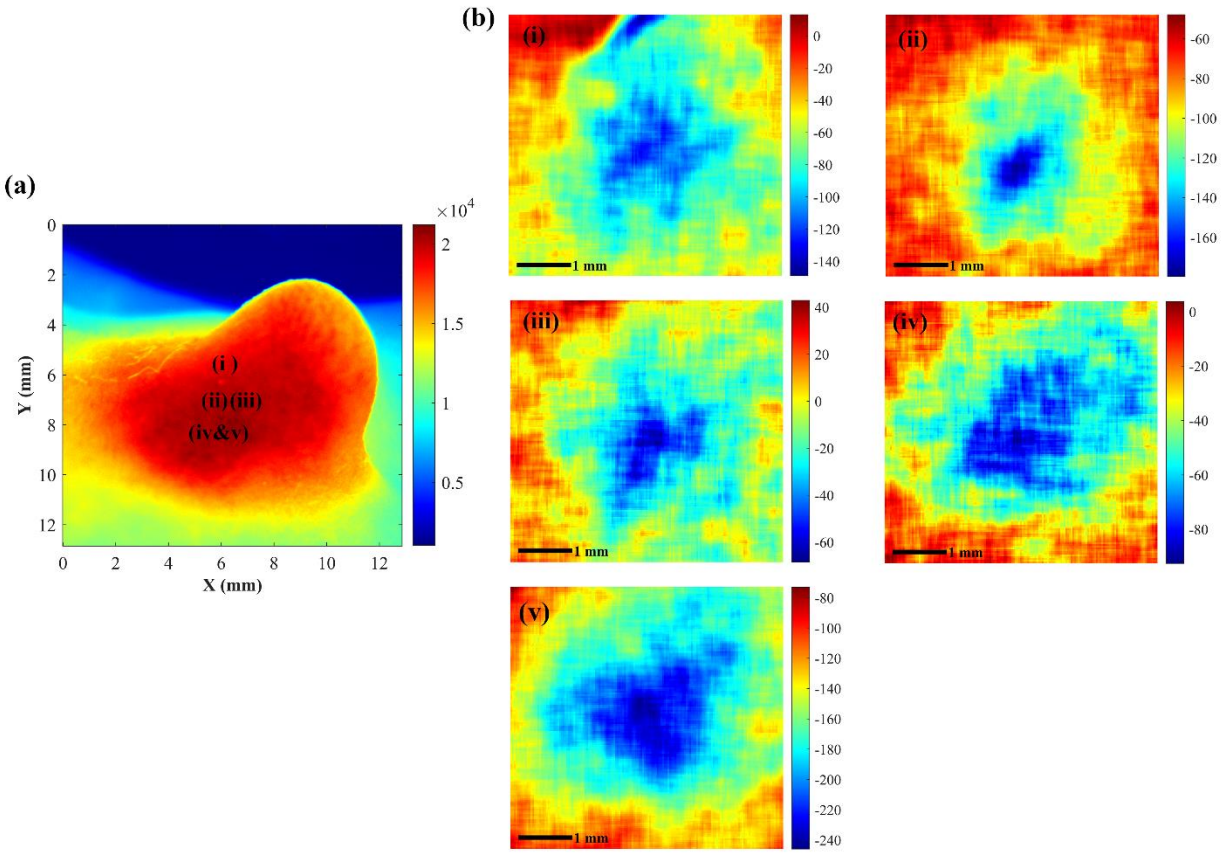

Figure 26 (a) is a zoom-in view (13 x 13 mm^2) of tumor area. (b) represents the zoom-in images (5 x 5 mm^2) of negative USF distribution profiles at four different locations as highlighted in (a) as (i), (ii), (iii), (iv), and (v). Scale bar = 1 mm.

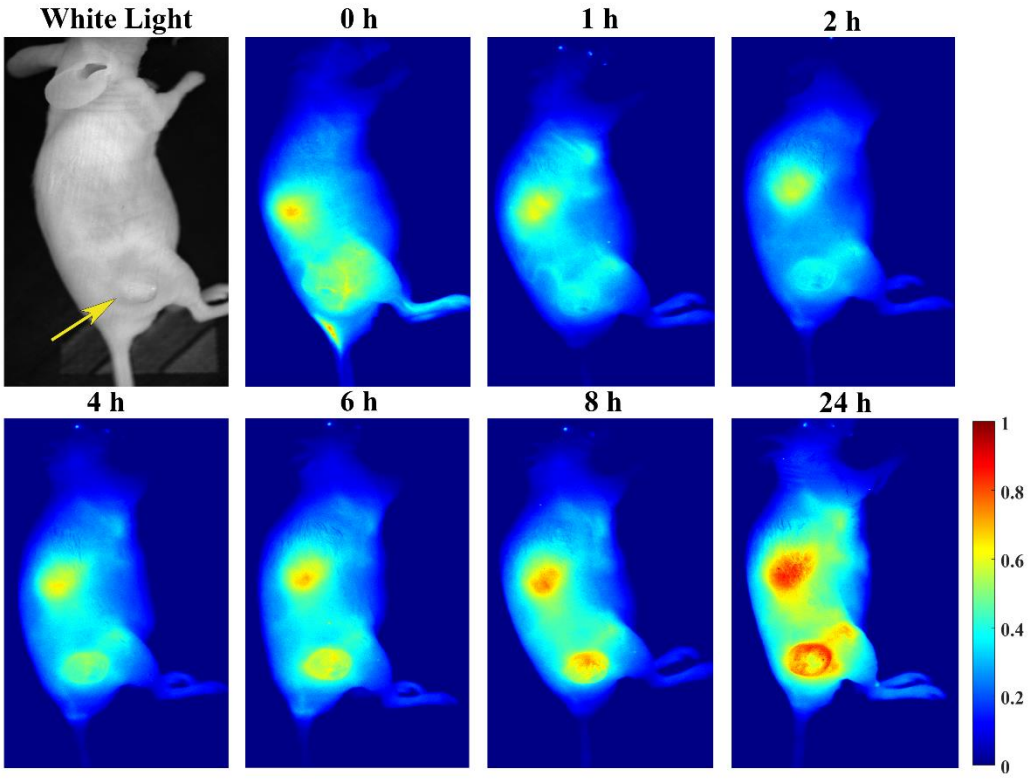

Figure 27 The images of BxPC-3 tumor-bearing mouse after i.v. injection of PNIPAM/ICG. 0 h image was taken immediately after i.v. administration.

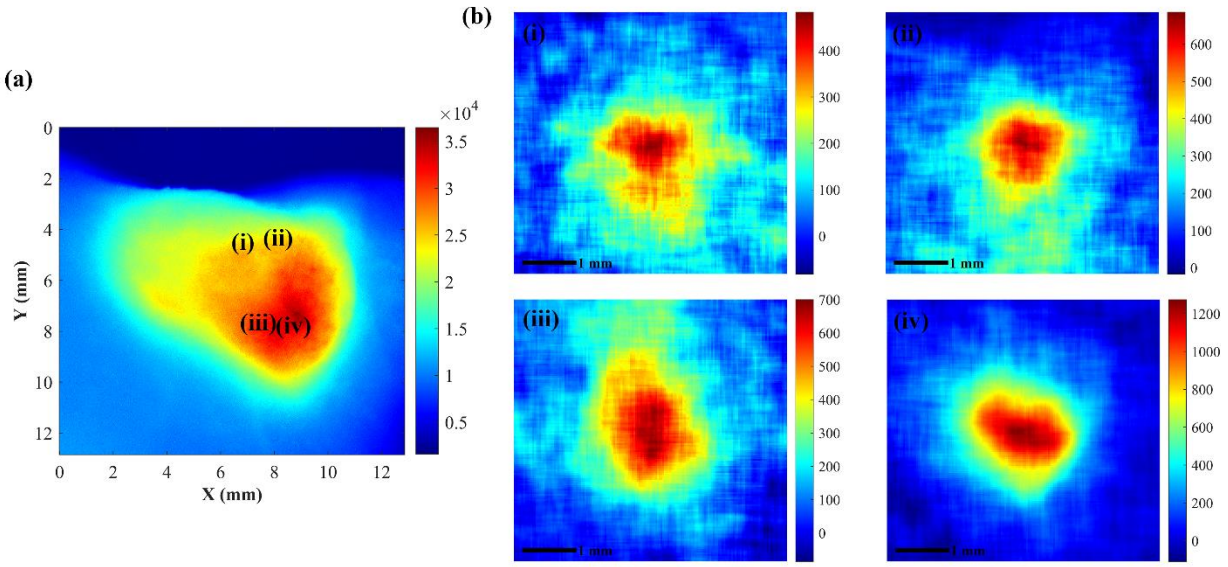

Figure 28 (a) Fluorescence image of tumor. (b) Zoom-in images of positive USF profiles at selected locations as indicated in (a). Scale bar = 1 mm.

Biographical Information

Liqin Ren received the M.S. degree in optics and photonics from Imperial College London, London, U.K. in 2016. Building on this foundation, she pursued a Doctor of Philosophy degree in Biomedical Engineering from the esteemed Joint Program of University of Texas at Arlington and the University of Texas Southwestern Medical Center, Texas, USA, in 2023.

During her academic pursuit, Liqin Ren engaged in impactful research and academic roles. As a research assistant in Prof. Baohong Yuan's Ultrasound and Optical Imaging laboratory, she focused on the ultrasound-switchable fluorescence imaging for various biomedical applications. Her journey as a researcher also saw her taking on teaching assistant responsibilities for various courses including bio-instrumentation, tissue-ultrasound optical imaging, human physiology, cell physiology, biomedical optics laboratory, and senior design projects.

Throughout her doctoral journey, Liqin contributed two first-author peer-viewed journal papers, three co-author journal papers, and filed one US patent. She received the Award for Outstanding Biomedical Engineering PhD Student twice in both 2022 and 2023. As she continues her journey, she aspires to make even more significant contributions to the field of biomedical engineering.